# Quasi-Orthogonal Wideband Radar Waveforms Based on Chaotic Systems

by

Matt Willsey

Submitted to the Department of Electrical Engineering and Computer Science
in partial fulfillment of the requirements for the degree of
Master of Engineering in Electrical Engineering and Computer Science
at the
MASSACHUSETTS INSTITUTE OF TECHNOLOGY
December 2006

This work was sponsored by the Air Force Research Laboratory under Air Force Contract No. FA8721-05-C-0002. Opinions, interpretations, recommendations and conclusions are that of the authors and are not necessarily endorsed by the United States Government.

Author . . . . . . . . . . . . . . . . . . . . . . . . . . . . . . . . . . . . . . . . . . . . . . . . . . . . . .
Department of Electrical Engineering and Computer Science
December 13, 2006

Certified by . . . . . . . . . . . . . . . . . . . . . . . . . . . . . . . . . . . . . . . . . . . . . . . . . . .
Alan V. Oppenheim
Ford Professor of Engineering
Thesis Supervisor

Certified by . . . . . . . . . . . . . . . . . . . . . . . . . . . . . . . . . . . . . . . . . . . . . . . . . . .
Kevin M. Cuomo
Senior Staff, MIT Lincoln Laboratory
Thesis Supervisor

Accepted by . . . . . . . . . . . . . . . . . . . . . . . . . . . . . . . . . . . . . . . . . . . . . . . . . . .
Arthur C. Smith
Chairman, Department Committee on Graduate Students

# Quasi-Orthogonal Wideband Radar Waveforms Based on Chaotic Systems

by

Matt Willsey

Submitted to the Department of Electrical Engineering and Computer Science
on December 13, 2006, in partial fulfillment of the
requirements for the degree of
Master of Engineering in Electrical Engineering and Computer Science

## Abstract

With the development of A/D converters possessing sufficiently high sampling rates, it is now feasible to use arbitrary, wideband waveforms in radar applications. Large sets of quasi-orthogonal, wideband waveforms can be generated so that multiple radars can simultaneously operate in the same frequency band. Each individual radar receiver can process its own return as well as the orthogonal returns from the other radars, which opens the possibility for developing algorithms that combine data from multiple radar channels. Due to the random nature of chaotic signals, it is possible to develop a procedure for generating large sets ($> 50$) of quasi-orthogonal radar waveforms using deterministic chaos.

Deterministic chaos is defined as a bounded, aperiodic flow with a sensitive dependence on initial conditions. There are many different types of chaotic systems. In this thesis, waveforms will be generated from the well-studied Lorenz system. Each waveform from the Lorenz system can be fully characterized by three parameters ($\sigma$, b, and r) and a set of initial conditions, ($x_o$, $y_o$, $z_o$). The particular parameter values greatly affect quality of the Lorenz waveform as quasi-orthogonal radar waveform. Therefore, this thesis conducts a parameter study to quantify how the parameters affect various radar waveform metrics. Additionally, this thesis proposes a procedure for modifying the Lorenz waveform in order to improve its performance on these metrics.

Thesis Supervisor: Alan V. Oppenheim
Title: Ford Professor of Engineering

Thesis Supervisor: Kevin M. Cuomo
Title: Senior Staff, MIT Lincoln Laboratory

# Acknowledgments

A great technical benefit in completing a thesis is collaborating with a research advisor to gain both a better understanding in a particular field and to learn general problem solving skills. I have been very fortunate to have had the opportunity to collaborate closely with two advisors: Dr. Kevin Cuomo and Professor Alan Oppenheim. In addition to collaborating with this thesis, both of my advisors are outstanding individuals.

I have been involved in the MIT VI-A program for the last few years, which is a program that enables me to collaborate with MIT Lincoln Laboratory on a laboratory thesis project. My advisor at Lincoln Laboratory is Dr. Kevin Cuomo, and we have worked very closely throughout the duration of this thesis. Despite that Kevin is very intelligent and qualified, anyone who has spent time with him will tell you that he is also uncharacteristically modest and completely down to earth. Moreover, even with his busy schedule, Kevin could always make himself available when I needed help. His encouragement, motivation, advice, and support were essential to the completion of this thesis. However, not only has Kevin been a great advisor, but he is also a great friend. I value all the time that I have had to get to know him better during all of our meetings and lunches at Lincoln, where our conversations were not limited to just technical topics.

Over the past year, I have had the opportunity to also work with Professor Alan Oppenheim, who insists on me calling him Al. Many people are familiar with Al's many technical accomplishments and his reputation for being a fantastic thesis advisor. Without question, the quality of this thesis was very heavily influenced by Al's guidance and help. However, I will never forget when Al saw me standing in the office with my bags packed ready to catch the subway to the airport. Without hesitating, he offered to drop me off at the airport. Al often explains that an advisor/advisee relationship is much like a father/son relationship. I feel like Al is concerned with my development both as an engineer and a person. I am very grateful for the impact that he has made on my life.

I would also like to thank Dr. Frank Robey for funding most of this thesis research. Frank has been very helpful during my stay at Lincoln Laboratory. He is very understanding and has made sacrifices to make my research at Lincoln easier. For example, Frank helped me acquire a laptop computer to allow me to more easily transport my work between Cambridge and Lexington. Moreover, Frank has always encouraged and promoted my research for which I am very appreciative.

This thesis was also funded, in part, by the Siebel Systems, Inc. I was provided with a full semester of funding as a recipient of the Siebel scholarship. I am grateful for this scholarship and consider this award a great honor.

Many others have contributed to the technical development of this thesis. Engaging technical discussions with Ross Bland, Sourav Dey, Al Kharbouch, and Charles Rhohrs significantly affected this thesis. They are, of course, great friends and are also co-workers in the Digital Signal Processing Group at MIT. At Lincoln Laboratory, both Jeff McHarg and Scott Coutts always made themselves available whenever I had any questions or concerns about this research. I would also like thank Scott for some editorial comments. It has been my privilege to work with both Jeff and Scott and to get to know them better. Additionally, Jeff had been my advisor at Lincoln Laboratory while I was an undergraduate at MIT and has greatly contributed to my development, and I am especially thankful. Also, I would like to thank Tom Gross for helping me through tests on the Next Generation Radar.

I have worked closely with both Group 33 at Lincoln Laboratory and the Digital Signal Processing Group (DSPG) at MIT. Specifically, in Group 33, I have had the privilege of working closely with Scott Coutts, Kevin Cuomo, Jeff McHarg, Frank Robey, and Dennis Weikle. In DSPG, I have had the privilege of working with Arthur Baggeroer, Ross Bland, Tom Baran, Petros Boufounos, Sourav Dey, Zahi Karam, Alaa Kharbouch, Al Oppenheim, Charles Rohrs, Melanie Rudoy, Joesph Sikora, Eric Strattman, Archana Venkataraman, and Dennis Wei.

I have also had the opportunity to make several presentations to DSPG in the weekly group meetings (which were actually referred to as ”brainstorming sessions where $1 + 1 = 3$”). In these meetings, I had the opportunity to present my research

in a casual setting to the other members of the group and a few visiting scientists including Dan Dudgeon and Steve Smith. Moreover, these meetings provoked many comments which became incorporated into my thesis. Without question, this thesis was significantly influenced by these group meetings.

I would like to also thank all those who both directly and indirectly supported me and this thesis. It is impossible to list everybody, and I apologize for anyone that I have missed.

On a personal level, I would like to thank my loving family for all of their sacrifice and support. I would like to thank my parents for their guidance and dedication to raising me as best they could. Describing, in words, all that they have done for me is simply impossible. From feeding the ducks with my dad in second grade to after-school chats with my mom to all the high school basketball games that my parents never missed, I feel extremely blessed to have such fantastic parents. I would also like to thank my brother, Mark, and my sister, Kelli. I could have never ask for any better siblings. I would also like to thank both sets of grandparents for supporting me both emotionally and financially. Their support greatly encouraged me. I would also like to thank all those in my extended family.

I would also like to thank my friends for making my stay in Boston enjoyable. I have made many friends while in Boston, and without mentioning any names, I would like thank them all. However, I would like to give a special thanks to Ross Bland who was my roommate, my office-mate, class-mate, and close friend. I was around Ross every day for almost my entire stay in Boston. We have many good memories. We rode our bikes in sub-zero weather all around Boston. When I bought a pickup, we drove all over New England. We spent many late nights studying and had many late-night discussions on completely random topics such as college football. I am extremely thankful for this friendship.

Finally, and most importantly, I would like to thank the Lord for providing and guiding me through this period of my life.

# Contents

# List of Figures

# List of Tables

# Chapter 1

# Introduction

Radar systems typically utilize wideband waveforms that possess a narrow autocorrelation function main-lobe in order to achieve fine range resolution. The wideband radar waveform of choice is usually the linear-FM waveform, which has an instantaneous frequency that linearly increases with time. The wide-spread use of this waveform is mostly due to specific properties that allow for stretch processing, as explained in [17]. The stretched processed linear-FM waveform can then be sampled by an A/D converter with a sampling frequency that is less than what would be required for an arbitrary wideband waveform. In fact, until recently, the sampling rate of practical A/D converters has only been high enough to sample stretch-processed linear-FM waveforms and not an arbitrary wideband waveform. However, linear-FM waveforms have some disadvantages. For example, they have high range side-lobes, unless significant spectral tapering is applied to the receive signal (which sacrifices range resolution and degrades the signal-to-noise ratio). Furthermore, the set of linear-FM waveforms includes only two quasi-orthogonal waveforms, i.e. the "up-chirp" and "down-chirp".

With the development of A/D converters possessing sufficiently high sampling rates, wideband waveforms other than linear-FM waveforms are beginning to see use in applications with stringent requirements such as very low range side-lobes or a large quasi-orthogonal set. Arbitrary wideband waveforms can be designed in a number of ways. For example, minimum-shift keying can be used to embed a maximal-length sequence into a complex exponential [1]. This technique and others like it require a discrete-time sequence. Unfortunately, as is the case for maximal-length sequences, there is a limited number of possible sequences, and the length of these sequences is only defined for lengths of $2^k - 1$ samples (where k is a positive integer). Thus, although these waveforms have very low range side-lobes, they also have these two significant drawbacks, which are now explained in more detail.

Many emerging radar applications often require a set of hundreds, or even thousands, of distinct quasi-orthogonal waveforms. In a quasi-orthogonal waveform set, no single waveform significantly interferes with the detection of another waveform that is transmitted in the same frequency band and/or at the same time (this issue will be addressed further in Chapter 3). An example of a radar system that requires a quasi-orthogonal set is a multiple-input, multiple-output (MIMO) radar system. A MIMO radar system consists of multiple apertures, where each aperture is capable of transmitting and receiving radar waveforms [15]. In some modes of operation, a MIMO radar system requires that every transmitted waveform must be quasi-orthogonal with every other transmitted waveform being used at that time and every point of time in the past. Thus, in examples like this where large numbers (hundreds, thousands, millions, etc...) of quasi-orthogonal waveforms are required, finite-set sequences may not be useful due to an insufficient number of waveforms, since each quasi-orthogonal waveform is generated from a distinct sequence. However, as to be discussed in this thesis, extremely large sets of quasi-orthogonal waveforms can, in fact, be generated by exploiting the random nature of deterministic chaos.

An additional drawback to finite sets of fixed-length sequences is associated with their fixed-length. For example, the length of the maximal length sequences is limited to $2^k - 1$ where k is any positive integer. Therefore, if the application specifies a length between $2^k - 1$ and $2^{k+1} - 1$ then a maximal length sequence may not be applicable. On the other hand, waveforms derived from chaotic systems can be of any length since they are generated by integrating a chaotic system over an arbitrary time-interval.

Apart from finite-set, fixed-length sequences, techniques have been developed for generating other quasi-orthogonal radar waveforms, but these generation techniques require complicated numerical optimization algorithms [2]. On the other hand, some chaotic systems naturally lend themselves to a simple waveform generation procedures as explored in this thesis. The resulting procedure generates a large set of high-quality waveforms in a very short time interval (perhaps even on a pulse-by-pulse basis). The ability to develop a systematic waveform generation procedure with deterministic chaos is largely due to the structure and properties of chaotic systems, which are studied, in part, by many past publications such as [6], [7], [19], [9], and [8].

When using a chaos-based waveform, a well-designed receiver might also be able to exploit the self-synchronization property possessed by certain chaotic systems, which was discovered by Pecora and Carroll as explained in [13]. Self-synchronization offers potential benefits in channel equalization [5], high-speed long-distance communications [3], and other signal processing applications. Self-synchronization benefits are not discussed in this thesis although preliminary results of a self-synchronizing radar waveform are given in the appendix. The focus of this project, however, is just on the design of quasi-orthogonal radar waveforms via chaotic systems.

For all the above reasons, the use of deterministic chaos to generate large sets ($>$ 50) of quasi-orthogonal radar waveforms has been explored in the past and is explored further herein. Previously, chaos-based waveforms have been utilized in some of the radars located in Kwajalein Atoll [1]. However, many of these waveforms are actually based only loosely on deterministic chaos. In fact, generating each waveform requires computationally intensive numerical optimization algorithms [2]. This thesis presents a systematic radar waveform design technique, which is heavily based on deterministic chaos, which can be used to generate large sets of quasi-orthogonal waveforms. The chaotic system used in this thesis is the Lorenz system [10]. The generation technique developed is much less computationally intensive when compared to methods used to generate the previous chaos-based radar waveforms. Moreover, since the Lorenz system is a self-synchronizing chaotic system and since the transmitted waveforms are closely based on the original Lorenz waveform, the potential for exploiting the self-synchronization property exists.

## 1.1 Outline of Thesis

In this thesis, the use of the Lorenz system to generate radar waveforms is evaluated and then improvements to the waveforms are suggested. The details are organized into chapters as follows.

Chapter 2 summarizes deterministic chaos. In particular, an overview of the Lorenz system is presented. For a more detailed summary on chaos and the Lorenz system, refer to [4], [8], or [18].

Chapter 3 proposes four radar design goals, which will be used to evaluate the strengths and weaknesses of various waveforms presented throughout the thesis. These four design considerations include: (i) peak-to-RMS ratio, (ii) the autocorrelation function, (iii) the energy spectrum, and (iv) the cross-correlation function. To simplify the evaluation of the waveforms, the autocorrelation and cross-correlation functions were considered in place of the two-dimensional ambiguity and cross-ambiguity functions, although the results can also be illustrated with the ambiguity function as shown in the appendix.

Chapter 4 investigates how to select the Lorenz parameters, when generating Lorenz radar waveforms. Specifically, the parameters are varied to demonstrate the tradeoffs between the peak-to-RMS ratio, the autocorrelation function side-lobe level, and the bandwidth of a Lorenz waveform. Furthermore, this chapter discusses how to time-scale the state variables in two ways in order to set the bandwidth of the waveform.

Chapter 5, addresses practical issues associated with the Lorenz waveforms. The waveforms are compared against an industry standard, and the practical limitations are discussed. Transformations to the Lorenz waveforms are then suggested. The modified waveforms are again compared against (and outperform) an industry standard. Thus, the major result of Chapter 4 is a systematic waveform generation procedure, which is based closely on the Lorenz system. Moreover, this generation procedure is capable of quickly generating waveforms that meet and surpass current industry standards.

Finally, as described in the appendix, the waveforms designed in Chapter 4 were tested in a real radar at M.I.T. Lincoln Laboratory and preliminary results are presented.

# Chapter 2

# Overview of Chaotic Systems

This chapter presents an overview of chaos theory. However, it is not an all-inclusive introduction to the topic. For more information on chaos theory, refer to [8], [18], and [4].

As described in the introduction, deterministic chaos is used to generate very large sets of quasi-orthogonal waveforms. As similarly defined in [18], deterministic chaos herein will be loosely defined as a bounded, aperiodic flow with a sensitivity to initial conditions. Infinite numbers of continuous-time chaotic systems do exist [4], and there are several well-known, continuous-time chaotic systems such as the Lorenz system, the Rössler system, and the Double Scroll system. In general, the radar waveform properties of waveforms generated from a different chaotic system will be noticeably different. This thesis focuses on, perhaps, the most well-known chaotic system, the Lorenz system. While this thesis provides a deep understanding of how to generate radar waveforms from the Lorenz system, the concepts and tools developed herein can also be extended to other chaotic systems.

## 2.1 The Lorenz System

The Lorenz system is a well-studied chaotic system [10] named after Edward N. Lorenz. It is given in Eq. 2.1, and the three parameters $\sigma$, $r$, and $b$ are referred to as the Lorenz parameters.

$$\begin{aligned}\dot{x} &= \sigma(y-x) \\ \dot{y} &= rx - y - xz \\ \dot{z} &= xy - bz\end{aligned} \tag{2.1}$$

Assuming all parameters are greater than zero, all fixed points of the Lorenz are unstable if the following constraints are satisfied:

$$\sigma > b+1 \tag{2.2}$$

$$r > \frac{\sigma(\sigma+b+3)}{(\sigma-b-1)} \equiv r_c. \tag{2.3}$$

For sets of parameters which satisfy Eqs. 2.2 and 2.3, the Lorenz system might give rise chaotic dynamics or stable limit cycles. On the other hand, when $0 < r < r_c$, the Lorenz system will be heavily influenced by the presence of stable fixed points. When $0 < r < 1 < r_c$, the Lorenz system has a stable fixed point at $(x, y, z) = (0, 0, 0)$, and all solutions eventually approach this fixed point. When $1 < r < r_c$, two nontrivial and stable fixed points emerge at $(x, y, z) = (\pm\sqrt{b(r-1)}, \pm\sqrt{b(r-1)}, r-1)$, and the fixed point at the origin becomes unstable. When $r$ becomes greater than $r_c$, all the fixed points become unstable, and chaotic dynamics may ensue.

When the Lorenz system exhibits chaotic dynamics, the resulting trajectories described by the Lorenz system demonstrate a bounded, aperiodic flow with a sensitive dependence on initial conditions. The bounded, aperiodic flow of these trajectories can be verified by integrating the Lorenz equations and observing the nature of resulting trajectories. The Lorenz system can be approximately integrated via numerical integration techniques, for example, by using a fourth-order Runge-Kutta method with a step size equal to $10^{-3}$. A plot of each state variable of the Lorenz system can be seen in Fig. 2-1. The values for the parameters used in generating this plot were $\sigma = 267$, $r = 595$, and $b = 100$. The process for selecting the initial conditions will be explained at the end of this section. The boundedness and aperiodicity associated with a chaotic system can be observed from from Fig. 2-1. The state variables in this figure remain bounded. Also, if the time window was extended to reveal a longer section of the waveform in time, the state variables would be noticeably aperiodic.

In addition to boundedness and aperiodicity, a chaotic system also exhibits a sensitivity to initial conditions. For chaotic systems, two solutions with nearby initial conditions exponentially diverge. To demonstrate that the Lorenz system has this sensitivity, the $x$ state variable from two distinct solutions with nearby initial conditions are shown in Fig. 2-2. As can be seen by this figure, the two signals begin nearby and rapidly diverge from each other. Although only $x(t)$ is shown, the same behavior can be observed from both $y(t)$ and $z(t)$. Therefore, as can be seen in Figs. 2-1 and 2-2, the Lorenz system demonstrates a bounded, aperiodic flow with a sensitive dependence on initial conditions which is characteristic of any chaotic system.

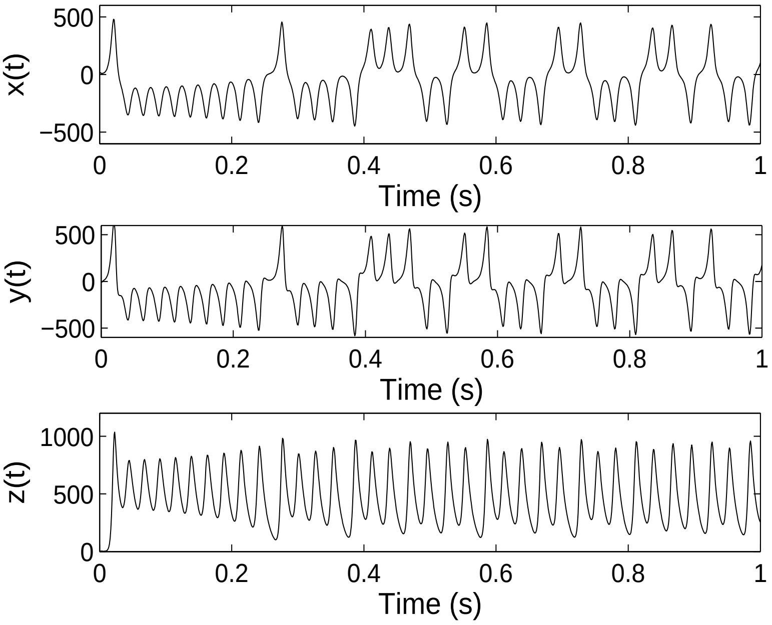

Figure 2-1: Time Window of the Trajectories of the State Variables of the Lorenz System.

For parameter values for which the Lorenz system demonstrates chaotic dynamics, all solutions, regardless of their initial conditions, converge to a set called the strange

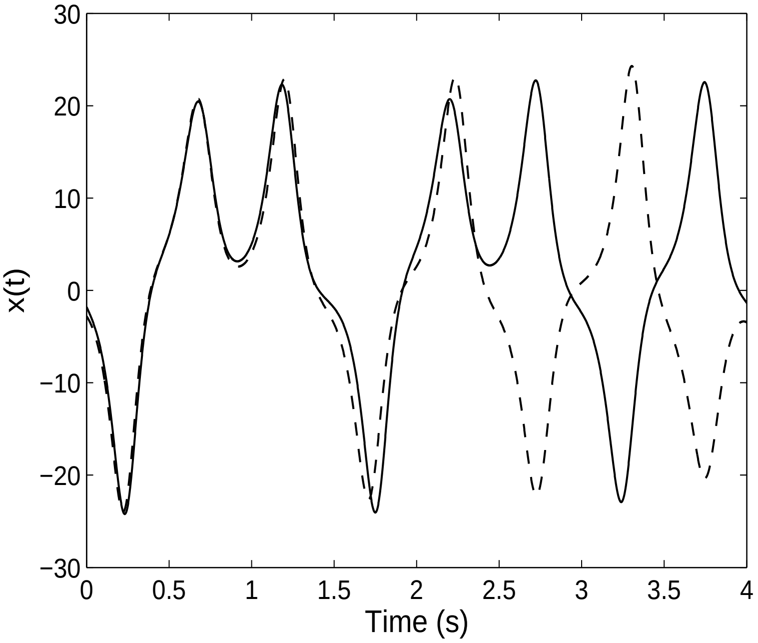

Figure 2-2: Time Window of Two Trajectories with Nearby Initial Conditions.

attractor. The strange attractor can be observed in state space (also called phase space) where each state variable is assigned a respective axis in the $x - y - z$ space. Figure 2-3 illustrates a solution to the Lorenz system tracing out the strange attractor in state space. Since the Lorenz system satisfies the uniqueness theorem [8], no points of intersection exist on the strange attractor. Nonetheless, all solutions eventually converge to the butterfly-shaped attractor. Specifically, the attractor is composed of two wings, and each wing of the attractor encircles one of the two nontrivial fixed points.

The attractor in Fig. 2-3 illustrates several characteristics of the Lorenz system. For example, the bounded, aperiodic nature of the Lorenz system is further demonstrated. Also, it is worth noting that the shape of the strange attractor actually varies for varying parameter values. This issue is addressed in Chapter 4. Additionally, an explanation can be easily given for the selection of the initial conditions when solving the Lorenz equations. In this thesis, the initial conditions are randomly selected from the attractor. Selecting the initial conditions on the attractor is accomplished by randomly selecting a three-dimensional point, $\{x_0, y_0, z_0\}$, from a cube enclosing the origin. The Lorenz system is then numerically integrated, with a step size of $10^{-3}$, using $\{x_0, y_0, z_0\}$ as the set of initial condition. Then, the first $10^4$ samples of the solution are discarded. Since empirical observations have shown that the solutions converge to the attractor after $10^4$ samples (for the Lorenz parameter values used in this thesis), the effective result is that the initial conditions are randomly selected from the attractor.

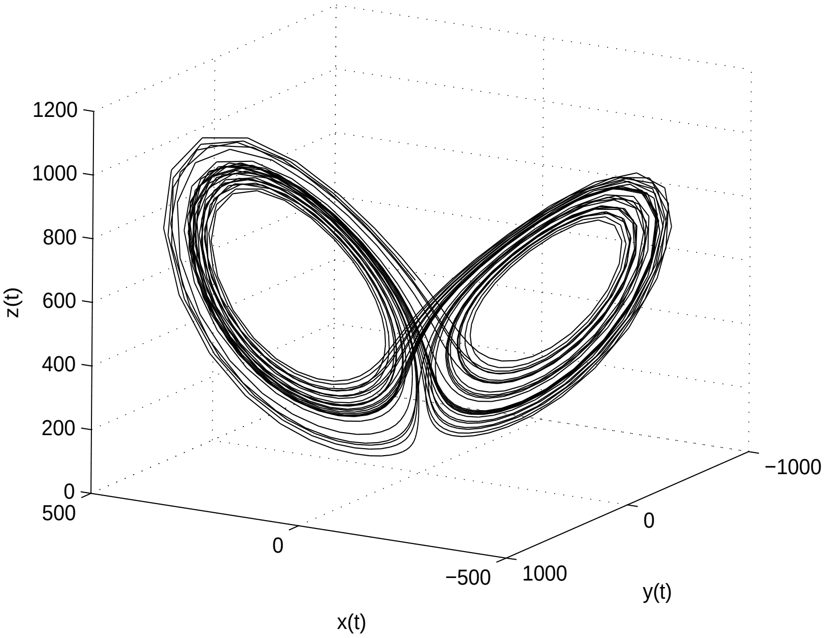

Figure 2-3: The Strange Attractor.

### 2.1.1 Bifurcations of the Lorenz System

As explained given in Eq. 2.3 of the previous section, when $r < r_c$, the Lorenz system is heavily influenced by stable fixed points. When $r > r_c$, all fixed points are unstable. At $r = r_c$, a bifurcation occurs. The word bifurcation is used to indicate when the qualitative dynamics of the Lorenz system change. The Lorenz system undergoes multiple bifurcations as $r$ is varied from 0 to $r_c$ (while $\sigma$ and $b$ remain constant), and consequently, $r$ is referred to as the bifurcation parameter. This section studies these bifurcations as $r$ is varied in order to understand the dynamics and attractor of the Lorenz system in more detail. The reference [8] provides an excellent description of these bifurcations, and the rest of this section summarizes relevant issues in Sections 2.4, 5.7, and 6.4 of [8]. The purpose for including the summary herein is to condense the relevant topics for the convenience of the reader, but for a more rigorous discussion, see [8].

The qualitative dynamics of the Lorenz system can be simplified and described by deriving a one-dimensional Lorenz map, which does not refer to the one-dimensional mapping in [10] discovered by Lorenz. The Lorenz map herein is derived by first defining a rectangle, $\Sigma$, as shown in Fig. 2-4 where $q^-$ and $q^+$ correspond to two nontrivial fixed points of the Lorenz system. As explained in Section 5.7 of [8] or as observed through numerical simulation, every time a trajectory travels around one wing of the attractor, the trajectory will eventually "pass down through $\Sigma$". As shown in Fig. 2-5, a Poincaré map[1] on $\Sigma$ can be calculated, and an observable boundary line, which will be called $B$, exists in $\Sigma$ where points on the left side correspond to trajectories that will proceed to rotate next around $q^-$ while points on the right side correspond to trajectories that will next rotate around $q^+$. It is assumed that this boundary is the intersection of $\Sigma$ and the stable manifold[2] of the origin, $W^s(p)$ [8]. As a notational simplification, a change of coordinates is performed, $(x, y) \longrightarrow (u, v)$, by rotating the x-y plane, and as a result, B is coincident with the line $u = 0$ as shown

---

[1] A Poincaré map is also known as a first return map and is explained in detail in pages 22-32 of [8].

[2] The stable manifold is the set of all trajectories that converge to the stable fixed point. For more details, refer to [8].

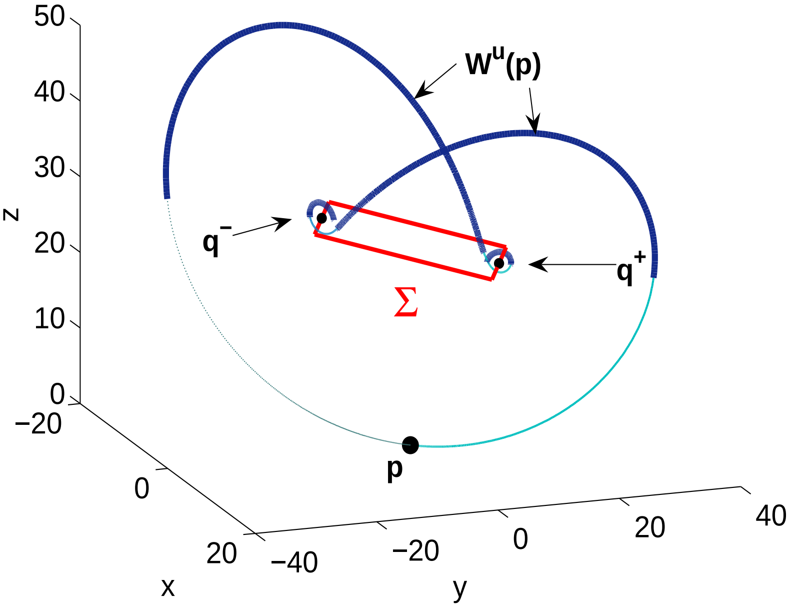

Figure 2-4: Definition of $\Sigma$. $\Sigma$, which lies in the $z = r - 1$ plane, stretches from $q^-$ to $q^+$. $W^u(p)$ is the unstable manifold of the origin. The segment of $W^u(p)$ that is above the plane $z = r - 1$ is colored dark blue, and the segment below $z = r - 1$ is colored light blue [8].

in Fig 2-5. With the change of coordinates, the $u$ coordinate, independently of the $v$ coordinate, specifies which wing of the attractor the trajectory will rotate around next. A mapping can be expressed mathematically as

$$\begin{pmatrix} u_{i+1} \\ v_{i+1} \end{pmatrix} = F(u_i, v_i) \tag{2.4}$$

where F, is a function used to relate consecutive points of the Poincaré map and $i$ indexes through all the points in time. As a further simplification, it is assumed that the $u$ coordinate completely specifies the value of the next $u$ coordinate, which is expressed mathematically in Eq. 2.5. This decoupling of the $u$ and $v$ coordinates is consistent with the nature of the observed boundary, B, and can be validated

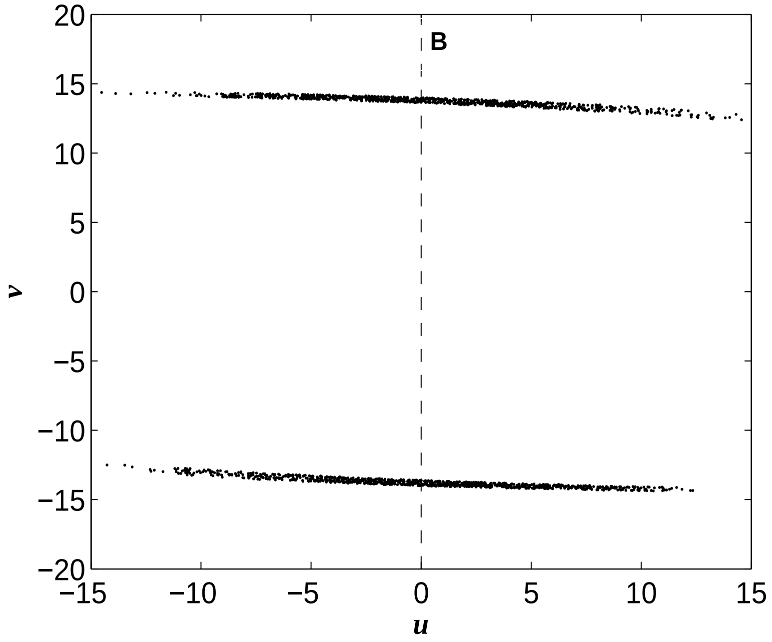

Figure 2-5: Poincaré Map on $\Sigma$. Each time a trajectory passes through $\Sigma$, the $(x, y)$ coordinates are recorded. For illustration purposes, a change of coordinates, $(x, y) \longrightarrow (u, v)$, is performed to rotate the $x - y$ plane. An observable boundary exists, B, such that all points on the left of B represent trajectories that rotate next around one wing of the attractor while points on the other side of B rotate around the other wing of the attractor. Also the upper cluster of points of this map all correspond to trajectories that just completed one loop around the same wing, and the lower cluster of points correspond to trajectories that just completed one loop around the other wing [8].

numerically as explained in [8].

$$\begin{pmatrix} u_{i+1} \\ v_{i+1} \end{pmatrix} = F(u_i, v_i) = \begin{pmatrix} h(u_i) \\ g(u_i, v_i) \end{pmatrix} \tag{2.5}$$

Thus, since consecutive $u$-coordinates have no dependence on the $v$-coordinate and since the $u$-coordinate completely specifies the wing a trajectory will rotate around next, $h(u_i)$ provides a one-dimensional mapping that qualitatively describes how the trajectory moves around the Lorenz attractor. This mapping is referred to as the

Lorenz map and is given in Eq. 2.6 and shown in Fig. 2-6.

$$u_{i+i} = h(u_i) \tag{2.6}$$

All points, $u_i$, to the left of the vertical line $u_i = 0$ represent trajectories that will rotate next around $q^-$ while points on the right correspond to trajectories that will rotate next around $q^+$.

As a notational clarification, successive iterations of Eq. 2.6 on an initial $u$-coordinate, $u_0$, will result in a sequence of $u$-coordinates that can be referred to as $u_n$. Also, for notational clarity, the fixed points of $h(u_i)$, which correspond to the fixed points of the Lorenz system, will also be denoted as $q^+$ and $q^-$.

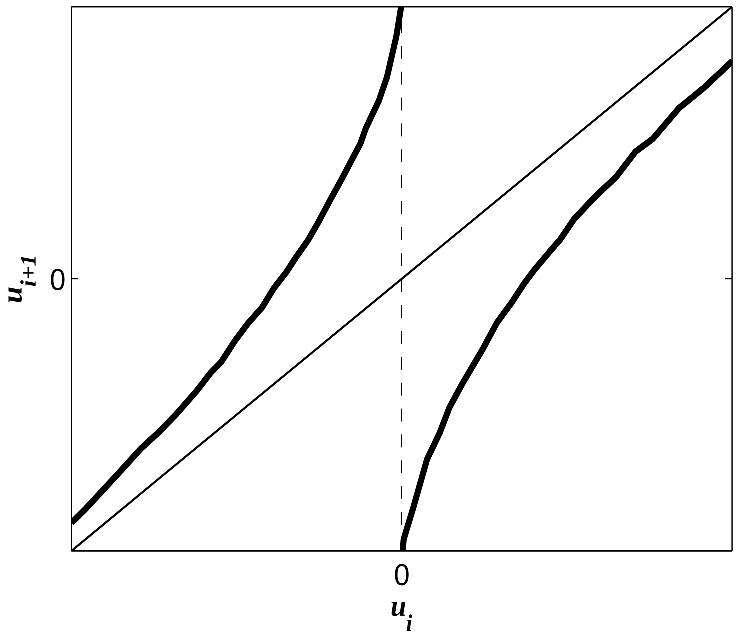

Figure 2-6: The Lorenz Map for $r > r_c$. This Lorenz map describes a Lorenz system exhibiting chaotic dynamics [8].

Using the Lorenz map, the qualitative dynamics of the Lorenz system are described as the bifurcation parameter is increased from zero. The dynamics when $r < 1$ are somewhat trivial. The Lorenz system has one, globally stable fixed point at the origin.

All trajectories converge to this fixed point. When $1 < r < r_c$, the fixed point at the origin becomes unstable, and the two nontrivial, stable fixed points, $q^+$ and $q^-$, emerge at $(x, y, z) = (\pm\sqrt{b(r-1)}, \pm\sqrt{b(r-1)}, r-1)$.

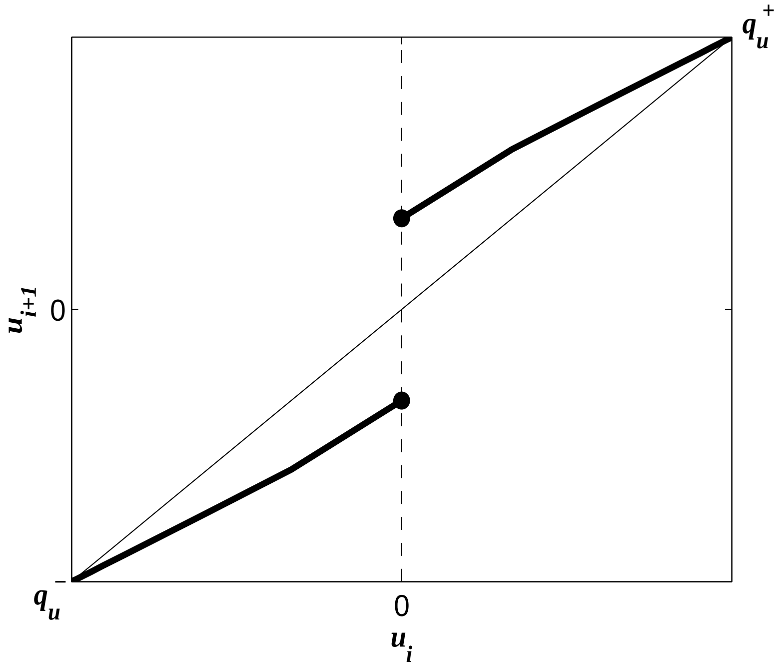

Figure 2-7: The Lorenz Map for $1 < r < r_h$. For this range of $r$, this map demonstrates that the sequence $u_n$ converges to the fixed points $q^+$ and $q^-$, which implies that all trajectories converge to the fixed points also [8].

When $r$ is marginally increased above unity, the Lorenz map is as given in Fig. 2-7. As shown in the figure, successive iterations of all points on one particular side of $u_i = 0$ will only give rise to points on the same side of $u_i = 0$, and these successive iterations will converge to either $q^+$ or $q^-$. Thus, the corresponding attractor dynamics are that all trajectories originating on one wing of the attractor will remain on that wing of the attractor and will converge to the appropriate fixed point, $q^+$ or $q^-$.

As explained more rigorously in [8], when $r$ increases, the Lorenz map indicates an interesting phenomenon. The endpoints of the Lorenz map on the line $u_i = 0$ begin to move toward each other along the line $u_i = 0$. Eventually, $r$ reaches a value,

$r_h$, where the endpoints of the Lorenz map meet at $(u_i, u_{i+1}) = (0, 0)$. This creates an unstable fixed point of the Lorenz map at $(u_i, u_{i+1}) = (0, 0)$. As $r$ increases above $r_h$, the endpoints of the Lorenz map begin to move apart along the line $u_i = 0$, and the unstable fixed point at $(u_i, u_{i+1}) = (0, 0)$ splits into two unstable fixed points, $f_p^+$ and $f_p^-$ as shown in Fig. 2-8. As $r$ continues to increase, $f_p^+$ and $f_p^-$ move in opposite directions along the line $u_{i+1} = u_i$ toward either $q^+$ or $q^-$, respectively.

The region of the Lorenz map corresponding to $u_i \in [f_p^-, f_p^+]$ is a chaotic-like region where, almost always, successive iterations of the Lorenz map will give rise to points that move around the region somewhat randomly until, eventually, an iteration maps a point outside the region $[f_p^-, f_p^+]$. Once a point jumps outside $[f_p^-, f_p^+]$, successive iterations will converge to either $q^+$ or $q^-$. The Lorenz map represents trajectories that appear chaotic-like for some finite time interval, but then eventually approach a fixed point. The behavior of the Lorenz system for the range of $r$ where $r_h < r < r_a < r_c$ is called *preturbulence* and is explained with more details in [8].

As $r$ is increased to $r_a$, the endpoints on the line $u_i = 0$, as well as $f_p^+$ and $f_p^-$, continue to separate until all points $u_i \in [f_p^-, f_p^+]$ map to points $u_{i+1} \in [f_p^-, f_p^+]$. Consequently, even though the fixed points $q^+$ and $q^-$ remain stable, a butterfly-like attractor for the system exists in the aforementioned range, but not all trajectories converge to this attractor. Many trajectories also converge to the fixed points $q^+$ and $q^-$.

When $r = r_c$, $f_p^+$ and $f_p^-$ reach $q^+$ and $q^-$, respectively. Then when $r$ is increased arbitrarily above $r_c$, all fixed points of the Lorenz map become unstable. At this point, practically all trajectories converge to the Lorenz attractor.

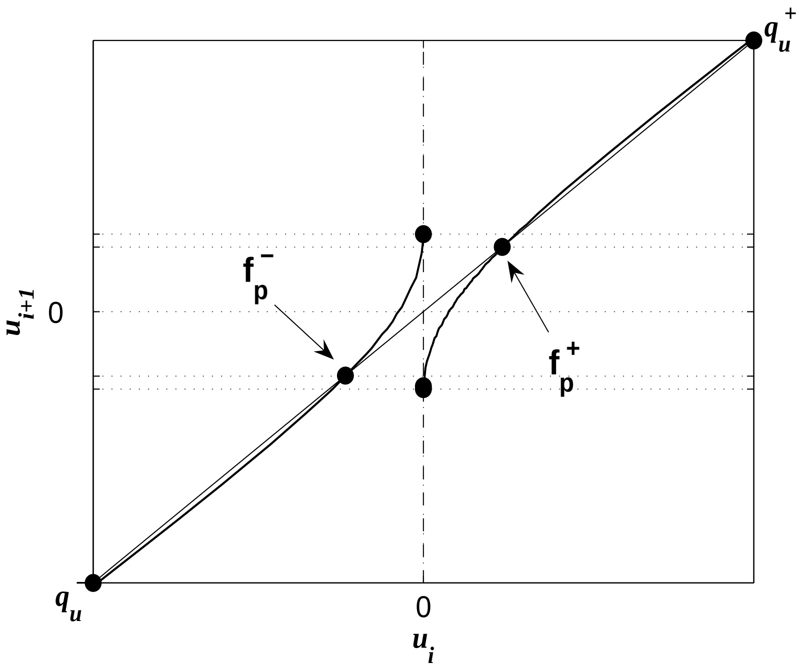

Figure 2-8: The Lorenz Map for $r_h < r < r_a$. For this range of $r$, almost always, successive iterations of the Lorenz map will give rise to points that move around somewhat randomly until converging to the fixed points. The Lorenz map represents trajectories that appear chaotic-like for some finite time interval, but then eventually approach a fixed point, which is called *preturbulence* [8].

# Chapter 3

# Radar Waveform Design Considerations

In Chapter 2, the background for the Lorenz system is presented. This chapter proposes four radar waveform design considerations, which will be used to evaluate the strengths and weaknesses of the waveforms based on the Lorenz system. However, before discussing various design considerations, an introduction to radar waveforms, based on relevant sections of [14], is briefly summarized in the next paragraph[1].

Any transmit radar waveform, $s(t)$, considered herein will be a real signal of the form shown in Eq. 3.1 where $a(t)$ and $\theta(t)$ are slowly varying when compared to $\omega_c$ [14]. Signals of this form will have a Fourier transform with energy concentrated around $\pm\omega_c$ [14].

$$s(t) \quad = \quad a(t)\cos(\omega_c t + \theta(t)) \tag{3.1}$$

Since $s(t)$ is real, its Fourier transform, $S(j\omega)$, is conjugate symmetric, which is mathematically expressed as $S(j\omega) = S^*(-j\omega)$. Consequently, $s(t)$ can be described as shown below where the first line follows from the definition of the inverse Fourier

---

[1] For a more detailed introduction, see Chapter 2 of the reference.

transform and the last line follows from the conjugate symmetric property of $S(j\omega)$.

$$\begin{aligned} s(t) &= \frac{1}{2\pi}\int_{-\infty}^{\infty} S(j\omega)e^{j\omega t}d\omega \\ &= \frac{1}{2\pi}\int_{-\infty}^{0} S(j\omega)e^{j\omega t}d\omega + \frac{1}{2\pi}\int_{0}^{\infty} S(j\omega)e^{j\omega t}d\omega \\ &= \frac{1}{2\pi}\int_{0}^{\infty} \left[S(j\omega)e^{j\omega t} + S^{*}(j\omega)e^{-j\omega t}\right] d\omega \end{aligned}$$

The last line can also be written as

$$s(t) = \Re\left\{\frac{1}{2\pi}\int_{0}^{\infty} 2S(j\omega)e^{j\omega t}d\omega\right\}. \quad (3.2)$$

Consequently, the positive frequencies of $S(j\omega)$ completely determine the signal $s(t)$. A complex function, $\psi(t)$, can be defined from the positive frequencies of $s(t)$ as shown in Eqs. 3.3 and 3.4. Substituting Eq. 3.3 into Eq. 3.2 and evaluating the resulting integral, which is defined in Eq. 3.4, relates $\psi(t)$ to $s(t)$ as shown in Eq. 3.5.

$$\Psi(j\omega) = \begin{cases} 2S(j\omega); & \omega > 0 \\ 0; & \omega < 0 \end{cases} \quad (3.3)$$

$$\psi(t) = \frac{1}{2\pi}\int_{-\infty}^{\infty} \Psi(j\omega)e^{j\omega t}d\omega \quad (3.4)$$

$$s(t) = \Re\{\psi(t)\} \quad (3.5)$$

Since the energy of $S(j\omega)$ is concentrated around $\pm\omega_c$, the energy of $\Psi(j\omega)$ will be concentrated around $\omega_c$. To center the energy of $\Psi(j\omega)$ around $\omega = 0$, a complex, base-band signal, $\mu(t)$, can be defined and related to $\psi(t)$ as shown in Eq. 3.6. Substituting Eq. 3.6 into Eq. 3.5 relates $s(t)$ and $\mu(t)$ as shown in Eq. 3.7. Rewriting the real component of Eq. 3.7 results in Eq. 3.8 where $|\mu(t)|$ and $\theta_\mu(t)$ denote the magnitude and phase of $\mu(t)$, respectively. As can be seen by comparing Eqs. 3.1 and 3.8, Eq. 3.8 is consistent with the form of a radar signal given in Eq. 3.1.

$$\psi(t) = \mu(t)e^{j\omega_c t} \quad (3.6)$$

$$s(t) = \Re\{\mu(t)e^{j\omega_c t}\} \tag{3.7}$$

$$s(t) = |\mu(t)|\cos(\omega_c t + \theta_\mu(t)) \tag{3.8}$$

In this thesis, all the waveforms are designed at base-band, and the base-band waveform, $\mu(t)$, will be related to the transmitted waveform via Eq. 3.7.

As typical in many engineering disciplines, waveform design involves various tradeoffs such as the tradeoff between bandwidth and the main-lobe width of the autocorrelation function. A second major waveform tradeoff is the tradeoff between waveform length (in time) and doppler precision as defined in [14]. Thus, waveform design involves various qualitative features, which makes the design procedure as much of an art form as a science.

Although waveform design involves various tradeoffs, this chapter attempts to quantify several radar waveform metrics in order to compare the quality of different radar waveforms. These metrics will be concentrated in four categories of interest: (i) peak-to-RMS ratio, (ii) the autocorrelation function, (iii) the energy spectrum, and (iv) the cross-correlation function. For example, metrics associated with the autocorrelation function would include main-lobe pulse-width and peak side-lobe level. Improving the metrics associated with the autocorrelation function will be considered one of the radar waveform design goals. Three additional design goals involve improving various metrics associated with the peak-to-RMS ratio, energy spectrum, and cross-correlation function.

Due to the various tradeoffs associated with waveform design, designing a ”good” radar waveform is a relative statement. Thus, the complex, base-band waveforms designed herein will be compared against a base-line radar waveform used in practice. The comparison will be based on the radar metrics associated with the four major design considerations presented in this chapter. In Chapter 5, the details of this comparison are presented.

## 3.1 Peak-to-RMS Ratio

One major design considerations is that transmitted waveform $s(t)$ should have a low peak-to-RMS ratio (PRMS). This design goal is a result of maximizing the output power from the radar transmitter to maximize the signal-to-noise ratio (SNR) at the receiver. The peak value of $s(t)$ is set by the saturation level of the transmitter, and the average power of $s(t)$ is designed to be as high as possible. Since the RMS level is the square root of the average power, the PRMS of $s(t)$ is designed to be as low as possible. For a perfect sine wave where the peak is one, the PRMS value would be approximately 1.414. Ideally, the PRMS of $s(t)$ should be close to 1.414. Constraining $s(t)$ to be close to 1.414 places a constraint on the base-band signal $\mu(t)$ as defined in Eq. 3.8.

This constraint on $\mu(t)$ can be determined by expressing the PRMS of $s(t)$ in terms of the PRMS of $\mu(t)$ where the carrier frequency $\omega_c$ (in Eq. 3.8) is assumed to be much greater than all significant frequencies of $\mu(t)$. The PRMS of $s(t)$ is calculated by first calculating the RMS value of $s(t)$, $s_{RMS}$, as shown in Eq. 3.9, where L is the length of $s(t)$ in time.

$$s_{RMS} = \sqrt{\frac{1}{L}\int_0^L s(t)^2 dt} \tag{3.9}$$

By substituting Eq. 3.8 into Eq. 3.9, the equation can be written as

$$s_{RMS} = \sqrt{\frac{1}{L}\int_0^L |\mu(t)|^2 \cos^2(\omega_c t + \theta(t))dt}. \tag{3.10}$$

The integral in Eq. 3.10 can be broken apart as shown in Eq. 3.11 where $T = \frac{2\pi}{\omega_c}$. Also, without loss of generality, $L$ is assumed to be a multiple of $T$.

$$s_{RMS} = \sqrt{\frac{1}{L}\sum_{k=0}^{L/T-1}\int_{kT}^{(k+1)T} |\mu(t)|^2 \cos^2(\omega_c t + \theta(t))dt} \tag{3.11}$$

Since $|\mu(t)|$ and $\theta_\mu(t)$ are assumed relatively constant on the interval from $[kT, (k+1)T]$, then $|\mu(t)|^2 \cos^2(\omega_c t + \theta(t)) \approx |\mu(kT)|^2 \cos^2(\omega_c t + \theta(kT))$ over this time interval.

Thus, Eq. 3.11 can be rewritten as Eq. 3.12.

$$s_{RMS} \approx \sqrt{\frac{1}{L}\sum_{k=0}^{L/T-1}|\mu(kT)|^2\int_{kT}^{(k+1)T}\cos^2(\omega_c t+\theta(kT))dt} \tag{3.12}$$

Since $\int_{kT}^{(k+1)T} cos^2(\omega_c t+\theta_\mu(kT))dt = \frac{T}{2}$, Eq. 3.12 can be re-written as in Eq. 3.13.

$$s_{RMS} \approx \sqrt{\frac{1}{2L}\sum_{k=0}^{L/T-1}|\mu(kT)|^2T} \tag{3.13}$$

By the definition of an integral and since $T$ is small on the time scale of $\mu(t)$, the summation in Eq. 3.13 can be approximated with an integral. Consequently, Eq. 3.13 can be written as

$$s_{RMS} \approx \sqrt{\frac{1}{2L}\int_0^L|\mu(t)|^2dt}. \tag{3.14}$$

Since the RMS value of $\mu(t)$, $\mu_{RMS}$, is $\sqrt{\frac{1}{L}\int_0^L|\mu(t)|^2dt}$, $s_{RMS}$ can be expressed as shown in Eq. 3.15.

$$s_{RMS} \approx \frac{\mu_{RMS}}{\sqrt{2}} \tag{3.15}$$

Since $\mu(t)$ is slowly varying when compared to $T=\frac{2\pi}{\omega_c}$, the peak of $\mu(t)$, $\mu_p$, is approximately equal to the peak of $s(t)$, $s_p$, which can be seen from Eq. 3.8. Consequently, the PRMS of $s(t)$, $s_{prms}$, can be approximated in terms of the PRMS of $\mu(t)$, $\mu_{prms}$, as shown in Eq. 3.16 where $\mu_{prms}$ is calculated according to Eq. 3.17.

$$\begin{aligned} s_{prms} &= \frac{s_p}{s_{RMS}} \\ &= \sqrt{2}\frac{\mu_p}{\mu_{RMS}} \\ &= \sqrt{2}\mu_{prms} \end{aligned} \tag{3.16}$$

$$\mu_{prms} = \frac{\mu_p}{\sqrt{\frac{1}{L}\int_0^L|\mu(t)|^2dt}} \tag{3.17}$$

As shown in Eq. 3.16, $s_{prms}$ will be approximately a factor of $\sqrt{2}$ greater than $\mu_{prms}$. The beginning of this section explained that $s_{prms}$ is desired to be close to 1.414. Consequently, $\mu_{prms}$ should be close to unity.

## 3.2 Autocorrelation Function

Another major design consideration is that the waveform should possess an autocorrelation function with both a narrow main-lobe and low side-lobes. For a complex, base-band waveform $\mu(t)$, we define the autocorrelation function, $r_{\mu\mu}(t)$, as in Eq. 3.18 and/or 3.19 where "$*$" denotes a convolution and "$^*$" denotes the complex conjugate.

$$\begin{aligned} r_{\mu\mu}(t) &= \mu(t) * \mu^*(-t) && (3.18) \\ &= \int_{-\infty}^{\infty} \mu(\tau)\mu^*(\tau - t)d\tau && (3.19) \end{aligned}$$

A typical autocorrelation function can be seen in Figure 3-1. As can be seen in the figure, the function has both a main-lobe and many smaller side-lobes.

The autocorrelation function is an important design consideration since, in traditional radar processing, the base-band signal, $\hat{\mu}(t)$, corresponding to the received signal, is matched filtered with a replica of the base-band signal, $\mu(t)$, corresponding to the transmit signal[2]. This filtering operation can be expressed as shown in Eq. 3.20.

$$r_{\hat{\mu}\mu}(t) = \hat{\mu}(t) * \mu^*(-t) \quad (3.20)$$

For an idealized point scatterer in a zero-noise environment, $r_{\hat{\mu}\mu}(t)$ equals a time delayed and amplitude scaled version of $r_{\mu\mu}(t)$ where the time delay is related to the distance to the target[3]. Thus, if a cluster of targets is approximated by a collection

---

[2] Relating the base-band signals to the transmit signals was described at the beginning of this chapter.

[3] To simplify this explanation, the doppler effect has been ignored. More information on this processing, including the doppler effect, is found in [17].

of idealized point scatters in a zero-noise environment, then the response of this group of targets, described by $r_{\hat{\mu}\mu}(t)$, is a linear superposition of the function $r_{\mu\mu}(t)$. Consequently, features of the autocorrelation function, such as the main-lobe width and side-lobe level, are extremely important in target detection and classification.

The main-lobe of $r_{\mu\mu}(t)$, centered around $t = 0$, is the maximum value of the function. The width of the main-lobe is desired to be as narrow as possible, since a narrower main lobe translates into a better capability of discriminating nearby targets. One of the radar waveform metrics associated with the autocorrelation function will be the main-lobe width. The main-lobe width will be evaluated by calculating the time duration[4] of the main-lobe of $r_{\mu\mu}(t)$ as given below where the integrals are evaluated from $-\infty$ to $\infty$.

$$\tau_d = \sqrt{\frac{4\int t^2\mu(t)^2}{\int \mu(t)^2} - \frac{\int t\mu(t)^2}{\int \mu(t)^2}} \tag{3.21}$$

In addition to a main-lobe, $r_{\mu\mu}(t)$ will also have many smaller side-lobes. Ideally, the autocorrelation function should have side-lobes as low as possible, since large, peaky side-lobes result in false targets and could mask the presence of true targets. Thus, the second radar waveform metric associated with the autocorrelation function is the magnitude of the peak side-lobe of the normalized autocorrelation function. This metric can be evaluated directly from the calculated autocorrelation function.

As explained in this section, the two metrics used in this thesis to evaluate the quality of the autocorrelation function are: (i) main-lobe pulse width and (ii) peak side-lobe value.

## 3.3 Energy Spectrum

A third radar waveform design consideration is that each radar waveform should have a compact energy density spectrum, which will be referred to as the energy spectrum of the waveform. The energy spectrum is defined as shown in Eq. 3.22 where $M(j\omega)$

---

[4] An explanation of the time duration can be found in [16].

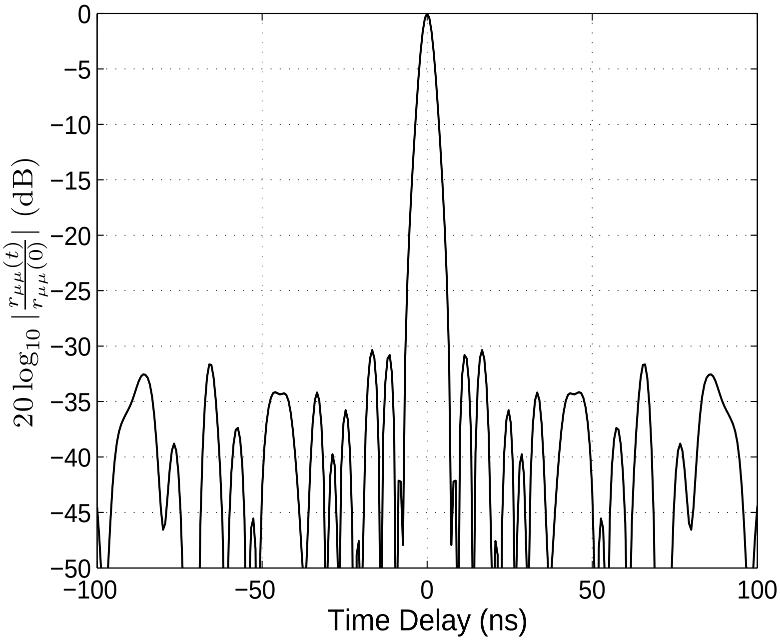

Figure 3-1: Autocorrelation Function of a Typical Radar Waveform.

is the Fourier transform of $\mu(t)$ [11].

$$\begin{aligned}\Phi_{\mu\mu}(j\omega) &= M(j\omega)M^*(j\omega) \\ &= |M(j\omega)|^2 \qquad (3.22)\end{aligned}$$

The energy spectrum can be related to the energy of $\mu(t)$ via Parseval's relation. Moreover, the inverse Fourier transform of Eq. 3.22 equals $r_{\mu\mu}(t)$. Thus, $r_{\mu\mu}(t)$ and $\Phi_{\mu\mu}(j\omega)$ are Fourier pairs as shown in Eq. 3.23 and 3.24.

$$\Phi_{\mu\mu}(j\omega) = \int_{-\infty}^{\infty} r_{\mu\mu}(t)e^{-j\omega t}dt \qquad (3.23)$$

$$r_{\mu\mu}(t) = \frac{1}{2\pi}\int_{-\infty}^{\infty} \Phi_{\mu\mu}(j\omega)e^{j\omega t}d\omega \qquad (3.24)$$

Figure 3-2 illustrates the energy spectrum of a typical waveform used in radar applications.

The energy spectrum of the waveform is desired to be compact over a given frequency range, $R$, in order to: (i) prevent the waveform from interfering with other radars operating outside $R$ and (ii) prevent the waveform's detection by receivers operating outside $R$. A compact spectrum, in general terms, means that

1. a large percentage of the energy of the waveform is concentrated within a continuous frequency range centered around $\omega = 0$, and
2. the energy outside this frequency range should be a low percentage of the overall energy of the waveform.

For example, the energy spectrum in Fig. 3-2 would be considered compact, since most of the energy in this spectrum is concentrated within 500 MHz of the center frequency.

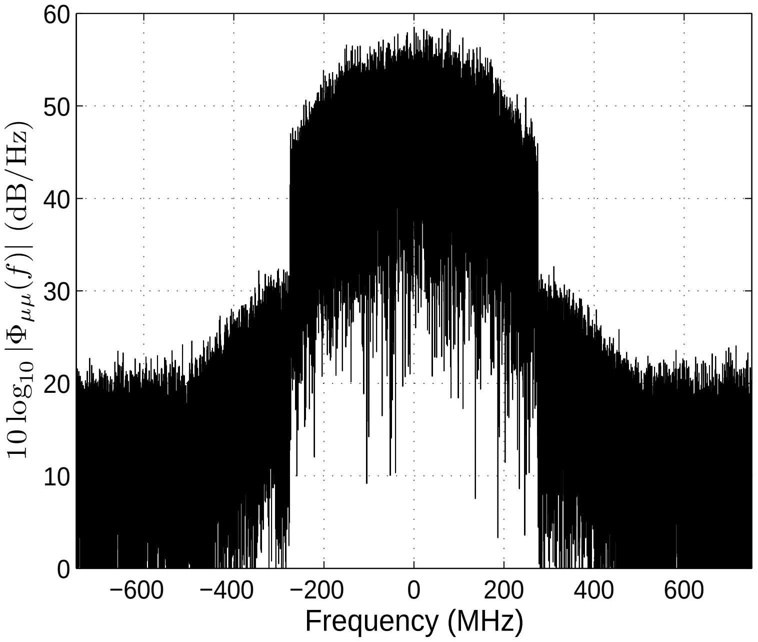

Figure 3-2: Energy spectrum of a Typical Radar Waveform. This graph of the energy spectrum illustrates the compact spectrum of a typical radar waveform.

Quantifying various properties of associated with the compactness of the energy spectrum is difficult but can be helpful when comparing the energy spectra of different waveforms. A particular quantification is made by determining the continuous frequency range containing 99.9% of the waveform's energy, which will be considered the in-band region of the waveform. The length of the in-band region will also be considered the bandwidth of the waveform. The frequency range outside the in-band region is the out-of-band region. The peak out-of-band side-lobe will be a metric associated with the energy spectrum that quantifies an important property of a compact spectrum. To measure this metric, the energy spectrum is normalized by the factor given in Eq. 3.25 where $N_{inband}$ is the number of samples in the in-band region and N is the total of samples of the discrete-time approximation of the continuous-time energy spectrum of the waveform.

$$norm = \frac{N_{inband}}{N^2} \tag{3.25}$$

The peak out-of-band side-lobe is then located and recorded. The peak out-of-band side-lobe can be used to approximately compare an important property of compactness: the amount of waveform energy that exists out of band.

## 3.4 Cross-correlation Function

A fourth radar design consideration is associated with the design of a large ($> 50$) set of quasi-orthogonal waveforms. A quasi-orthogonal set is a set where each waveform is quasi-orthogonal with every other waveform in the set. "Quasi-orthogonality" in this thesis means that the cross-correlation between any two distinct waveforms in a set must be "small." To explain this statement in more detail, both the cross-correlation and "small" are defined in this section. The cross-correlation of two waveforms is defined in Eq. 3.26 and 3.27.

$$\begin{aligned} r_{\mu\nu}(t) &= \mu(t) * \nu^*(-t) && (3.26) \\ &= \int_{\infty}^{\infty} \mu(\tau)\nu^*(\tau - t)d\tau && (3.27) \end{aligned}$$

In practice, the cross-correlation, $r_{\mu\nu}(t)$, is considered small if $20\log_{10}\left(r_{\mu\nu}(t)/r_{\mu\mu}(0)\right)$ is on the order of $-20\log_{10}\left(\sqrt{LB}\right)$ where $LB$ is the time-bandwidth product of the waveforms[5]. As evident from the name, the time-bandwidth product equals $L \cdot B$ where $L$ is the length of the waveform in time and $B$ is the bandwidth of the waveform.

An example of the cross-correlation of two quasi-orthogonal waveforms, $\mu(t)$ and $\nu(t)$, is illustrated by Figure 3-3. The cross correlation of the two waveforms is normalized by dividing by the peak autocorrelation function value of one waveform, $r_{\mu\mu}(0)$. The average cross-correlation level is located at approximately $-20\log_{10}(\sqrt{LB})$ $dB$. Consequently, the two waveforms are considered quasi-orthogonal. The radar waveform metric used to evaluate quasi-orthogonality will be the peak value of the normalized cross-correlation function.

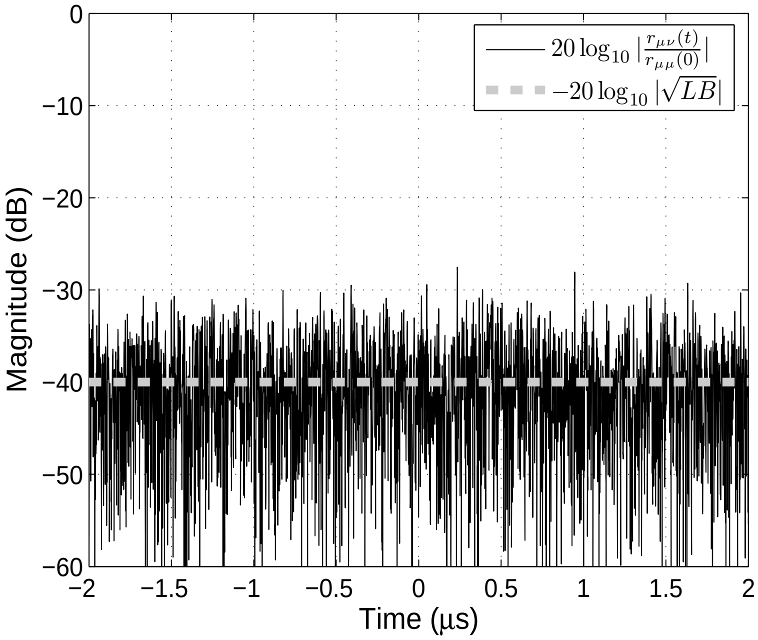

Figure 3-3: Cross-Correlation Function of Two Quasi-Orthogonal Radar Waveforms. The function is normalized by dividing the cross correlation by $r_{\mu\mu}(0)$. In this figure, $-20\log_{10}\left(\sqrt{LB}\right)$ was plotted with a horizontal, dotted line. The average side-lobe level is around $-20\log_{10}\left(\sqrt{LB}\right)$.

---

[5] Herein, $r_{\mu\mu}(0)$ is assumed to be approximately equal to $r_{\nu\nu}(0)$.

## 3.5 Radar Waveforms Designed from the Lorenz System

In Chapter 4 of this thesis, base-band radar waveforms will be derived from state variables of the Lorenz system. The Lorenz system is an excellent candidate system for generating radar waveforms due to various characteristics of deterministic chaos. For example, the bounded nature of the Lorenz system limits the magnitude of PRMS. Moreover, the aperiodicity of solutions and the sensitivity to initial conditions contribute to low side-lobes in both the autocorrelation and cross-correlation functions. Also, as will be shown in the remaining chapters, the energy spectra of the state variables are triangular-like, which provides a natural spectral control.

The state variable of the Lorenz system that best lends itself to radar waveform design is not initially clear. However, based on preliminary empirical studies, $x(t)$ was observed to evaluate better on the radar waveform metrics than $y(t)$ or $z(t)$. Moreover, no observable evidence suggested that a linear combination of state variables would be significantly better than $x(t)$. Thus as a simplification, all radar waveforms will be based on just $x(t)$. A Lorenz waveform, $x_L(t)$, will be defined as a normalized, time-windowed segment of the x-state-variable as shown in Eq. 3.28 where $L$ denotes the length of the waveform in time and $x_p$ denotes the maximum of $|x(t)|$ for the time interval where $t \in [0, L]$.

$$x_L(t) = \frac{1}{x_p} w_r(t) x(t) \tag{3.28}$$

$$w_r(t) = \begin{cases} 1; & t \in [0, L] \\ 0; & else \end{cases} \tag{3.29}$$

Throughout this thesis, all reference to $x_L(t)$ will refer to the Lorenz waveform as defined in Eq. 3.28, and $x(t)$ will refer to the state variable, $x$.

As explained in the first Section 2.1, the initial conditions will be arbitrarily chosen on the strange attractor at $t = 0$. What is actually done is that the initial conditions are chosen in a small cube encompassing the origin at a time, $t = -10$ seconds, and the solutions are assumed to converge to the strange attractor after 10 seconds.

In Chapter 5 of this thesis, the base-band radar waveform will not be directly extracted from the Lorenz system. The details related to constructing the radar waveform in Chapter 5 will be explained therein.

# Chapter 4

# The Effect of the Lorenz System Parameters on Radar Waveform Design Metrics

This chapter focuses on numerically and analytically exploring the Lorenz parameter space to determine how various radar waveform metrics vary as the parameters are varied. As explained in the previous chapter, these radar waveform metrics are associated with four major design considerations: (i) peak-to-RMS ratio, (ii) the autocorrelation function, (iii) the energy spectrum, and (iv) the cross-correlation function. Improving these metrics by varying the parameters gives rise to improved radar waveforms.

## 4.1 Peak-to-RMS Ratio

The first design consideration presented in Chapter 3 is associated with reducing the peak-to-RMS ratio (PRMS) of the Lorenz waveform, $x_L(t)$. Different Lorenz parameters were observed to affect the PRMS. This section numerically determines how the PRMS varies with different parameters and attempts to provide some insight into some attractor properties that contribute to a lower PRMS.

When numerically determining how the PRMS varies with the parameters, the parameter, $b$, is fixed while $\sigma$ and $r$ are varied. The rationale for fixing $b$ is that, as will be explained later, $b$ can be used to time-scale the state variables of the Lorenz system. Since a time-scaling will not affect the PRMS, the parameters $\sigma$ and $r$ can be varied to adjust the PRMS.

The $b$ parameter was set to 100, and $\sigma$ and $r$ were independently varied to numerically determine the effect on the PRMS. The constraints required to ensure unstable fixed points are $\sigma > b+1 = 101$ and $r > r_c$, which are given in Eqs. 2.2 and 2.3. Thus when $\sigma$ and $r$ were varied, they were greater than these minimal values. Moreover, preliminary studies demonstrated that ranges of $\sigma$ and $r$ relevant to the radar waveform metrics were $\sigma \in (200, 850)$ and $r \in (r_c, 1.6r_c)$. For each combination of $\sigma$ and $r$, the Lorenz system was numerically integrated over one hundred seconds to give rise to $x_L(t)$. The PRMS of $x_L(t)$ is then determined by averaging over three trials. The results are shown in Fig. 4-1. The figure demonstrates that as $\sigma$ increases, the PRMS likewise increases. Also, as $r$ increases, the PRMS again increases. Thus as can be verified by Fig. 4-1, the parameters that give rise to an $x_L(t)$ trajectory with the lowest PRMS are the values of $\sigma$ and $r$ in the lower left-hand corner of the figure. Since in this thesis, it is desirable to operate with a $PRMS < 2.3$, a two-dimensional plot of the lower left-hand corner of Fig. 4-1 is shown in Fig. 4-2.

Two system trends that affect the PRMS of the Lorenz waveform were observed. The first trend indicated that as $\sigma$ increased, the trajectory of the Lorenz system (in state-space) traveled a longer path from one maximum to the next maximum. This trend was not addressed in this thesis. The second trend concerns distance separating the minimum and maximum relative maximum of $x_L(t)$ for various values of $\sigma$ and $r$, which is investigated herein.

Relating the distance separating the minimum and maximum relative maximum of $x_L(t)$ to the attractor is accomplished by analyzing an example. The attractor of two distinct Lorenz systems was analyzed for the following sets of parameters: $\{\sigma = 200, r = r_c, b = 100\}$ and $\{\sigma = 300, r = 1.6r_c, b = 100\}$. The former set of parameters gives rise to a Lorenz system with a lower PRMS than the one with the latter set of parameters. For convenience, System A and System B will denote the

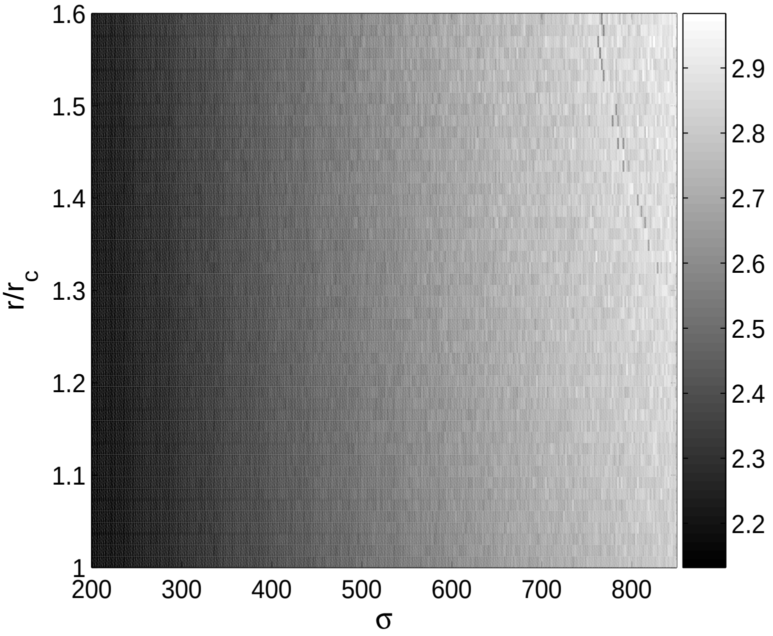

Figure 4-1: Peak-to-RMS Ratio as a Function of $\sigma$ and $r$. This figure was created from a Lorenz system with $b = 100$ and varying values of $\sigma$ and $r$. For a particular value of $\sigma$ and $r$, the system was numerically integrated three times for distinct initial conditions with a step size of $10^{-3}$ seconds. The peak-to-RMS Voltage ratio was calculated for each of the three solutions and then averaged together.

former and latter parameter sets, respectively.

An $x$-$z$ slice of the attractor for System A and System B is shown in Fig. 4-3 to demonstrate the attractor differences between these systems, where the attractor shown in the figure has been normalized so that the peak value of each state variable is equal to unity. In this figure, a time-windowed solution traces out a trajectory on the attractor, which is shown in state space. By comparing the trajectories from the two systems qualitatively, the trajectory of System A appear to wrap more tightly around the attractor than the trajectory of System B. In other words, the attractor can be thought of as two separate butterfly wings. Each wing consists of several rings, which are segments of the trajectory that wrap once around one of the wings. Both System A and System B have an outermost ring where the solution stretches the

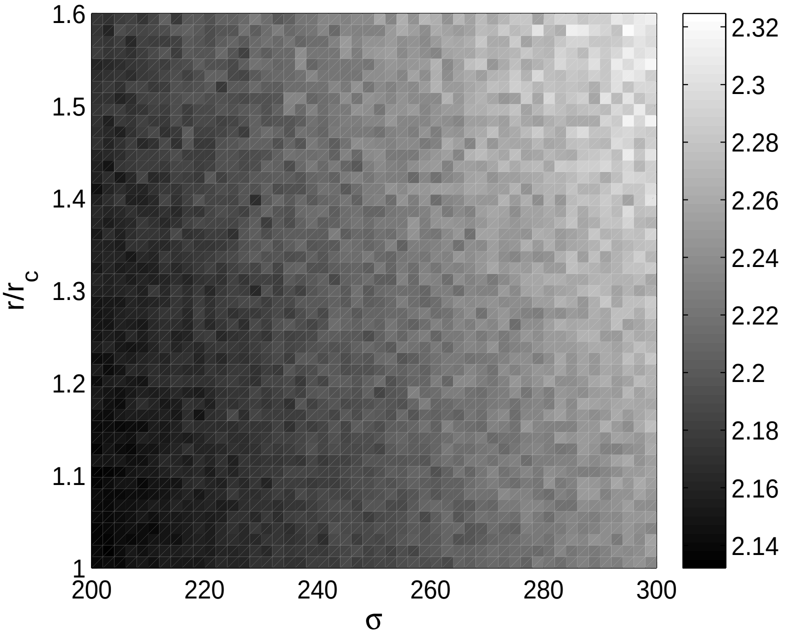

Figure 4-2: Peak-to-RMS Ratio as a Function of $\sigma$ and $r$.

greatest distance from the origin. However, since the rings of System A wrap more tightly than System B, the rings of System A are assumed to, on average, lie closer to the outermost ring of System A than the case for system B.

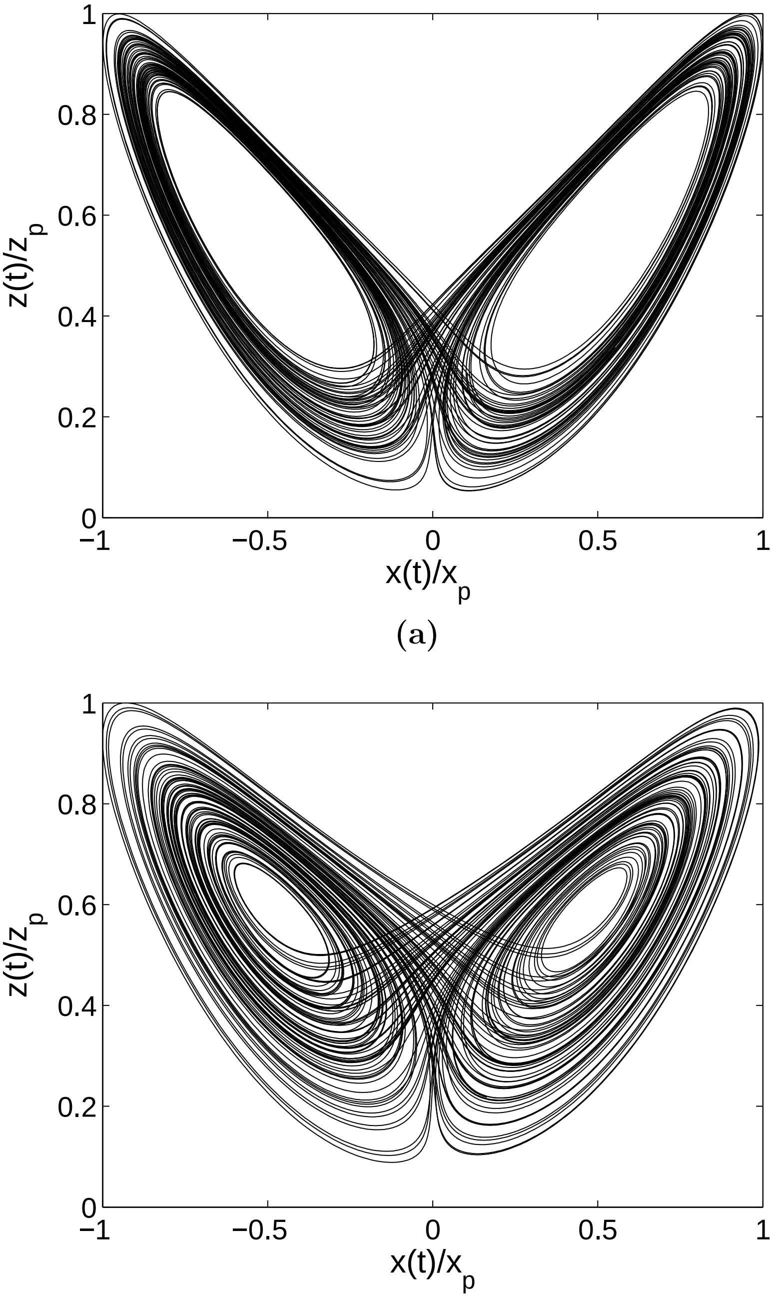

**(a)**

**(b)**

Figure 4-3: Slices of the Attractor for Two Distinct Lorenz Systems. The state variable have been normalized by their respective peak values, i.e. $x_p = max(|x(t)|)$. The system in (a) was derived from a Lorenz system with a parameter set of $\{\sigma = 200, r = r_c, b = 100\}$ and has a PRMS of $\approx 2.15$. The system in (b) was derived from a Lorenz system with a parameter set of $\{\sigma = 300, r = 1.6r_c, b = 100\}$ and has a PRMS of $\approx 2.41$.

To quantify this relationship further, a metric called wing width of a typical solution is defined. For the time-windowed x-state-variable, which will be called $x_w(t)$, wing width will be defined as the Euclidean distance between the minimum relative maximum of $|x_w(t)|$ subtracted from absolute maximum of $|x_w(t)|$ as shown in Eq. 4.1 where $p_x$ represents the set of relative maximums of $|x_w(t)|$ over a certain time interval. The wing width is normalized with the peak value of x(t) so that $W_x$ from distinct systems can be compared.

$$W_x \quad = \quad \frac{1}{max(p_x)}[max(p_x) - min(p_x)] \tag{4.1}$$

Figure 4-4 illustrates $W_x$ graphically on the attractor for a Lorenz system with the parameters set of $\{\sigma = 300, r = 1.6r_c, b = 100\}$.

It is important to clarify that the wing width is calculated based on a particular time-windowed solution to the Lorenz system, not an infinitely long time segment that traces out the entire attractor. In other words, the wing width metric is associated with a time-windowed $x_w(t)$ for a given set of parameters, $\{\sigma, r, b\}$, and for a given time interval, which in this experiment was 100 seconds. Therefore, by averaging the wing width over several distinct solutions of the same length in time, the mean value is, more or less, the typical wing width for that set of parameters and that time interval[1]. Moreover the concept of wing width is a legitimate indicator of the PRMS of the Lorenz waveform, $x_L(t)$, for the two following reasons: every radar Lorenz waveform is a normalized time-windowed x-state-variable, and it is easy to intuitively understand and numerically verify how the averaged wing width relates to the PRMS of $x_L(t)$ as explained next.

Specifically, a larger wing width intuitively suggests that rings have the flexibility to vary greatly from the outermost ring, or in other words, the relative extrema of $|x_w(t)|$ have the flexibility to vary greatly from the global extremum. This flexibility to vary greatly reduces the average power of $x_L(t)$ with respect to the peak value

---

[1] The concept of wing width may not be the most mathematically rigorous way to justify how the peak-to-RMS ratio is related to the Lorenz attractor. However, it was chosen since it was easy to depict its relation to the attractor graphically.

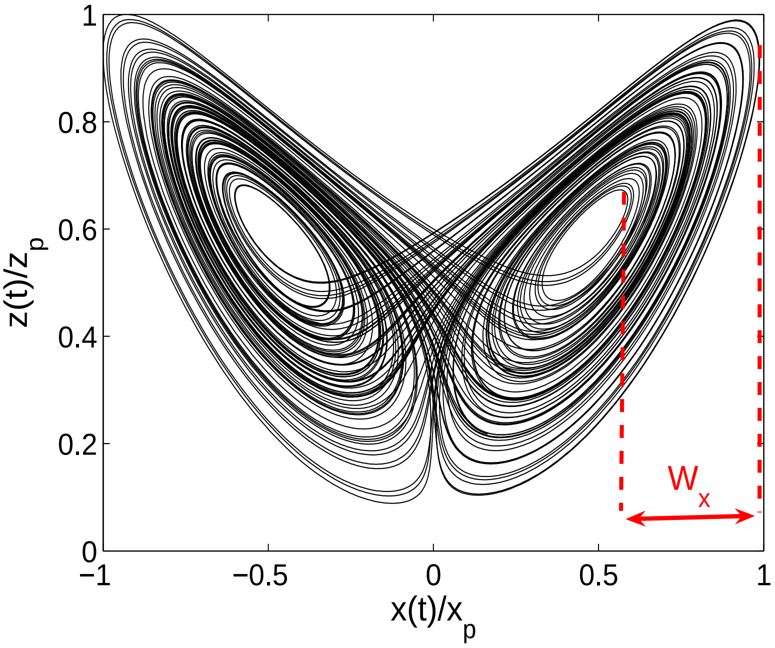

Figure 4-4: The Wing Width of the Attractor. This figure plots an $x$-$z$ slice of the attractor for the Lorenz system with $\sigma = 300, r = 1.6r_c, b = 100$. The wing width, $W_x$ for this attractor is shown in red.

of $x_L(t)$. Thus the larger the wing width, the higher the PRMS of $x_L(t)$. To verify this statement numerically, $W_x$ was calculated for Lorenz systems with varying values of $\sigma$ and $r$ with $b = 100$. $W_x$ was calculated by numerically integrating the Lorenz equations for a given set of parameters and random initial conditions. Three distinct, 100 second solutions were generated, and $W_x$ was calculated for each of the three solutions. The mean of the three calculations was recorded as the wing width for that particular Lorenz system with that particular set of parameters. The parameters were varied in the ranges $\sigma \in (200, 300)$ and $r \in (r_c, 1.6r_c)$. The results are shown in Fig. 4-5. This figure demonstrates that increasing $\sigma$ will increase the wing width, and increasing $r$ will also increase the wing width. Since increasing $\sigma$ and $r$ will also increase the PRMS, the numerical results suggest that the wing width is, in fact, related to the PRMS of $x_L(t)$.

In summary, the main result of this section is that lower values of both $\sigma$ and $r$

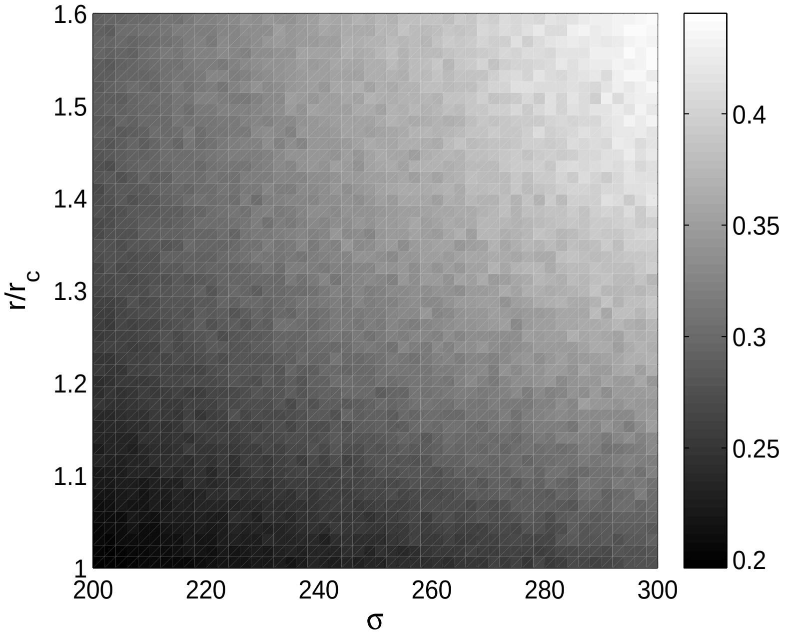

Figure 4-5: Wing Width as a Function of $\sigma$ and $r$. This figure corresponds to a Lorenz system with $b = 100$ and varying values of $\sigma$ and $b$. For a particular value of $\sigma$ and $r$, the system was numerically integrated three times for distinct initial conditions with a step size of $10^{-3}$ seconds. $W_x$ was calculated for each of the three solutions and then averaged together.

will lead to a lower values for the PRMS. Moreover, the peak-to-RMS ratio appears to be related, in part, to how tightly trajectories wrap around the attractor, and the wing width was a simple evaluation metric for the tightness of this wrapping.

## 4.2 Autocorrelation Function

Another design consideration of radar waveforms deals with improving metrics associated with the autocorrelation function. Improving these metrics implies decreasing the the main-lobe width and decreasing the magnitude of the peak side-lobe. This section summarizes a numerical study on how to minimize the magnitude of the peak side-lobe and explains why control of the main-lobe width will be considered when discussing the energy spectrum of the Lorenz waveform.

The variation in the main-lobe width was observed to be due to a difference in bandwidth and not some other chaotic system property, which can be intuitively explained utilizing 2 key points. First, the autocorrelation function and the energy spectrum are Fourier pairs. Second, the energy spectrum of $x_L(t)$ has the same triangular-like shape (as shown in Fig. 4-6) for any set of parameters that makes the Lorenz system chaotic. Consequently, the main-lobe of the autocorrelation function is closely related to the bandwidth of the energy spectrum (see [16] for further details). Therefore, to decrease the main-lobe width of the autocorrelation function, the bandwidth should be increased, which is explained in Section 4.3. The remainder of this section considers reducing the side-lobe level of the autocorrelation function.

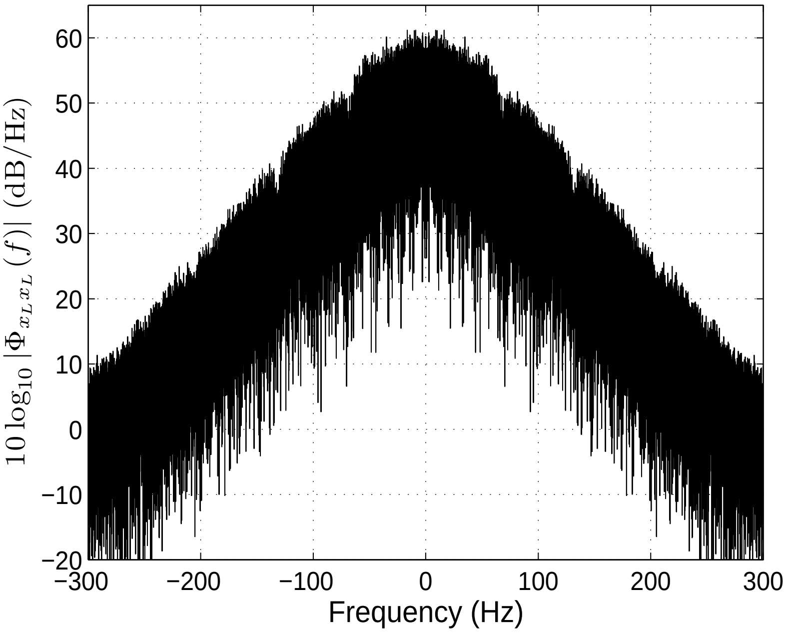

Figure 4-6: Energy Spectrum of a Lorenz Waveform.

The magnitude of the peak side-lobe of the autocorrelation function is very dependent on the particular parameters used in the Lorenz system. Accordingly, it is an important radar waveform metric when comparing radar waveforms from Lorenz systems with different sets of Lorenz parameters. As explained in Section 4.1, $b$ is fixed to equal 100, and it will be used to scale Lorenz waveform in time. Since time scaling a $x_L(t)$ has no effect on the magnitude of the peak sid-lobe, the rest of this section attempts to understand how this metric varies with the parameters $\sigma$ and $r$.

To demonstrate the relationship between the magnitude of the peak side-lobe and the parameters, the peak side-lobe is determined empirically for various combinations of $\sigma$ and $r$. To maintain chaotic dynamics, $\sigma$ and $r$ were chosen such that $\sigma \in (200, 850)$ and $r \in (r_c, 1.6r_c)$. For each combination of $\sigma$ and $r$, the Lorenz system was numerically integrated over one hundred seconds to give rise to $x_L(t)$. The peak side-lobe of the autocorrelation function was determined. This process was repeated three times for each combination of $\sigma$ and $r$, and the mean was computed and recorded. Figure 4-7 shows the average magnitude of the peak side-lobe for a given $\sigma$ and $r$. For $b = 100$, this plots shows the combinations of $\sigma$ and $r$ that minimize the side-lobes of $x_L(t)$.

The dependence of the peak side-lobe on the Lorenz parameters is due to the underlying Lorenz system properties. These properties can be explained by first considering the autocorrelation function of a Lorenz waveform. There are three main regions of the autocorrelation function of a chaotic waveform. One region is a region containing the distinguishable main-lobe. Adjacent to the main-lobe are several, smaller, but yet still distinct, side-lobes, which will be contained in a region referred to as the side-lobe region. Beyond this region is a region that will be referred to as the autocorrelation noise. These three regions can be seen in Fig. 4-8. Ideally, both the autocorrelation noise and the side-lobe region should be minimized as much as possible.

For an $x_L(t)$ with a fixed length in time, the level of the autocorrelation noise was observed to be set by the bandwidth of the system. A waveform with a larger bandwidth gives rise to a waveform whose autocorrelation function has a lower autocorrelation noise level. The autocorrelation noise level was not observed to be dependent on certain combinations of parameters, unless these sets of parameters affected the bandwidth of $x_L(t)$. Using the parameters to set the bandwidth (and correspondingly the autocorrelation noise) is discussed in detail in the next section.

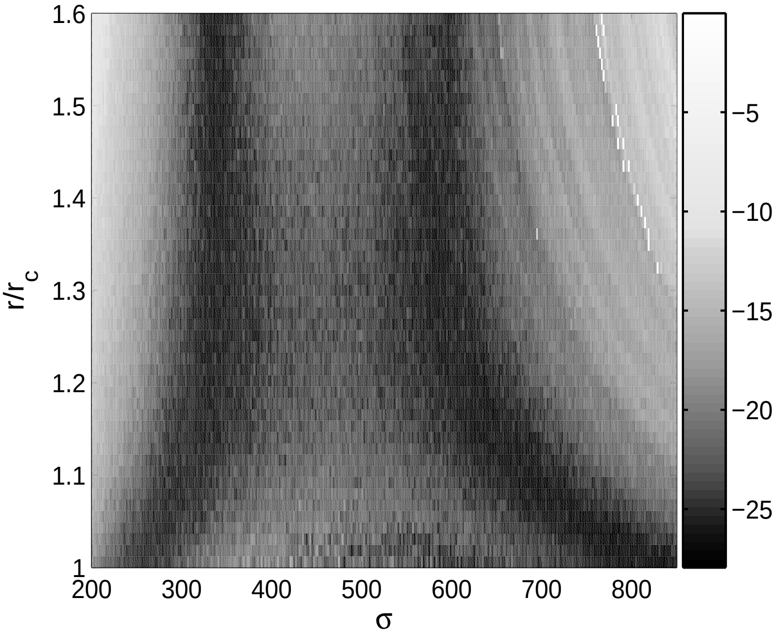

Figure 4-7: Peak Side-lobe of the Lorenz System for $b = 100$ and Varying Values of $\sigma$ and $r$. For a particular value of $\sigma$ and $r$, the system was numerically integrated three times with a distinct set of initial conditions with a step size of $10^{-3}$ seconds. The peak side-lobe that was recorded was the mean peak side-lobe of the three trials.

Moreover, since the level of the autocorrelation noise was not observed to be affected by carefully selecting the Lorenz parameters and since in most cases, the autocorrelation noise was observed to be less than the level of the side-lobes contained in the side-lobe region, the issue of reducing the magnitude of the peak side-lobe involves minimizing the side-lobes in the side-lobe region, which can be reduced to about the same level as the autocorrelation noise[2]. In the remainder of this section, when the word side-lobe is used, it refers to one of the side-lobes contained in the side-lobe region depicted in Fig. 4-8.

The side-lobes of the autocorrelation function are due to the structure of the

---

[2] In these cases, it may be true that the peak of the autocorrelation noise may be higher than the peak of the side-lobe region, but this behavior could not be controlled by varying the Lorenz parameters. Moreover, this peak in the autocorrelation noise is usually far enough away from the main-lobe of the autocorrelation function that it is insignificant in most applications.

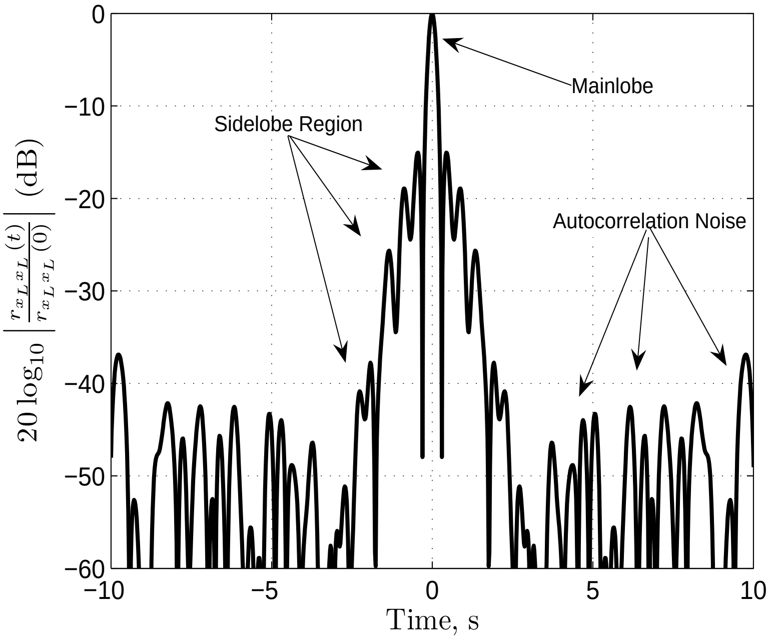

Figure 4-8: Typical Autocorrelation Function of a Lorenz Waveform. For future reference, this figure labels the main-lobe, side-lobes, and autocorrelation noise of the autocorrelation function.

Lorenz system. As evident from the Fig. 2-3, a Lorenz trajectory confined to the attractor demonstrates certain ordered dynamics. The trajectory will loop around one wing of the attractor an arbitrary number of times until eventually transitioning to the next wing. This structure of the Lorenz system exists for any chaotic Lorenz system, despite the parameters.

Since the state variable, $x(t)$, is the projection of the trajectory onto the $x$-axis, the dynamics of $x(t)$ can be understood from the dynamics of a trajectory on the attractor. For example, in a time period during which $x > 0$, the trajectory on the attractor could move outward around a wing of the attractor, then continue to move around toward the origin. The trajectory could then repeat this pattern, for example, one more time and begin to move around the same wing twice. The behavior corresponds to $x(t)$ approaching a relative maximum, then moving back toward zero. Before reaching zero, $x(t)$ moves through a relative minimum and begins rising again toward a second consecutive relative maximum.

A simple analysis on the amount of time separating two consecutive maximum of $|x(t)|$ reveals that consecutive maxima appear to be separated by approximately the same time interval[3]. Before further discussion of this timing issue, two notational issues are clarified. The relative maxima of $|x(t)|$ will be referred to as the peaks of $x(t)$. Also, the time interval between consecutive peaks of $x(t)$ will be denoted as the random variable $\Delta$. Now, this timing issue can be described mathematically by saying, a random sample of $\Delta$ appears to cluster very close to the mean of $\Delta$, $\mu_\Delta$. To verify this clustering, a histogram of a random sample from $\Delta$ is given in Fig. 4-9 for $x(t)$ from a Lorenz system with $\sigma = 8.05$, $r = 49.72$, and $b = 4.0$. The mean of $\Delta$, $\mu_\Delta$, was estimated to be 0.51 seconds. As can be seen from Fig. 4-9, the random sample from $\Delta$ clusters around 0.51 seconds. Consequently, if a peak of $x(t)$ arrives at a certain time, $t_0$, then another peak is likely to arrive around $t_0 + \mu_\Delta$. Thus, information on the location, in time, of the next peak is contained in the location, in time, of the previous peak.

Consecutive peaks separated by approximately $\mu_\Delta$ will have a significant effect on the location and amplitude of the side-lobes of the autocorrelation function. This effect can be best explained by example. Assume that a Lorenz system gives rise to trajectories that have the following property. After a trajectory completes a rotation around one wing of the attractor, it is twice as likely for the trajectory to transition to the other wing than remain on the same wing. For any such trajectory, consecutive peaks of $x(t)$, which are separated by $\mu_\Delta$, will be twice as likely to be of opposite sign than of the same sign. Therefore, the autocorrelation function will have a sizeable negative side-lobe at $\mu_\Delta$ since $r_{xx}(\mu_\Delta) = \int_{-\infty}^{\infty} x(\tau)x(\tau-\mu_\Delta)^* d\tau$ will line up a relatively large number of peaks of opposite sign.

Figure 4-10 demonstrates this principle with the Lorenz system used to generate the histogram in Fig. 4-9. This system was observed to give rise to trajectories that are more likely to transition to the next wing rather than remain on the same wing of

---

[3] $|x(t)|$ is used as opposed to just $x(t)$ since we are considering the arrival of both the positive and negative peaks of $x(t)$.

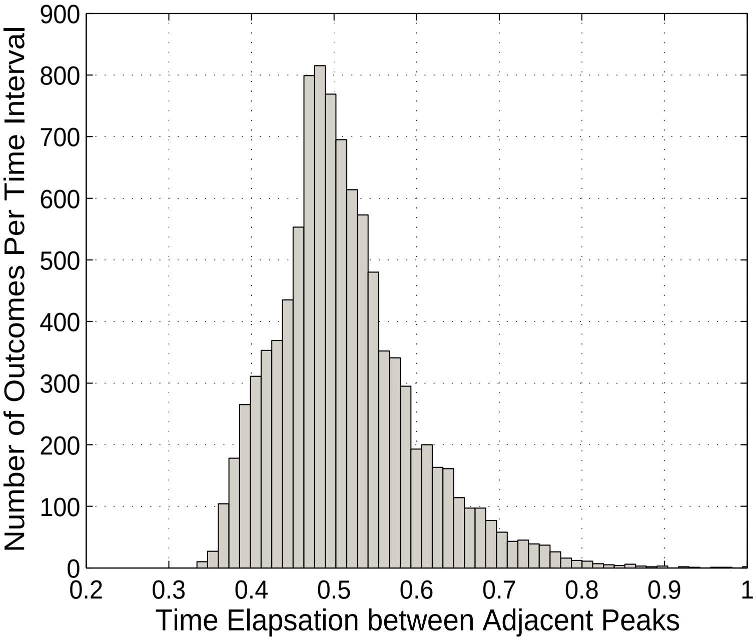

Figure 4-9: Histogram for the Distance in Time Between Consecutive Relative Extrema of $x(t)$, $\Delta$.

the chaotic attractor. Also, as shown by Fig. 4-9, consecutive peaks are separated, on average, by approximately 0.51 seconds. Consequently as explained in the previous paragraph, the autocorrelation function is predicted to have a side-lobe at $t \approx 0.51$. The autocorrelation function for $x(t)$ is shown in Fig 4-10. As can be seen in the figure, a large side-lobe is present at $t \approx 0.51$ (although the peak of this side-lobe actually occurs at 0.44).

By understanding the timing dynamics responsible for high side-lobes of $x(t)$, a method for reducing the side-lobe level can be suggested. Since the timing dynamics of the Lorenz system ensure that consecutive peaks of $x(t)$ will remain at about $\mu_\Delta$, the only way to reduce the side-lobes of the Lorenz system is to ensure that a trajectory is equally likely to proceed to the next wing as to remain on the same wing, which is equivalent to saying that $x(t)$ will have approximately the same number of consecutive same-signed peaks as opposite-signed peaks. In this way, the value of the autocorrelation function at $\mu_\Delta$ (as shown in Eq. 4.2) will be reduced since the positive value due to consecutive same-sign peaks will cancel with the negative value due consecutive opposite-sign peaks.

$$r_{xx}(0.44) = \int_{-\infty}^{\infty} x(\tau)x^*(\tau - 0.44)d\tau \tag{4.2}$$

The likelihood that a trajectory jumps to the next wing as opposed to remaining on the same wing depends on the parameters of the Lorenz system.

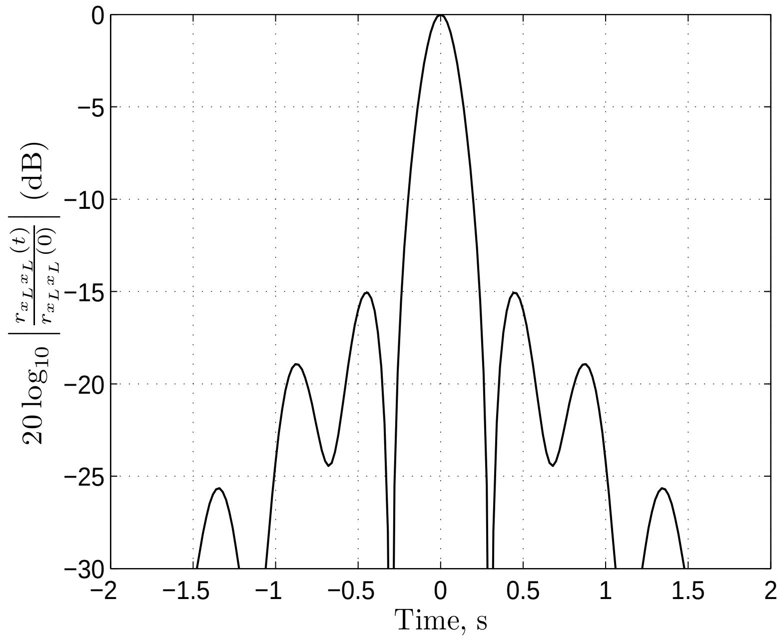

Figure 4-10: Autocorrelation Function for $x_L(t)$.

Accordingly, to reduce the side-lobes of the Lorenz waveform the parameters of the Lorenz system need to be set such that a trajectory is equally likely to jump to the next wing as remaining on the same wing of the attractor. To quantify this likelihood, a quantity called the transition rate, $r_t$, is defined in Eq. 4.3. The variable $n_t$ represents the number of times a trajectory rotates around one wing, then jumps to the next wing, and then rotates around that wing. The variable $n_s$ represents the number of times a trajectory completes a rotation around one wing and then proceeds to rotate again around the same wing of the attractor.

$$r_t = \frac{n_t}{n_t + n_s} \tag{4.3}$$

Equation 4.3 calculates the transition rate of one particular time-windowed solution to the Lorenz system. However, the transition rate of the Lorenz system with a particular set of parameters is defined to be equal to the mean transition rate of multiple time-windowed solutions of the system. As stated above, low side-lobes require for this transition rate to equal 0.5, and the combinations of $\sigma$ and $r$ that give rise to this transition rate is explored next.

A numerical simulation is used to explore how the parameters of the Lorenz system affect the transition rate of the system. To begin, $b$ is set to 100, and $\sigma$ and $r$ are varied such that $\sigma \in (200, 850)$ and $r \in (r_c, 1.6r_c)$. For each combination of $\sigma$ and $r$, the Lorenz system was numerically integrated over one hundred seconds to give rise to $x_L(t)$. The mean transition rate over three trials was then recorded. Figure 4-11 shows a mapping of the transition rate for varying values of $\sigma$ and $r$. As can be seen in the figure, for a constant $r$, increasing $\sigma$ will decrease the transition rate until around $\sigma = 500$. Then, increasing $\sigma$ will increase the transition rate. For a constant $\sigma$, increasing $r$ will, in most cases, increase the transition rate, although the rate of increase depends on the value of $\sigma$. The darkest region of the plot approximates where the parameters give rise to Lorenz systems with a transition rate equal to 0.5. When Fig. 4-11 is compared with Fig. 4-7, the low side-lobe region and the region where the transition rate equals 0.5 overlap. Thus, to operate with a low peak side-lobe, $\sigma$ and $r$ need to be chosen to give rise to a Lorenz system with a transition rate equal to 0.5, which is the darkest region of Fig. 4-11.

To further illustrate this final point, the side-lobes of two systems with different parameters and different transition rates are compared. The first set of parameters is $\{\sigma = 262, r = r_c, b = 100\}$, which gives rise to a system with a transition rate of about 0.5. The second system has a parameter set of $\{\sigma = 262, r = 1.6r_c, b = 100\}$, which gives rise to a transition rate of about 0.6. Figure 4-12 plots the autocorrelation

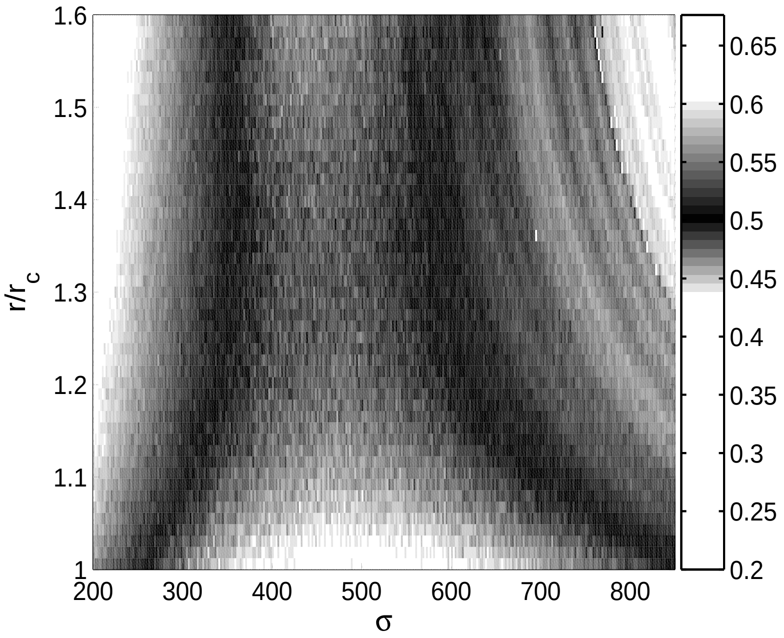

Figure 4-11: Transition Rate of the Lorenz System for $b = 100$ and Varying $\sigma$ and r. This figure was generated from a Lorenz system with $b = 100$ and varying values of $\sigma$ and $b$. For a particular value of $\sigma$ and $r$, the system was numerically integrated three times for distinct initial conditions with a step size of $10^{-3}$ seconds. The transition rate was calculated for each of the three solutions and then averaged together.

function of the Lorenz waveform, $x_L(t)$, derived from the two Lorenz systems. As can be seen in the figure, the autocorrelation function from the system with a transition rate of 0.50 has considerably lower side-lobes than the autocorrelation function from the system with a transition rate of 0.60.

By using Fig. 4-7 and Fig. 4-2, information from Sections 4.1 and 4.2 can be combined. Specifically, the values of $\sigma$ and $r$ can be chosen to trade off the peak-to-RMS ratio with the peak side-lobe level for $b = 100$. Specifically, the relevant information in Figs. 4-11 and 4-2 can be fused to form the design curves for $x_L(t)$. These design curves are shown in Fig. 4-13. The blue line, $C_1$, represents the combinations of $\sigma$ and $r$ that give rise to systems with transition rates equal to 0.5. Consequently, $C_1$ also marks the combinations of parameters with autocorrelation functions possessing

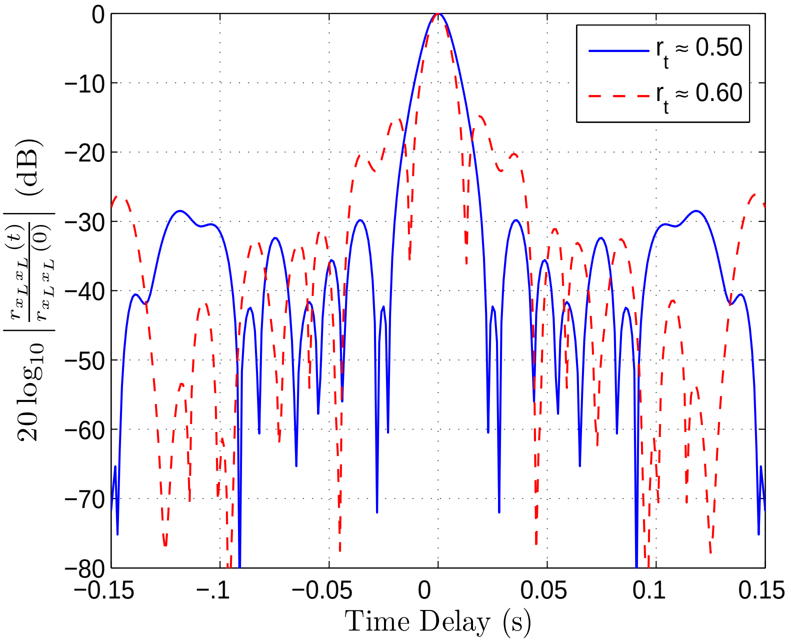

Figure 4-12: Side-lobe Comparison for Two Systems with Different Transition Rates. The autocorrelation functions in this figure are derived from two separate Lorenz systems. The system in blue has a transition rate of approximately 0.5, and the system in red has a transition rate of approximately 0.6.

minimized side-lobes. The red lines represent combinations of $\sigma$ and $r$ that give rise to systems with a peak-to-RMS ratio equal to 2.2, 2.3, and 2.4, respectively. Moreover, as shown in Fig. 4-1, the peak-to-RMS ratio in Fig. 4-13 monotonically increases from the bottom left corner to the top right corner. In this thesis, combinations of $\sigma$ and $r$ will be chosen on $C_1$ in order to minimize the magnitude of the peak side-lobe and reduce the peak-to-RMS ratio of $x_L(t)$ to less than 2.3. These combinations of parameters are illustrated in the figure as the operating region, which is shaded light blue[4]. Finally, the third section of this chapter explains how $b$ can be used to time scale $x_L(t)$.

---

[4] All lines in Fig. 4-13 are drawn with a relatively large width to indicate that the combinations of $\sigma$ and $r$ that give rise to minimized side-lobes and particular realizations of the peak-to-RMS ratio were numerically approximated (as opposed to analytically determined).

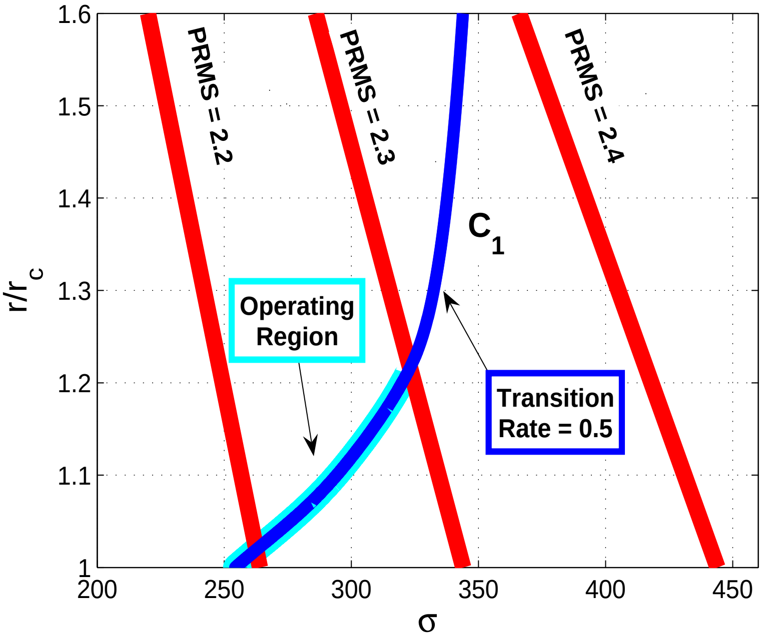

Figure 4-13: Lorenz Waveform Design Curves. For $b_0 = 100$, these curves indicate combinations of $\sigma_0$ and $r_0$ that tradeoff the peak-to-RMS ratio and magnitude of the peak side-lobe.

## 4.3 Energy Spectrum

A third radar design consideration deals with metrics associated with the energy spectrum of the Lorenz waveform. The metric isolated for this design consideration was the peak out-of-band side-lobe. However, the energy spectrum of all the waveforms presented in this thesis will have a energy spectrum qualitatively shaped as shown in Fig. 4-6 where the only major observable difference is in bandwidth. Thus, a search for the set of parameters that give rise to a minimal peak out-of-band side-lobe will yield limited results. However, the bandwidth of $x_L(t)$, although not directly a radar waveform metric, is very important to understand in order to meet the specifications for a given application. Moreover, the bandwidth is indirectly related to other radar waveform metrics such as the main-lobe width of the autocorrelation function. Thus, the objective of this section is to explain how to set the bandwidth of the system. Bandwidth control is discussed utilizing two separate approaches. Mathematically time scaling the Lorenz equations can be used to control the bandwidth of the state variables. Also scaling the Lorenz parameters can be used to time and amplitude scale the state variables. At first glance, scaling the parameters to set the bandwidth may seem unnecessary. However, in doing so, tremendous insight into the Lorenz system (and chaotic systems in general) is gained, and this insight is discussed in detail in Section 4.3.3.

### 4.3.1 Time-Scaling the Lorenz Equations

Before discussing issues related to time scaling the state variables the Lorenz system, some notation is introduced. The variable $\underline{\mathrm{x}}$(t) is defined as shown in Eq. 4.4 where $x$, $y$, and $z$ denote the state variable of the Lorenz system:

$$\underline{x}(t) = \begin{pmatrix} x(t) \\ y(t) \\ z(t) \end{pmatrix} \tag{4.4}$$

Next, the f(($\underline{\mathrm{x}}$t)) is defined as:

$$f(\underline{x}(t)) = \begin{pmatrix} \sigma(y(t) - x(t)) \\ rx(t) - y(t) - x(t)z(t) \\ x(t)y(t) - bz(t) \end{pmatrix} \tag{4.5}$$

Therefore, the Lorenz system can be written as shown in Eq. 4.6.

$$\dot{\underline{x}}(t) = f(\underline{x}(t)) \tag{4.6}$$

Also for notational convenience, $\underline{\mathrm{x}}$ and f($\underline{\mathrm{x}}$) can be defined by dropping the t-dependence as shown below. The t-dependencies will be dropped from this point forward unless otherwise stated.

$$\underline{x} = \begin{pmatrix} x \\ y \\ z \end{pmatrix} \tag{4.7}$$

$$f(\underline{x}) = \begin{pmatrix} \sigma(y-x) \\ rx - y - xz \\ xy - bz \end{pmatrix} \tag{4.8}$$

Using this notation, let $\underline{x}(t)$ denote the solution to Eq. 4.9. Also let $\underline{\tilde{x}}(t)$ denote the solution to Eq. 4.10 where $a$ is a constant greater than zero.

$$\dot{\underline{x}} = f(\underline{x}) \tag{4.9}$$

$$\dot{\underline{\tilde{x}}} = af(\underline{\tilde{x}}) \tag{4.10}$$

If both systems have identical initial conditions, then $\underline{\tilde{x}}(t)$ and $\underline{x}(t)$ are related as described in Eq. 4.11.

$$\underline{\tilde{x}}(t) = \underline{x}(at) \tag{4.11}$$

In other words, scaling the Lorenz equations by $a$ (as shown in Eq. 4.10) has the effect of time-scaling $\underline{\mathrm{x}}(\mathrm{t})$ by $a$.

Before proceeding, an important issue about numerically generating $\underline{\tilde{x}}(t)$ and $\underline{x}(t)$ is briefly discussed. Even though the above presentation is exact, due to rounding in the numerical integration methods and to the divergence of nearby Lorenz trajectories, numerically demonstrating the relationship in Eq. 4.11 is difficult if the magnitude of $a$ is too large. However, in this case, verifying the relation analytically is possible.

The time scaling principle can be proved by differentiating Eq. 4.11 by $t$ to determine the differential equations that describe $\underline{x}(at)$. First, let $\underline{x}(at)$ be denoted as $\underline{x}(\tau)$ where $\tau = at$. Next, $\underline{x}(\tau)$ is differentiated with the chain rule as shown below.

$$\begin{aligned}
\dot{\tilde{\underline{x}}} &= \frac{d}{dt}\underline{x}(\tau) \\
&= \frac{d[\underline{x}(\tau)]}{d\tau}\frac{d[\tau]}{dt} \\
&= \frac{d[\underline{x}(\tau)]}{d\tau}a \\
&= af(\underline{x}(\tau))
\end{aligned}$$

The last line in the above derivation follows from Eq. 4.6. The $\tau$ dependence can be dropped to yield the differential equations in Eq. 4.12 that describe $\tilde{x}(t) = \underline{x}(at)$.

$$\dot{\tilde{\underline{x}}} = af(\underline{x}) \tag{4.12}$$

Therefore, time scaling the Lorenz equations by $a$ will time-scale the state variables as described in Eqs. 4.9-4.11.

Scaling $\underline{x}(t)$ by $a$ in time also scales the bandwidth of $x(t)$ by $a$. The Fourier relationship in Eq. 4.13 describes how this time scaling affects the bandwidth of $\underline{x}(at)$ (where $X(j\omega)$ is the Fourier transform of x(t)).

$$x(at) \longleftrightarrow \frac{1}{|a|}X\left(\frac{j\omega}{a}\right) \tag{4.13}$$

Thus as $a$ increases, the bandwidth of the $\underline{x}(at)$ likewise increases by a factor of $a$.

By scaling the Lorenz equations, a Lorenz radar waveform can be generated with the desired properties and bandwidth. To do so, first $\sigma$, $r$, and $b$ in Eq. 4.14 must be chosen such that the Lorenz system has the desired system properties.

$$\dot{\underline{x}} = a\begin{pmatrix} \sigma(y-x) \\ rx - y - xz \\ xy - bz \end{pmatrix} \tag{4.14}$$

As explained above, the bandwidth of $x(at)$ can then be scaled by varying $a$ in Eq. 4.14. Finally, the length of the waveform in time is selected by numerically integrating

Eq. 4.14 over the desired time interval. The result is Lorenz radar waveform with the desired system properties (determined by setting the Lorenz parameters), desired bandwidth, and the desired length in time.

### 4.3.2 Time and Amplitude Scaling the Lorenz Equations

Scaling the Lorenz parameters is, in fact, very close to a time and amplitude scaling of the Lorenz system. Consequently, before presenting how scaling the Lorenz parameters approximately scales $\underline{x}(t)$ in time and amplitude, the differential equations that describe an exact time and amplitude scaling are presented. Let $\underline{x}(t)$ denote the solution to the Lorenz equations given in Eq. 4.15 where$f$ denotes the Lorenz system as defined in Eq. 4.8. Also, let $\underline{\tilde{x}}(t)$ denote the solution to Eq. 4.16 where $a > 0$.

$$\dot{\underline{x}} \quad = \quad f(\underline{x}) \tag{4.15}$$

$$\dot{\underline{\tilde{x}}} \quad = \quad a^2 f(\frac{1}{a}\underline{\tilde{x}}) \tag{4.16}$$

If the initial conditions of $\underline{x}(t)$ and $\underline{\tilde{x}}(t)$ are selected appropriately, then the two sets of state variables are related according to Eq. 4.17.

$$\underline{\tilde{x}}(t) \quad = \quad a\underline{x}(at) \tag{4.17}$$

Appropriately selecting the initial conditions means that the initial conditions are related as shown in Eq. 4.18.

$$\{\tilde{x}_0, \tilde{y}_0, \tilde{z}_0\} = \{ax_0, ay_0, az_0\} \tag{4.18}$$

Thus, Eqs. 4.15-4.17 present an exact time and amplitude scaling of the Lorenz equations.

This time and amplitude scaling by $a$ can again be proved by differentiating $a\underline{x}(at)$ by $t$ to determine the differential equations that describe $a\underline{x}(at)$. First, let $\underline{x}(t)$ be a solution to the Lorenz system. Next, let $a\underline{x}(at)$ be denoted by $\tilde{\underline{x}}(t)$ as shown in Eq. 4.19.

$$\tilde{\underline{x}}(t) \quad = \quad a\underline{x}(at) \tag{4.19}$$

Differentiating both sides of Eq. 4.19 gives rise to Eq. 4.20 where $\tau$ is substituted for $at$.

$$\begin{aligned} \dot{\tilde{\underline{x}}}(t) &= a\frac{d}{dt}\underline{x}(\tau) \\ &= a\frac{d[\underline{x}(\tau)]}{d\tau}\frac{d[\tau]}{dt} \\ &= a^2\frac{d[\underline{x}(\tau)]}{d\tau} \\ &= a^2 f(\underline{x}(\tau)) \end{aligned} \tag{4.20}$$

The last line in the above derivation follows from Eq. 4.6. Substituting $at$ back in for $\tau$ gives rise to Eq. 4.21.

$$\dot{\tilde{\underline{x}}}(t) \quad = \quad a^2 f(\underline{x}(at)) \tag{4.21}$$

By using Eq. 4.19, $\frac{1}{a}\tilde{\underline{x}}(t)$ can be substituted for $\underline{x}(at)$ on the right hand side of Eq. 4.21. By dropping the t-dependencies, this substitution yields Eq. 4.22, which is equivalent to Eq. 4.16.

$$\dot{\tilde{\underline{x}}} \quad = \quad a^2 f(\frac{1}{a}\tilde{\underline{x}}) \tag{4.22}$$

Therefore, the differential equations that exactly describe $\underline{x}(t)$ and $a\underline{x}(at)$ are given in Eqs. 4.15 and 4.16 where $f$ denotes the Lorenz system as given in Eq. 4.8.

### 4.3.3 Approximate Time-Scaling via the Lorenz Parameters

Numerical observations clearly demonstrate that the bandwidth of a Lorenz waveform significantly varies depending on the Lorenz parameters used. For example, Figure

4-14 shows the typical energy spectra for two waveforms, $x_{L1}(t)$ and $x_{L2}(t)$, which are generated from two systems with different parameters. The gray plot corresponds to the spectrum associated with the parameters $\{\sigma = 8.05, r = 39.72, b = 4.00\}$, which will be called System 1. The black plot corresponds to a spectrum associated with $\{\sigma = 22.95, r = 69.04, b = 10.00\}$, which will be called System 2. The variable $x_{L1}(t)$ is derived from System 1, and $x_{L2}(t)$ is derived from System 2. The bandwidth of $x_{L1}(t)$ is approximately 9.40 Hz, and the bandwidth of $x_{L2}(t)$ is approximately 20.74 Hz (where the bandwidth is as defined in Chapter 3). The bandwidth of $x_{L2}(t)$ is roughly a factor of 2.2 times greater than the bandwidth of the $x_{L1}(t)$. This result can be verified by repeating the calculations with new Lorenz waveforms from System 1 and 2 to reveal that the bandwidth of waveforms from System 2 is about 2.2 times the bandwidth of waveforms from System 1.

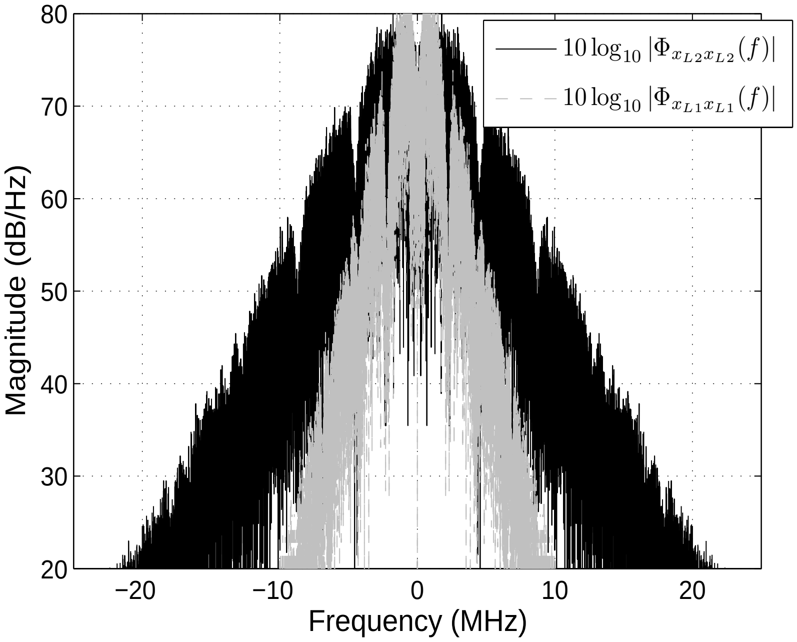

Figure 4-14: Energy Spectrum of Two Lorenz Systems with Different Parameter Values.

As shown above, varying the parameters of the Lorenz system has a significant impact on the bandwidth of a Lorenz waveform, which is a normalized and time-windowed segment of the state variable $x(t)$. Thus, based on this numerical observation, appropriately selecting the Lorenz parameters was hypothesized to time and amplitude scale the state variables of the Lorenz system, since time and amplitude scaling by a particular factor corresponds to scaling the bandwidth by the same factor[5]. Consequently, a method for determining this hypothetical scaling needs to be determined.

First, a mathematical description of a time and amplitude scaling, via varying the parameters, is given. Let two Lorenz system with different Lorenz parameters be denoted as $\underline{x}(t)$ and $\hat{\underline{x}}(t)$, respectively. Let $\underline{x}(t)$ and $\hat{\underline{x}}(t)$ be described by Eqs. 4.23 and 4.24, respectively.

$$\dot{\underline{x}} = \begin{pmatrix} \sigma_0(y-x) \\ r_0 x - y - xz \\ xy - b_0 z \end{pmatrix} \tag{4.23}$$

$$\dot{\hat{\underline{x}}} = \begin{pmatrix} \hat{\sigma}(\hat{y}-\hat{x}) \\ \hat{r}\hat{x} - \hat{y} - \hat{x}\hat{z} \\ \hat{x}\hat{y} - \hat{b}\hat{z} \end{pmatrix} \tag{4.24}$$

If the parameters and initial conditions of $\hat{\underline{x}}(t)$ and $\underline{x}(t)$ are related according to Eqs. 4.25 and 4.26, $\underline{x}(t)$ and $\hat{\underline{x}}(t)$ will be related as shown in Eq. 4.27. However, there exists two practical constraints in order for Eq. 4.27 to hold, which are given in Eq. 4.28.

$$\{\hat{\sigma}, \hat{r}, \hat{b}\} = \{a\sigma_0, ar_0, ab_0\} \tag{4.25}$$

$$\{\hat{x}_0, \hat{y}_0, \hat{z}_0\} = \{ax_0, ay_0, az_0\} \tag{4.26}$$

$$\hat{\underline{x}}(t) \approx a\underline{x}(at) \tag{4.27}$$

---

[5] This is due to the Fourier relationship where the Fourier transform of $x(at)$ is $\frac{1}{|a|}X(\frac{j\omega}{a})$.

$$\begin{aligned} r_0 &\geq 360 \\ a &\in [0.4, \infty) \end{aligned} \tag{4.28}$$

To understand both why Eq. 4.27 holds and the practical constraints, $\hat{\underline{x}}(t)$ is compared with a system that exactly time and amplitude scales $\underline{x}(t)$. Let $\tilde{\underline{x}}(t)$ denote a system that time and amplitude scales $\underline{x}(t)$ exactly, i.e. $\tilde{\underline{x}}(t) = a\underline{x}(at)$. The system that describes $\tilde{\underline{x}}(t)$ was derived in the previous section and was given in Eq. 4.16. By substituting the Lorenz system for $f$ using Eq. 4.5, Eq. 4.16 can be re-written as Eq. 4.29.

$$\dot{\tilde{\underline{x}}} = \begin{pmatrix} a\sigma_0(\tilde{y} - \tilde{x}) \\ ar_0\tilde{x} - a\tilde{y} - \tilde{x}\tilde{z} \\ \tilde{x}\tilde{y} - ab_0\tilde{z} \end{pmatrix} \tag{4.29}$$

This system has the same parameter set as $\underline{x}(t)$, which is $\{\sigma_0, r_0, b_0\}$ and also time and amplitude scales $\underline{x}(t)$ by $a$.

By comparing Eq. 4.24 and 4.29, it is easy to see why $\hat{\underline{x}}(t)$ cannot be exactly equal to $\tilde{x}(t) = a\underline{x}(at)$. If $\hat{\underline{x}}(t)$ equals $\tilde{x}(t) = a\underline{x}(at)$, then Eqs. 4.29 and 4.24 must be equivalent, since $\dot{\hat{\underline{x}}}(t) = \dot{\tilde{x}}(t)$ imposes the following constraints on the parameters of $\hat{\underline{x}}(t)$:

$$\hat{\sigma} = a\sigma_0 \tag{4.30}$$

$$\hat{r}\hat{x} - \hat{y} = ar_0\tilde{x} - a\tilde{y} \tag{4.31}$$

$$\hat{b} = ab_0. \tag{4.32}$$

These constraints are determined by equating Eqs. 4.29 and 4.24. Furthermore, if $\hat{\underline{x}}(t) = \tilde{\underline{x}}(t) = a\underline{x}(at)$, then $a\underline{x}(at)$ can be substituted into Eq. 4.31 to give rise to Eq. 4.33 as long as $x \neq 0$.

$$\hat{r} = ar_0 - \frac{y}{x}(a - 1) \tag{4.33}$$

Since in general $y \neq x$ and $\frac{y}{x}$ is time-varying, the preceding equation implies that $\hat{r}$ is time-varying, which is impossible due to the definition of a parameter. Consequently, $\hat{\underline{x}}(t) \neq \tilde{\underline{x}}(t) = a\underline{x}(at)$, or the constraint in Eq. 4.33 would hold.

As shown in the previous paragraph, the Lorenz system cannot be exactly time and amplitude scaled by simply varying the parameters. However, with the imposition of the constraint that $ar_0 >> \frac{y(t)}{x(t)}(a-1)$, setting $\hat{\sigma} = a\sigma_0$, $\hat{r} = ar_0$, and $\hat{b} = ab_0$ approximately corresponds to time and amplitude scaling the Lorenz system, since Eq. 4.33 is almost satisfied (i.e. $\hat{r} = ar_0 \approx ar_0 - \frac{y}{x}(a-1)$). This constraint can be written as shown in Eq. 4.34.

$$1 >> \frac{y(t)}{r_0 x(t)}(1 - \frac{1}{a}) \tag{4.34}$$

When the inequality in 4.34 holds, then scaling the Lorenz parameters by $a$ approximately corresponds to a time and amplitude scaling.

In order to compare the constraint in Eq. 4.34 for various values of $a$ and $r_0$, Eq. 4.34 is simplified to eliminate the time-dependence due to $\frac{y(t)}{x(t)}$. This simplification is made by substituting $\frac{y(t)}{x(t)}$ with the standard deviation of $\frac{y(t)}{x(t)}$. The resulting constraint is given in Eq. 4.35 where $\sigma_{yx}$ is the standard deviation of $\frac{y(t)}{x(t)}$.

$$1 >> \frac{\sigma_{yx}}{r_0}(1 - \frac{1}{a}) \equiv C(a) \tag{4.35}$$

Since the mean of $\frac{y(t)}{x(t)}$ is roughly zero, for most time, $\frac{y(t)}{x(t)}$ lies within $\pm\sigma_{yx}$. Figure 4-15 plots $C(a)$ as a function of the scale factor, $a$, for various values of $r_0$.

Operating at low values of $C(a)$ is necessary if an approximate time and amplitude scaling is desired (i.e. $\hat{\underline{x}}(t) \approx a\underline{x}(at)$). As can be seen in in Eq. 4.35, if $a$ is approximately unity, then $C(a)$ will be small no matter the value of $r_0$. However, in this thesis, in order to operate over a large range of $a$, $a \in [0.4, \infty)$, the constraint of $r_0 \geq 360$ is enforced so that $C(a)$ remains less than 0.1 for all $a \in [0.4, \infty)$ as shown in Fig. 4-15[6]. Enforcing $C(a) < 0.1$ implies that, for most time, $ar_0 - \frac{y}{x}(a-1)$ is within 10% of $\hat{r} = ar_0$. Thus, scaling the parameters approximately time and amplitude scales the Lorenz system since Eq. 4.33 is almost satisfied.

To illustrate and verify a time and amplitude scaling via scaling the Lorenz pa-

---

[6] Some applications may require a stricter constraint on $r_0$. However, in this thesis, scaling the parameters is only used for setting the bandwidth, so the constraint on $r_0$ is sufficient.

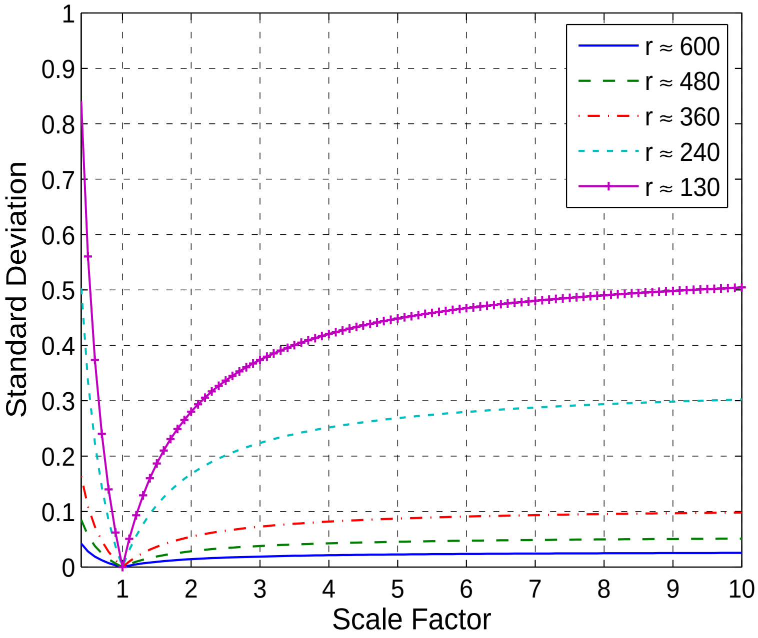

Figure 4-15: Estimation of Constraint Validity. This figure plots $C(a)$, which attempts to quantify how close scaling the parameter set by $a$ is to an exact time-scaling and re-normalization of the original Lorenz system. Low values of $C(a)$ correspond to a more accurate approximation of a time-scaling and re-normalization. Multiple plots are shown. Each plot is with a different parameter set with the value of $r$ was given in the legend. The value of $b$ and $\sigma$ were chosen so that the system had a transition rate equal to 0.5 and so that it was operating at the onset of chaos.

rameters, two Lorenz systems with scaled parameters are numerically integrated and compared. The first system has a set of parameters $\{\sigma, r, b\}$ equal to $\{267, 595, 100\}$. A set of initial conditions were found on the attractor of this Lorenz system and were used to give rise to the $x$ state variable which is plotted in a solid blue line in Fig. 4-16. The parameters and the initial conditions of the second system were chosen according to Eqs. 4.25 and 4.26, respectively, where $a = 0.95$. The $x$ state variable of the second system is plotted in a dashed red line in Fig. 4-16. As predicted by the analysis, it is expected for the the red signal to be time-scaled by 0.95 and amplitude-scaled by 0.95. Both of these expectations appear to be true. Although only $x(t)$ is shown, $y(t)$ and $z(t)$ are also time and amplitude scaled.

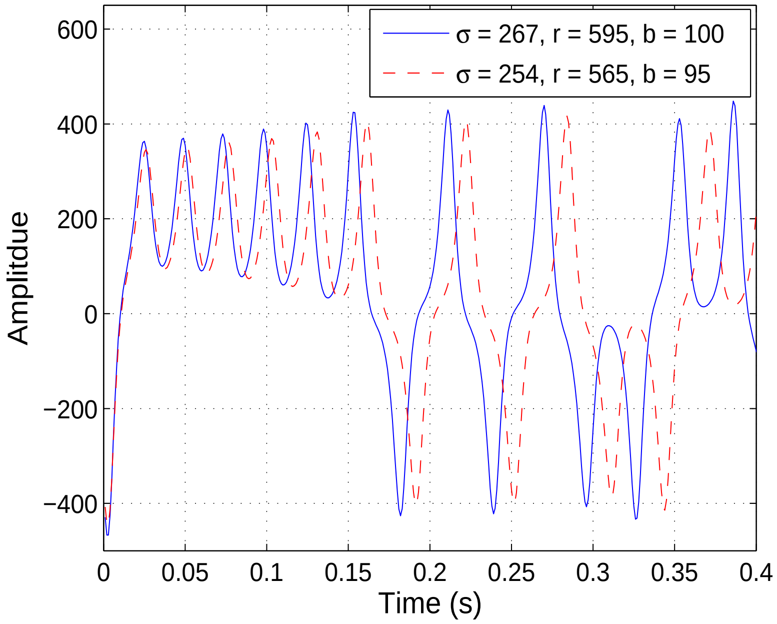

Figure 4-16: Time Evolution of the $x$ State-Variable for Two Lorenz Systems. The two systems have different parameter sets that give rise to two Lorenz systems where one system is a time-scaled and re-normalized version of the other system. The time-scaling and re-normalization factor was 0.95.

Section 4.3.1 explains that even when two Lorenz systems are exact time-scalings of each other, the solutions of the two respective systems only initially trace out the same path on the attractor when numerically generated on a computer. Unfortunately, due to both rounding errors and the fact that nearby trajectories diverge exponentially, the two trajectories will eventually diverge. Consequently, an approximate time-scaled version of the Lorenz system should, not be expected to exactly trace out the trajectory of the original solution (although it performs reasonably well when compared to the exact time-scaled version of the original system for certain values of the Lorenz parameters).

As mentioned at the beginning of this section, insights into the Lorenz system can be gained by using the parameters to time scale the state variables of the Lorenz system. The remainder of this section is devoted to two such insights. First, as shown in this section, the Lorenz equations cannot be *exactly* time and amplitude scaled because of the underlying structure of the Lorenz equations. However, an exact time and amplitude scaling *is* attainable by changing the Lorenz system to a different chaotic system with a similar structure. The second insight reveals how Lorenz parameters that scale with the bandwidth will approximately decouple the issues of setting the bandwidth and setting other system properties.

First, to determine how the structure of the Lorenz system should be modified, the Lorenz system in Eq. 4.36 is compared with the two systems given in Eqs. 4.37 and 4.38. Equation 4.37 (which was derived in Section 4.3.2) describes a system that exactly time and amplitude scales the Lorenz system in Eq. 4.36 by $a$. Equation 4.38 is just a Lorenz system with a set of parameters equal to $\{\sigma, r, b\}$.

$$\dot{\underline{x}} = \begin{pmatrix} \sigma_0(y-x) \\ r_0 x - y - xz \\ xy - b_0 z \end{pmatrix} \tag{4.36}$$

$$\dot{\underline{\tilde{x}}} = \begin{pmatrix} a\sigma_0(\tilde{y}-\tilde{x}) \\ ar_0\tilde{x} - a\tilde{y} - \tilde{x}\tilde{z} \\ \tilde{x}\tilde{y} - ab_0\tilde{z} \end{pmatrix} \tag{4.37}$$

$$\dot{\underline{x}} = \begin{pmatrix} \sigma(y-x) \\ rx - y - xz \\ xy - bz \end{pmatrix} \tag{4.38}$$

As explained in this section, there is no set of Lorenz parameters for Eq. 4.38 that can exactly time and amplitude scale Eq. 4.36 by a factor of $a$. In other words, there is no way to determine a set of Lorenz parameters so that the Lorenz system in Eq. 4.38 bears the form of Eq. 4.37. For example, if the parameters for the Lorenz system in Eq. 4.38 are chosen to be $\{\sigma, r, b\} = \{a\sigma_0, ar_0, ab_0\}$, then the resulting system, shown in Eq. 4.39, is close to Eq. 4.37, but not equivalent.

$$\underline{\dot{x}} = \begin{pmatrix} a\sigma_0(y-x) \\ ar_0x - y - xz \\ xy - ab_0z \end{pmatrix} \tag{4.39}$$

Specifically, the $-y$ term of the Eq. 4.39 does not match the $-a\tilde{y}$ term of Eq. 4.37.

However, if the Lorenz equations are changed, then the parameters could be chosen to account for an exact time and amplitude scaling by $a$. For example, if a system is defined as shown in Eq. 4.40, then a system that exactly time and amplitude scales Eq. 4.40 by $a$ would be described as shown in Eq. 4.41.

$$\underline{\dot{x}} = \begin{pmatrix} \sigma(y-x) \\ rx - \sigma y - xz \\ xy - bz \end{pmatrix} \tag{4.40}$$

$$\underline{\dot{\tilde{x}}} = \begin{pmatrix} a\sigma_0(\tilde{y}-\tilde{x}) \\ ar_0\tilde{x} - a\sigma_0\tilde{y} - \tilde{x}\tilde{z} \\ \tilde{x}\tilde{y} - ab_0\tilde{z} \end{pmatrix} \tag{4.41}$$

As can be seen by comparing Eqs. 4.40 and 4.41, scaling the parameters by $a$ is equivalent to time and amplitude scaling the system by $a$. Although a $\sigma$ was placed in the $-y$ term of the Lorenz system, either $r$ or $b$ could also be used. Moreover, placing one of the state variables[7], $x$, $y$, or $z$, in front of the $-y$ term would also enable scaling the parameters to correspond exactly to a time and amplitude scaling of the original system[8].

Lastly, the case is considered where the $-y$ term in the Lorenz equation has been omitted altogether. This system is given below in Eq. 4.42. For this system, the onset of chaos occurs at $r > \frac{\sigma(\sigma+b)}{(\sigma-b)}$. The attractor for this system is also butterfly-shaped

---

[7] The author would like to thank Charles Rohrs for suggesting that a state variable could also be placed in front of the $-y$ term to give a system that exactly time and amplitude scales with $a$.

[8] The dynamics of these systems are yet to be explored.

and appears to be very similar to the attractor of the Lorenz system.

$$\underline{x} = \begin{pmatrix} \sigma(y - x) \\ rx - xz \\ xy - bz \end{pmatrix} \tag{4.42}$$

If the parameters are given such that $\{\sigma, r, b\} = \{a\sigma_0, ar_0, ab_0\}$, then Eq. 4.42 can be written as in Eq. 4.43, and $a$ controls a time and amplitude scaling of a system with the parameters, $\sigma_0$, $r_0$, and $b_0$.

$$\underline{x} = \begin{pmatrix} a\sigma_0(y - x) \\ ar_0x - xz \\ xy - ab_0z \end{pmatrix} \tag{4.43}$$

Additionally, for large parameter values, the dynamics of the Lorenz system such as the one shown in Eq. 4.38 actually become very similar to the dynamics of the system described by Eq. 4.42. For the Lorenz system, when scaling the parameters by $a$, $\sigma = a\sigma_0$, $b = ab_0$, and $r = ar_0$, the amplitude of the state variables increases by about a factor of $a$, due to the approximate amplitude scaling. When scaling the parameters by $a$, all the terms in the Lorenz equations in Eq. 4.38 increase by a factor on the order of $a^2$ except the $-y$ term in the second line. This term only increases on the order of $a$. Thus as $a$ increases, the significance of the $-y$ term in the Lorenz system decreases, makes the dynamics very similar to Eq. 4.42 where the $-y$ term has been omitted.

A second insight into Lorenz system, due to Lorenz parameters that scale with bandwidth[9], involves decoupling the parameters that set the bandwidth and those that set other system properties. Specifically if the parameters are selected according to Eq. 4.44, $\sigma_0$ and $r_0$ can be used to select other system properties for a constant $b_0$

---

[9] Again and as explained earlier, time-scaling by $a$ corresponds to scaling the bandwidth by $a$.

(which in this thesis will be 100), and $a$ can be used to scale the bandwidth.

$$\{\sigma, r, b\} = \{a\sigma_0, ar_0, 100a\} \tag{4.44}$$

Since $a$ has a known effect on the system, the other parameters can be used to search for system properties over two dimensions, $\sigma_0$ and $r_0$, instead of three (such as was done for the minimum peak side-lobe and lowest peak-to-RMS in Figs. 4-7 and 4-1).

To understand why the bandwidth and other system properties decouple, the scaled Lorenz parameters in Eq. 4.44 are written as shown in Eq. 4.45 where $b_0$ is set to a constant at 100.

$$\begin{bmatrix} \sigma \\ r \\ b \end{bmatrix} = \begin{bmatrix} 1 \\ 0 \\ 0 \end{bmatrix} a\sigma_0 + \begin{bmatrix} 0 \\ 1 \\ 0 \end{bmatrix} ar_0 + \begin{bmatrix} 0 \\ 0 \\ 100 \end{bmatrix} a \tag{4.45}$$

Next, if we let $\tilde{\sigma_0} = a\sigma_0$ and $\tilde{r_0} = ar_0$, then Eq. 4.45 can be re-written as shown in Eq. 4.46 where $a \in (0, \infty)$, $\tilde{\sigma_0} \in (0, \infty)$ and $\tilde{r_0} \in (0, \infty)$ and the three parameters can be selected independently.

$$\begin{bmatrix} \sigma \\ r \\ b \end{bmatrix} = \begin{bmatrix} 1 \\ 0 \\ 0 \end{bmatrix} \tilde{\sigma_0} + \begin{bmatrix} 0 \\ 1 \\ 0 \end{bmatrix} \tilde{r_0} + \begin{bmatrix} 0 \\ 0 \\ 100 \end{bmatrix} a \tag{4.46}$$

Consequently, all positive combinations of $\sigma$, $r$, and $b$ are reachable by appropriately varying $\tilde{\sigma}_0$, $\tilde{r}_0$, and $a$. Moreover, all positive combinations of $\tilde{\sigma}_0$, $\tilde{r}_0$, and $a$ are reachable from $\sigma_0$, $r_0$, and $a$. Thus, the parameters $\sigma_0$ and $r_0$ in Eq. 4.45 can be selected when $a = 1$ and varying $a$ will determine the values of $\sigma$, $r$, and $b$. Selecting the parameters in this way gives rise to any positive combination of $\sigma$, $r$, and $b$; however, the interpretation that $a$ approximately time scales the dynamics is only valid if the constraints in Eq. 4.28 are satisfied. If satisfied, $\sigma_0$ and $r_0$ are selected to set desired system properties when $a = 1$, and then $a$ is varied to time and amplitude scale the particular dynamics of the system. Therefore, as long as Eq. 4.28 is satisfied, the parameters that set the bandwidth (i.e. $a$) have been decoupled from the parameters that set system properties unaffected by a time and amplitude scaling (i.e. $\sigma_0$ and $r_0$). These other system properties can be explored over two dimensions, $\sigma_0$ and $r_0$.

## 4.4 Cross-correlation Function

The objective of this thesis is to use chaos theory to generate sets of quasi-orthogonal waveforms. Thus, verifying the quasi-orthogonality of the Lorenz waveform, $x_L(t)$, is important. As explained in Chapter 3, two waveforms, $w_1(t)$ and $w_2(t)$, are only quasi-orthogonal if the average cross-correlation level is on the order of $20\log_{10}\left|\sqrt{LB}\right|$ dB below $r_{w_1w_1}(0)$ and $r_{w_2w_2}(0)$. Waveforms generated from the Lorenz system were observed to be quasi-orthogonal, which is a result of the aperiodicity of $x(t)$ and the sensitivity to initial conditions. As a result, every waveform generated with a set of distinct initial conditions was observed to be quasi-orthogonal with a waveform generated with a different set of initial conditions as long as the waveforms are not trivially short in time.

Thus, to verify that the Lorenz waveforms are quasi-orthogonal, two distinct Lorenz waveforms are generated and the cross-correlation function was determined. The parameters utilized for this Lorenz system were $\sigma = 441$, $r = 595$, and $b = 165$. A continuous time signal, $x_L(t)$ was approximated via numerical integration where the initial conditions are selected as explained in Chapter 2. The resulting bandwidth of $x(t)$ was 500 MHZ, and the length of $x_L(t)$ in time was 20 $\mu$s. Consequently, the time-bandwidth product for this waveform was calculated to be $-20\log_{10}\left|\sqrt{LB}\right| = -40$ dB. The cross-correlation of two 20 $\mu$s time-segments of $x_L(t)$ with randomly selected initial conditions is shown in Fig. 4-17. The average side-lobe level of the cross-correlation function in Fig. 4-17 was evaluated to -42.7 dB, which is less than -20 $\log_{10}\left|\sqrt{TB}\right|$ and implies that these Lorenz waveforms are indeed quasi-orthogonal. This example can be extended, without generality, to any set of arbitrary Lorenz parameters (that gives rise to chaotic dynamics) to conclude that waveforms generated from the Lorenz system are indeed quasi-orthogonal.

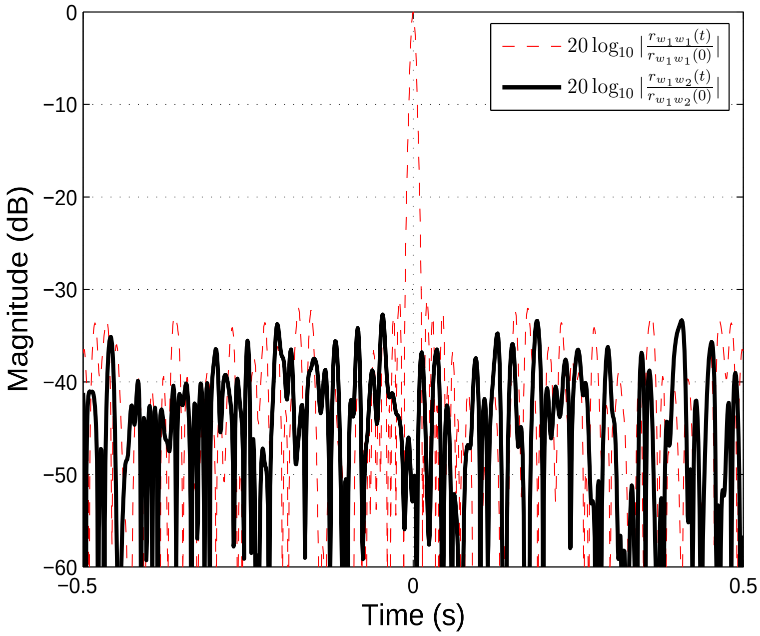

Figure 4-17: Cross-Correlation Between Two Distinct Lorenz Waveforms. The autocorrelation function is plotted behind the cross-correlation function to demonstrate that average cross-correlation function is $20\log_{10}\left(\sqrt{TB}\right) = 40$ dB below the peak of the autocorrelation function of one waveform.

## 4.5 Summary

The objective of this chapter was to determine a method for choosing the Lorenz parameters to generate Lorenz waveforms, $x_L(t)$, with the desired radar waveform metrics. As established in Sections 4.1 and 4.2, the two radar waveform metrics of $x_L(t)$ that can be controlled by $\sigma$ and $r$ are the magnitude of the peak side-lobe and the peak-to-RMS ratio. As explained in Section 4.3, if the parameters are selected via Eq. 4.44, then these radar metrics are completely determined by $\sigma_0$ and $r_0$ for a fixed $b_0 = 100$. Consequently, for $b_0 = 100$, $\sigma_0$ and $r_0$ can be appropriately selected in the operating region of the design curve shown in Fig. 4-13 (which trades-off peak side-lobe with peak-to-RMS ratio). Then as long as the constraints in Eq. 4.28 are satisfied, $a$ in Eq. 4.44 can be used to set the bandwidth as desired without affecting the side-lobes or peak-to-RMS ratio. In this thesis, this is the metho used for selecting the Lorenz parameters for the Lorenz waveform.

As well as providing a method for selecting the Lorenz parameters, this chapter discusses two additional key points. First, Section 4.4 verifies that waveforms generated from the Lorenz system are indeed quasi-orthogonal. Second, Section 4.3 explains how the state variables of the Lorenz system can be time-scaled in two ways: by scaling the Lorenz equations or by scaling the Lorenz parameters. Scaling the Lorenz equations exactly time scales the state variables of the Lorenz system. On the other hand, scaling the Lorenz parameters, only approximately time (and amplitude) scales the state variables. However, the development of time scaling the state variables via the Lorenz parameters provides two additional insights. The first of which is that the Lorenz system can be modified such that scaling parameters corresponds exactly to time and amplitude scaling the state variables. Several candidate systems are then suggested. The second insight reveals how the parameters being used to set the bandwidth can be decoupled from the parameters being used to set other system properties, which was used to develop a method for selecting the Lorenz parameters when generating Lorenz waveforms (as explained in the previous paragraph).

# Chapter 5

# Design Methods for Lorenz-Based Radar Waveforms

In this chapter, the set of Lorenz waveforms is evaluated and improvements are suggested. Specifically, the first section evaluates the Lorenz waveforms by comparing them with waveforms from a set of quasi-orthogonal radar waveforms used in practice at M.I.T. Lincoln Laboratory. These waveforms are generated from a method unrelated to deterministic chaos. For illustration purposes, the two sets of waveforms are compared by comparing two sample waveforms, one from each set, to illustrate the typical results. The Lorenz waveform will be referred to as $x_L(t)$, and the waveform being employed in practice will be referred to as $w(t)$. The two radar waveforms will be compared on all of the four radar waveform design considerations. Based on the comparison, the second section suggests improvements to the Lorenz waveforms. Then in the last section, the improved waveform is compared with $w(t)$ on all the radar waveform metrics.

| Description of System Specifications | |
|---|---|
| Bandwidth | $B \approx 500$ MHz |
| Pulse Length | $L = 20\mu s$ |
| Sampling Frequency | $\frac{1}{T} = 1.5GHz$ |

Table 5.1: System Specifications.

## 5.1 Evaluating the Lorenz Waveforms against Traditional Designs

In this section, the Lorenz waveforms will be compared with $w(t)$. Both waveforms are designed to be compatible with the specifications given in Table 5.1. As explained in Chapter 3, the initial conditions for the Lorenz waveforms were selected in a $800 \times 800 \times 800$ cube in state space, which is centered around the origin. The Lorenz system was numerically integrated to generate $4 \times 10^4$ samples using a fourth-order runga-kutta method and a step size of $10^{-3}$ seconds. The first $10^4$ samples allowed the trajectory enough time to converge to the chaotic attractor and were discarded. The $10^4 + 1$ sample was the $n = 0$ sample for the sequence of $3 \times 10^4$ samples, which is referred to as $x[n]$. For ease of implementation and without loss of generality, the sampling period of $x[n]$ is considered to be $\frac{2}{3}$ of a nanosecond as opposed to the integration step size of $10^{-3}$ seconds. Consequently the length in time of the resulting continuous-time signal, $x_L(t)$, is 20 $\mu s$ as required in Table 5.1. Also, the waveform is normalized so that its peak magnitude equals unity. Next, the parameters of the Lorenz system, $\{\sigma, r, b\}$, need to be selected to minimize side-lobes, to reduce peak-to-RMS ratio, and set the bandwidth of $x_L(t)$ to 500 MHz.

The Lorenz parameters were selected consistent with the discussion in the previous chapter. First, the parameters set of $\{\sigma \approx 267, r \approx 595, b \approx 100\}$ was used to give rise to a Lorenz system with the lowest peak-to-RMS ratio for a transition rate of 0.5. The bandwidth of waveforms from this system was then evaluated to be approximately 302 MHz. Since it was shown in Chapter 4 that scaling the parameter set approximately scales the bandwidth by the same factor, the parameters were scaled by 1.65, which yields $\{\sigma \approx 441, r \approx 982, b \approx 165\}$. The bandwidth of waveforms from this system was evaluated to be approximately 500 MHz as required by Table 5.1. In this chapter, a Lorenz waveform, $x_L(t)$, is generated from the Lorenz system given in Eq. 5.1.

$$\begin{aligned} \dot{x} &= 441(y-x) \\ \dot{y} &= 595x - y - xz \\ \dot{z} &= xy - 165z \end{aligned} \tag{5.1}$$

It is worth noting that each one of the Lorenz waveforms generated in this system can be represented by 6 finite-precision numbers. The first three numbers are the initial conditions of Lorenz system, $\{x_o, y_o, z_o\}$, and the set of three parameters, $\{\sigma, b, r\}$. Consequently, to store these radar waveforms, all that is needed is these six numbers or a method for selecting these six numbers.

### 5.1.1 Peak-to-RMS Ratio

The peak-to-RMS ratio (PRMS) is straightforward to evaluate for the Lorenz waveform. Using Eq. 3.17, the PRMS of the Lorenz waveform, $x_L(t)$, is 2.23. However, the PRMS of $w(t)$ is 1.21. Thus, the PRMS of $x_L(t)$ is significantly greater than the PRMS of $w(t)$. If the peaks of the two waveforms are normalized to unity, then the average power of $x_L(t)$ is a factor 0.3 times smaller than the average power of $w(t)$, which corresponds to about a 5 dB reduction in signal power. This reduction is unacceptable for many radar applications.

### 5.1.2 Autocorrelation Function

Comparing $x_L(t)$ and $w(t)$ on metrics associated with the autocorrelation function involves comparing the main-lobe width and the magnitude of the peak side-lobe of the two waveforms. To make this comparison, the autocorrelation function of $x_L(t)$ is shown in Fig. 5-1. The peak side-lobe has a magnitude that is -26 dB down from the magnitude of the main-lobe and is located in time at a delay of 1.3 $\mu$s away from the peak of the main-lobe. This peak is not visible in Fig. 5-1. For reference, the average side-lobe level was evaluated to be -42.8 dB, which is sufficient for many applications. The main-lobe width of the autocorrelation function was evaluated to be 4.2 ns, which, relatively speaking, is quite large as shown by comparing this waveform with $w(t)$.

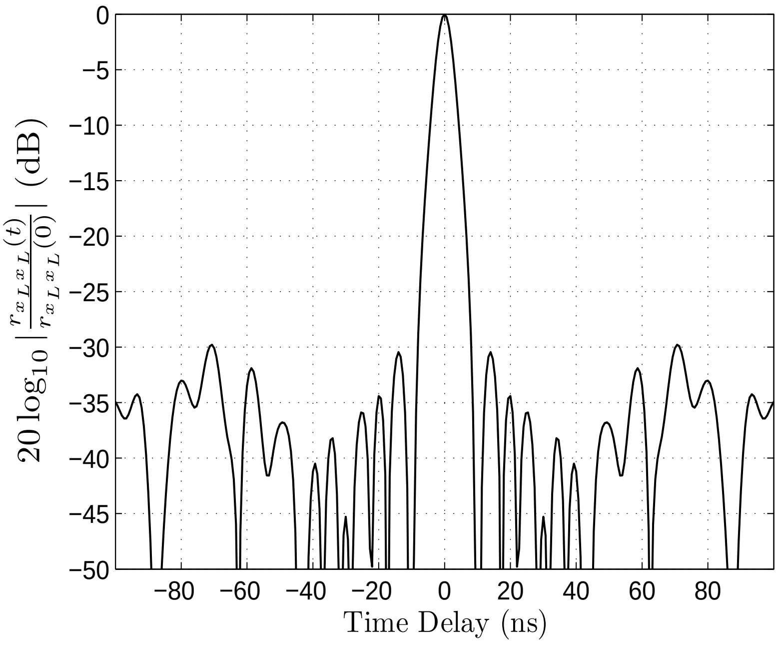

Figure 5-1: Autocorrelation Function of a Lorenz Waveform. This waveform is generated from the system given in Eq. 5.1.

The autocorrelation function of $w(t)$ is shown in Fig. 5-2. The side-lobe level is lower and the main-lobe width is narrower than the autocorrelation function of the Lorenz waveform given in Fig. 5-1. The peak side-lobe, average side-lobe level, and main-lobe width of the autocorrelation function of $w(t)$ evaluate to be -31 dB, -44 dB, and 1.8 ns, respectively. Consequently, due to a lower peak side-lobe and narrower main-lobe width, the autocorrelation function of $w(t)$ is usually better suited for radar applications than the autocorrelation function of $x_L(t)$.

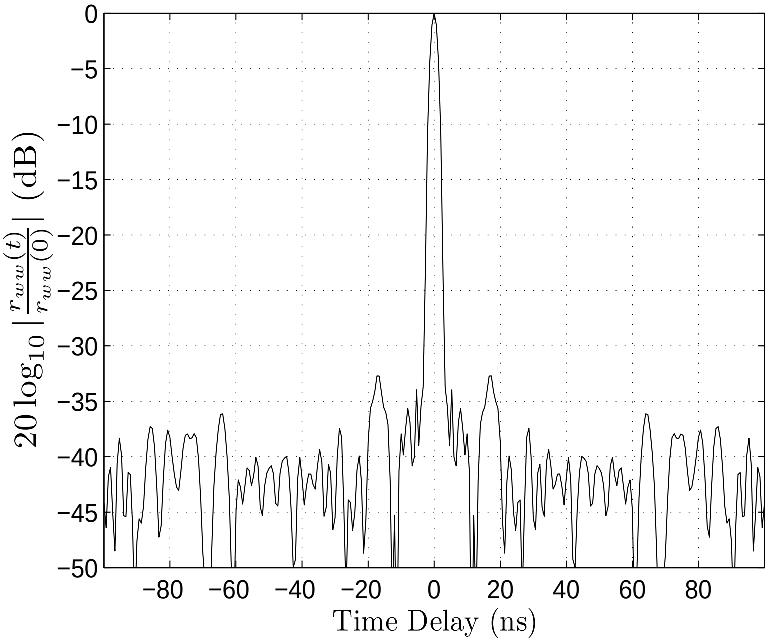

Figure 5-2: Autocorrelation Function for $w(t)$.

### 5.1.3 Energy Spectrum

The next comparison is associated with comparing the metrics associated with the energy spectra of the two waveforms. The metric associated with the energy spectrum is the peak out-of-band side-lobe. However, severe qualitative differences exist between the energy spectra of $x_L(t)$ and $w(t)$. Consequently, comparing the energy spectra with this metric is ambiguous. Specifically, for the triangular-like spectrum of the Lorenz waveform, the frequencies that correspond to the out-of-band region is somewhat arbitrary. Thus, the energy spectra of these two waveforms will just be compared qualitatively, which is sufficient to illustrate the significant differences between the energy spectrum of the two waveforms.

The energy spectra of both waveforms are calculated in order to make a comparison. The energy spectrum for one particular, 20 $\mu$s, Lorenz waveform, $x_L(t)$, is given in Fig. 5-3 and is calculated as described in Eq. 3.22. The energy spectrum of $w(t)$ is given in Fig. 5-4. For a compact spectrum, it is important (for reasons listed in

Chapter 3) that most of the energy in the energy spectrum be concentrated in the in-band region, [-250 MHz, 250 MHz], and little energy should be located outside the in-band region. When comparing the two spectrums, the energy spectrum of $w(t)$ appears to be more compact than the energy spectrum of $x_L(t)$. First, the energy spectrum of $w(t)$ in the in-band region appears to be more evenly distributed, which translates into a smaller main-lobe width of the autocorrelation function of $w(t)$. Secondly, the out-of-band energy is significantly less than the in-band energy for $w(t)$. On the other hand, since the energy spectrum of $x_L(t)$ falls off somewhat linearly (on a semi-log plot), the in-band energy is not significantly more than the out-of-band energy. Consequently, $x_L(t)$ will see more distortion than $w(t)$ due to filters in the radar hardware that further attenuate energy outside of the in-band region. When compared to the energy spectrum of $w(t)$, the energy spectrum of $x_L(t)$ does not appear to be very compact. However, Section 5.2 addresses issues involved with making the spectrum more compact.

### 5.1.4 Cross-Correlation Function

The next comparison requires evaluating the peak side-lobe of the cross-correlation function of two distinct Lorenz waveforms and comparing it with $w(t)$ and the quasi-orthogonal counterpart to $w(t)$. A sample cross-correlation function of two distinct Lorenz waveforms, $x_{L1}(t)$ and $x_{L2}(t)$, is shown in Fig. 5-5. Even though only the cross-correlation of two waveforms is shown, this function is typical of all observed cross-correlation functions for all distinct Lorenz waveforms. The peak side-lobe level, although not shown in the figure, was evaluated to be -25.4 dB. The average side-lobe level was evaluated to be -42.7 dB, which verifies that the waveforms are quasi-orthogonal, since $-20\log_{10}(\sqrt{LB}) = -40$ (where $LB$ denotes the time-bandwidth product).

Figure 5-6 plots the cross-correlation of $w(t)$ with a second waveform, $\tilde{w}(t)$, designed at M.I.T. Lincoln Laboratory, which is being used as a quasi-orthogonal counterpart to the original $w(t)$. The average side-lobe level and the peak side-lobe for these two waveforms are -43.9 dB and -28.7 dB, respectively. Thus these two wave-

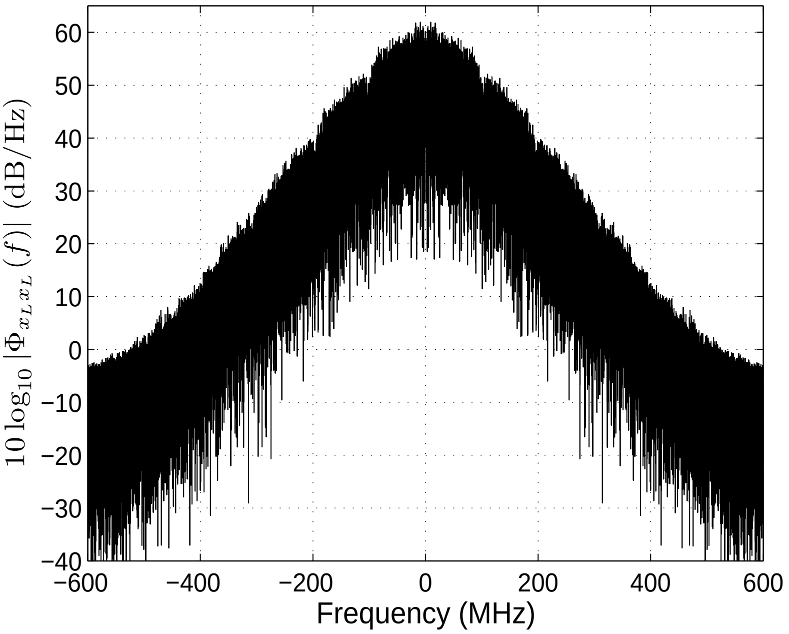

Figure 5-3: Energy Spectrum of a Lorenz Waveform. This is the energy spectrum for one particular Lorenz waveform and is calculated using Eq. 3.22.

forms are indeed quasi-orthogonal. When comparing the cross-correlation function of the Lorenz waveforms with the cross-correlation function of $w(t)$ and $\tilde{w}(t)$, the cross-correlation properties are roughly equivalent.

## 5.2 Transformations to Improve the Lorenz Radar Waveforms

As indicated in the previous section, Lorenz waveforms do not evaluate well on the radar design goals when compared to radar waveforms used in current applications. In this section, small modifications to the Lorenz waveforms will be suggested so that the new, Lorenz-based waveforms offer a valid set of quasi-orthogonal radar waveforms that evaluate just as well on the radar design goals as quasi-orthogonal radar waveforms used in current applications. In fact, Lorenz-based waveforms perform better

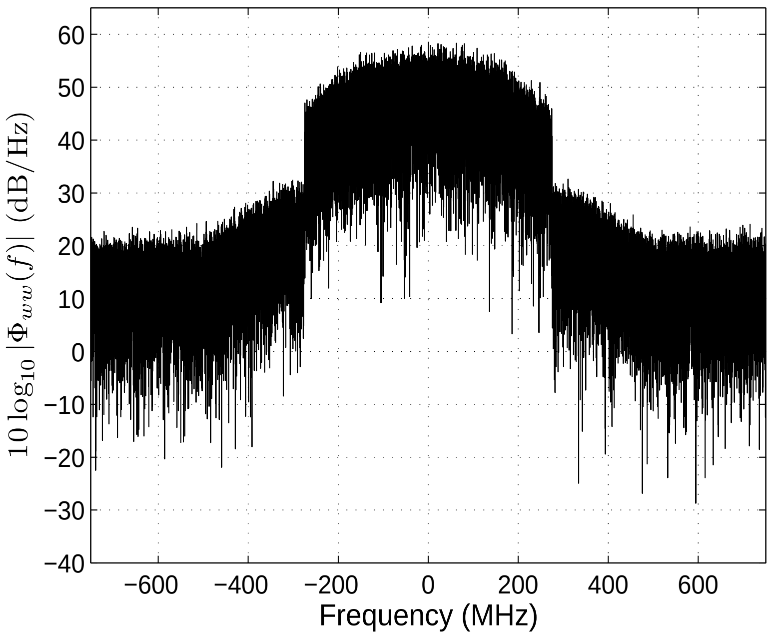

Figure 5-4: Energy Spectrum of $w(t)$.

than current radar waveforms on some of the design goals. The result of this section will be a systematic procedure for generating sets of quasi-orthogonal waveforms.

### 5.2.1 Peak-to-RMS Ratio Improvement

As mentioned in the previous section, Lorenz waveforms possess a relatively high peak-to-RMS ratio. The high PRMS of $x_L(t)$ is due, in large part, to the lack of an imaginary component to $x_L(t)$, since the Lorenz waveforms are real signals. Since $x_L(t)$ is a wideband waveform, it must consist of spectral components other than just the DC component, which forces the real signal $x_L(t)$ to vary in magnitude with time. This variation results in a PRMS greater than unity[1]. However, if a waveform consisted of both a real and imaginary component, then low power regions of the real component could be aligned with high-power regions of the imaginary component. This alignment of the real and imaginary components reduces the fluctuation in the

---

[1] As explained in Section 3.1, since $x_L(t)$ is centered around base-band, the PRMS should be as close to unity as possible.

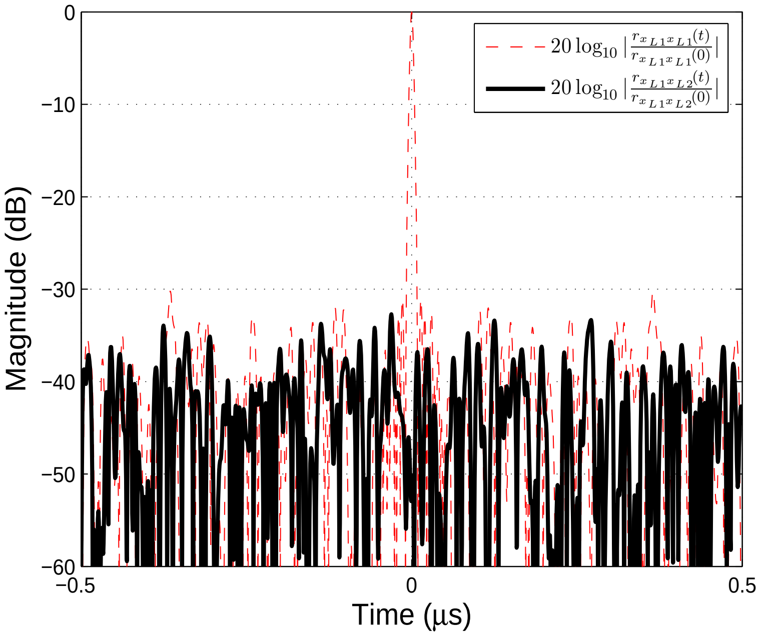

Figure 5-5: Cross-Correlation Between Two Distinct Lorenz Waveforms. The autocorrelation function is plotted lightly behind the cross-correlation function to demonstrate that average cross-correlation function is $20\log_{10}\left(\sqrt{TB}\right) = 40$ dB below the peak of the autocorrelation function of one waveform.

magnitude of the waveform, which results in a lower PRMS.

An example of this alignment can be demonstrated with the complex exponential. For the complex exponential, $e^{jw_c t}$, the real component is $\cos(w_c t)$, and the imaginary component is $\sin(w_c t)$. Moreover, low power regions of the real component align with the high power regions of the imaginary component, and vice-versa. Accordingly, the magnitude of the complex exponential is constant since $\|e^{jw_c t}\| = \sqrt{\cos^2(w_c t) + \sin^2(w_c t)} = 1$. Consequently since the peak equals unity, the PRMS, likewise, equals unity. Interestingly, since $\sin(w_c t) = \cos(w_c(t - \frac{\pi}{2w_c}))$, the imaginary component of the exponential is just a delayed version of the real component that minimizes the PRMS.

Using this intuition, an imaginary component is introduced for the Lorenz waveforms, which is simply the delayed version of the real component that minimizes the

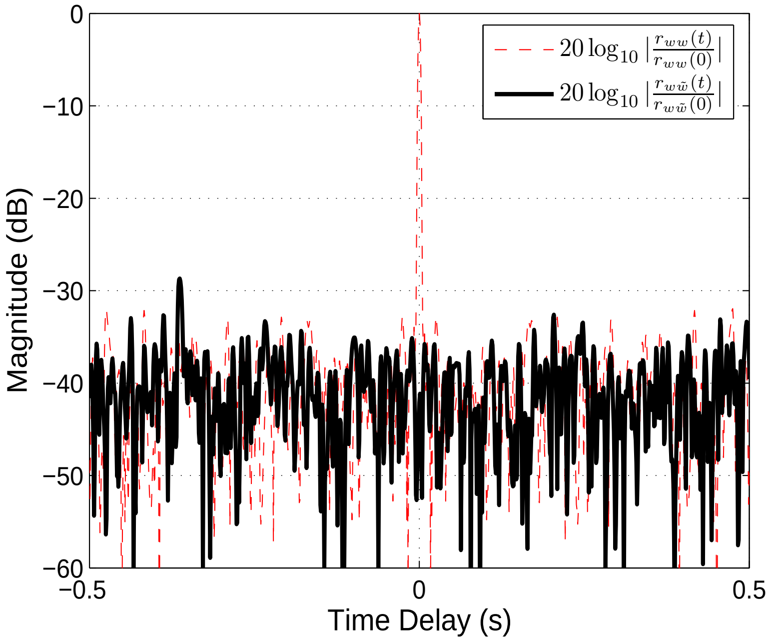

Figure 5-6: Cross-Correlation Between Two Quasi-Orthogonal Radar Waveforms. The autocorrelation function is plotted lightly behind the cross-correlation function to demonstrate that average cross-correlation function is $20\log_{10}\left(\sqrt{TB}\right) = 40$ dB below the peak of the autocorrelation function of one waveform.

PRMS. Thus, the objective is to choose the delay such that high power regions of the real component will align with the low power regions of the imaginary component[2]. The new waveform is now complex and is shown in Eq. 5.2, where $\tau_d$ is determined empirically from $x$ state variable of the Lorenz system.

$$x_1(t) \quad = \quad x_L(t) + jx_L(t-\tau_d) \tag{5.2}$$

However, using a delayed version of the real component as the imaginary component will have ramifications on the autocorrelation function of the complex waveform. The real and imaginary components of the autocorrelation function of $x_1(t)$, $r_{x_1x_1}(t)$,

---

[2] As shown in Section 4.2, consecutive peaks of the Lorenz waveform arrive at about the same time, which allows for the application of low and high power alignment.

is given in Eqs. 5.3. - 5.6.

$$\begin{aligned}
\Re\{r_{x_1x_1}(\tau)\} &= \int_{-\infty}^{+\infty} [x_L(t)x_L(t-\tau) + x_L(t-\tau_d)x_L(t-\tau_d-\tau)]dt && (5.3)\\
&= 2r_{x_Lx_L}(\tau) && (5.4)\\
\Im\{r_{x_1x_1}(\tau)\} &= \int_{-\infty}^{+\infty} [x_L(t-\tau_d)x_L(t-\tau) + x_L(t)x_L(t-\tau_d-\tau)]dt && (5.5)\\
&= r_{x_Lx_L}(\tau-\tau_d) - r_{x_Lx_L}(\tau+\tau_d) && (5.6)
\end{aligned}$$

As expected, $\|r_{x_1x_1}(\tau)\|$ has a global maximum at $\tau = 0$, since $\Re\{r_{x1x1}(\tau)\} = 2r_{x_Lx_L}(\tau)$. However, $|\Im\{r_{x_1x_1}(\tau)\}|$ introduces two additional relative maxima at $\tau = \pm\tau_d$, which can be seen in Eq. 5.6. These additional side-lobes could potentially give rise to false targets in a radar system and need to be eliminated.

To eliminate the high side-lobes at $\pm\tau_d$ while still maintaining a low peak-to-RMS ratio, Eq. 5.2 is redefined as shown in Eq. 5.7 and 5.8.

$$\begin{aligned}
x_2(t) &= x_L(t) + j\tilde{x}(t) && (5.7)\\
\tilde{x}(t) &= \begin{cases} x_L(t-\tau_d); & t \in [0, \frac{T}{2}] \\ -x_L(t-\tau_d); & t \in (\frac{T}{2}, T] \\ 0; & else \end{cases} && (5.8)
\end{aligned}$$

The autocorrelation function of $x_2(t)$ has the same real part, but $|\Im\{r_{x_2x_2}(\tau)\}|$ no longer has relative maxima at $\tau = \pm\tau_d$. To see this, first $\Im\{r_{x_2x_2}(\tau)\}$ is written out in Eq. 5.9 and 5.10.

$$\begin{aligned}
\Im\{r_{x_2x_2}(\tau)\} &= \int_{-\infty}^{+\infty} [\tilde{x}(t)x_L(t-\tau) + x_L(t)\tilde{x}(t-\tau)]dt && (5.9)\\
&= r_{\tilde{x}x_L}(\tau) - r_{x_L\tilde{x}}(\tau) && (5.10)
\end{aligned}$$

Next, Eq. 5.9 can be evaluated to show that no relative maxima exist at $\tau = \pm\tau_d$. Eq. 5.9 is evaluated first at $\tau = \tau_d$.

$$\Im\{r_{x_2x_2}(\tau_d)\} = \int_{-\infty}^{+\infty} \left[\tilde{x}(t)x_L(t-\tau_d) + x_L(t)\tilde{x}(t-\tau_d)\right] dt \qquad (5.11)$$

$$
\begin{aligned}
&= \int_{-\infty}^{\frac{T}{2}} \left[x_L(t-\tau_d)x_L(t-\tau_d) + x_L(t)x_L(t-2\tau_d)\right] dt \qquad (5.12)\\
&\quad - \int_{\frac{T}{2}}^{+\infty} \left[x_L(t-\tau_d)x_L(t-\tau_d) + x_L(t)x_L(t-2\tau_d)\right] dt\\
&\approx 0 \qquad (5.13)
\end{aligned}
$$

Equation 5.12 is derived by substituting Eq. 5.8 for $\tilde{x}(t)$ into Eq. 5.11 and by breaking the integral apart into two time segments. Both integrals in Eq. 5.12 evaluate about the same magnitude and cancel so that Eq. 5.12 evaluates to approximately zero. A similar evaluation could be performed to demonstrate that $r_{x_2x_2}(-\tau_d) \approx 0$. Thus, the spurious peaks of $|\Im\{r_{x_2x_2}(\tau)\}|$ have been eliminated and high magnitude time segments of $\Re\{x_2(t)\}$ are aligned with low magnitude time segments of $\Im\{x_2(t)\}$.

The peak-to-RMS ratio of the complex, base-band waveform $x_2(t)$ can now be evaluated and compared with the original waveform, $x_L(t)$. The PRMS of $x_2(t)$ was calculated over 10 different waveforms and the mean PRMS and maximum PRMS were 1.5774 and 1.5912, respectively. The mean PRMS and maximum PRMS of $x_L(t)$ were calculated to be 2.2082 and 2.2211, respectively. As expected the PRMS is considerably lower in $x_2(t)$ than $x_L(t)$; however, this improvement, while encouraging, is not enough.

To further reduce the peak-to-RMS ratio, a mapping is introduced to force the trajectory to spend more time near the peak value. Accordingly, the following mapping in Eq. 5.14 is introduced to create a new waveform with a lower PRMS (where $\|\cdot\|$ denotes $\sqrt{(\cdot)(\cdot)^*}$). A plot demonstrating this concave mapping is shown in Fig. 5-7. As can be seen in this figure, this mapping boosts segments of the trajectory with low instantaneous power and only slightly affects time segments with a high instantaneous power. It is true that there might be other functions that might be more suitable in reducing the PRMS, but this function is sufficient for the purposes of this thesis.

$$
f_c(x) = \sin\left(\frac{\pi\sqrt{\|x\|}}{2\max\left[\sqrt{\|x\|}\right]}\right) \qquad (5.14)
$$

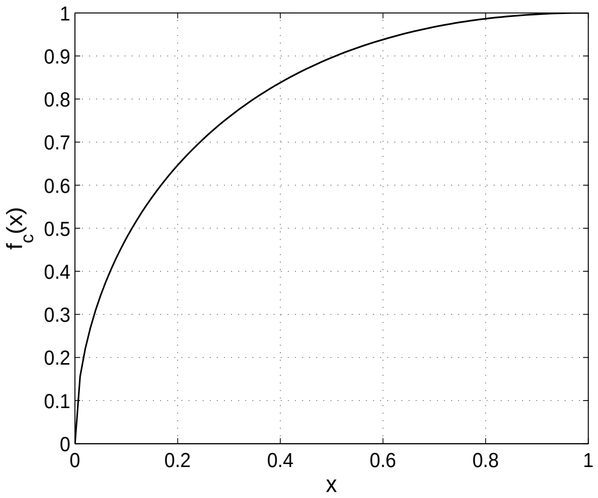

Figure 5-7: Mapping for $f_c(x)$. This mapping was used to boost the peak-to-RMS ratio of the waveforms in this thesis.

Using this mapping, a new waveform can be proposed that has a lower peak-to-RMS ratio but still remains closely based on the Lorenz system. This new waveform, $\hat{x}_3(t)$, is given in Eq. 5.15 where $\|\cdot\|$ denotes $\sqrt{(\cdot)(\cdot)^*}$ and $f_c^{(2)}(\cdot)$ denotes $f_c(f_c(\cdot))$.

$$\hat{x}_3(t) \quad = \quad f_c^{(2)}\left(x_2(t)\right) \cdot \frac{x_2(t)}{\|x_2(t)\|} \tag{5.15}$$

For a set of ten distinct waveforms, the average PRMS and maximum PRMS were 1.0140 and 1.0144, respectively. Alas, the PRMS of $\hat{x}_3(t)$ compares favorably against typical waveforms used in practice. However, due to the application of $f_c$, the energy spectrum, $\Phi_{\hat{x}_3\hat{x}_3}(j\omega)$, of $\hat{x}_3(t)$ has been altered as shown in Fig. 5-8. Also, the spectrum appears to have been compressed. Expanding and shaping $\Phi_{\hat{x}_3\hat{x}_3}(j\omega)$ without significantly boosting the PRMS will be addressed in the next section.

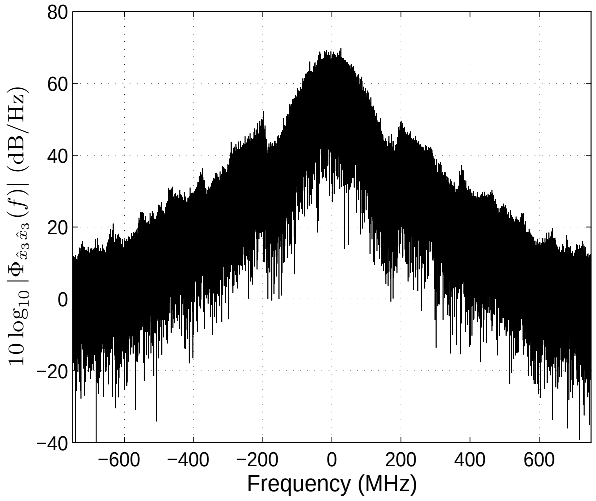

Figure 5-8: The Energy Spectrum of $\hat{x}_3(t)$.

### 5.2.2 Spectral Shaping

Properly shaping the spectrum of the Lorenz-based waveform will make the energy spectrum more compact and decrease the time width of the main-lobe of the autocorrelation function, without significantly boosting either the peak-to-RMS ratio or the side-lobes of the autocorrelation function. Shaping the spectrum (of $\hat{x}_3(t)$) is accomplished by a series of steps. First, the spectrum is expanded to correct for the compression due to the concave mapping, $f_c^{(2)}(x)$. Then, the expanded spectrum is filtered by a low-pass filter, which makes the spectrum compact. Finally, the in-band frequencies of the resulting waveform are shaped with a shaping filter, which trades-off autocorrelation main-lobe width with side-lobe area.

The first two necessary steps in shaping the spectrum of $\hat{x}_3(t)$ are shown in Fig. 5-9, and both the filter, $h_{lp}(t)$, and the value for $m$ need to be determined. $h_{lp}(t)$ is designed to be compatible with the waveform specifications given in Table 5.1, i.e. the width of the pass-band of $h_{lp}(t)$ was set to be approximately 500 MHz. The frequency response of this filter is given in Fig. 5-10. The value for $m$ in Fig. 5-9 (where for simplicity m is assumed to be greater than unity) scales the frequency axis of $\Phi_{\hat{x}_3\hat{x}_3}(j\omega)$, i.e. $\Phi_{x_3x_3}(j\omega) = \frac{1}{|m|}\Phi_{\hat{x}_3\hat{x}_3}(\frac{j\omega}{m})$. Moreover, since $h_{lp}(t)$ is fixed, $m$ is related

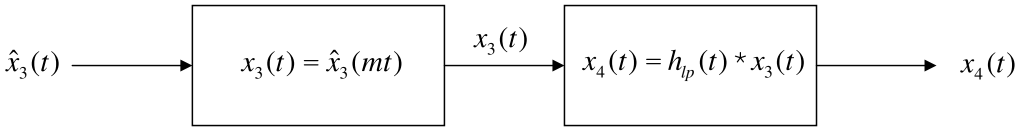

Figure 5-9: Time-Compression and Low-Pass Filtering of $\hat{x}_3(t)$.

to the frequency tapering of $\Phi_{x_4x_4}(j\omega)$, since when $\Phi_{x_3x_3}(j\omega)$ (shown in Fig. 5-8) is greatly expanded, the highly tapered regions of $\Phi_{x_3x_3}(j\omega)$ are outside of the pass-band of $h_{lp}(t)$ and significantly attenuated. Consequently, larger values of $m$ result in less tapering of $\Phi_{x_4x_4}(j\omega)$, and smaller values of $m$ result in more tapering of $\Phi_{x_4x_4}(j\omega)$. Since the in-band tapering is related to the main-lobe width of the autocorrelation function, $m$ is increased to 2.85 so that the main-lobe width of $r_{x_4x_4}(t)$ equals the main-lobe width of the autocorrelation function of $w(t)$ to make the comparison of the two waveforms easier (for more details, see the discussion of effective bandwidth versus time-width in [16]). The spectrum of the resulting waveform $x_4(t)$ is shown in Fig. 5-11.

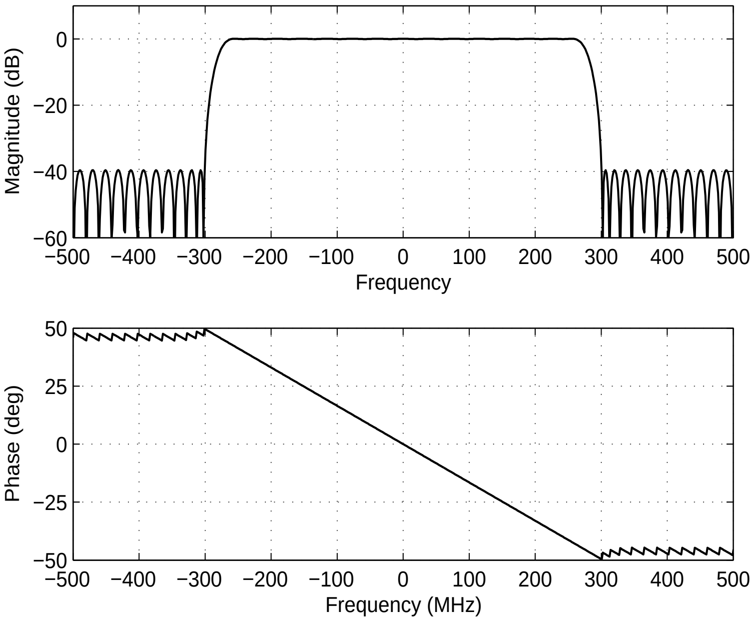

Figure 5-10: Frequency Response of $h_{lp}(t)$.

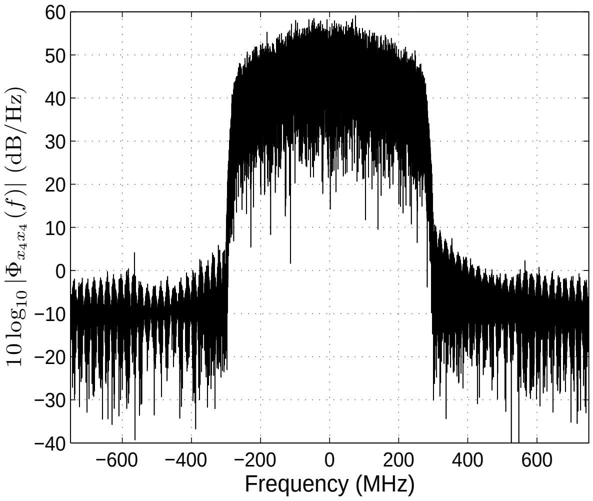

Figure 5-11: The Energy Spectrum of $x_4(t)$.

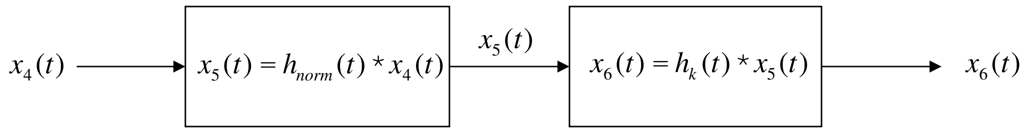

Figure 5-12: Steps Required for In-band Spectral Shaping

Now that $\Phi_{x_4x_4}(j\omega)$ is both more compact and gives rise to an autocorrelation function with a desirable main-lobe width, the in-band region of $\Phi_{x_4x_4}(j\omega)$ is further filtered to match the shape of a Kaiser window, since a Kaiser window almost optimally trades-off main-lobe width and side-lobe area [11]. Thus, the objective of this operation is to lower the side-lobes of the autocorrelation function without widening the main-lobe. To do so, a pseudo-normalization of the in-band region of $\Phi_{x_4x_4}(j\omega)$ is performed. Next, a Kaiser window is applied to the in-band region of $\Phi_{x_4x_4}(j\omega)$. These steps are expressed in Fig. 5-12[3].

The pseudo-normalization of the in-band region of $\Phi_{x_4x_4}(j\omega)$ was accomplished by dividing by an averaged approximation of $\Phi_{x_4x_4}(j\omega)$. This division is shown in Eqs 5.16 and 5.17 where $\hat{\Phi}_{x_4x_4}(j\omega)$ denotes the averaged approximation of $\Phi_{x_4x_4}(j\omega)$ and $\Phi_{x_5x_5}(j\omega)$ is the output of this shaping.

$$\Phi_{x_5x_5}(j\omega) = |H_{norm}(j\omega)|^2 \, \Phi_{x_4x_4}(j\omega) \tag{5.16}$$

$$|H_{norm}(j\omega)|^2 = \begin{cases} \frac{1}{\hat{\Phi}_{x_4x_4}(j\omega)}; & \omega \in [-\omega_c, \omega_c] \\ \frac{1}{\hat{\Phi}_{x_4x_4}(j\omega_c)}; & \omega \in (-\infty, -\omega_c) \cup (\omega_c, \infty) \end{cases} \tag{5.17}$$

In Eq. 5.17, the in-band region is defined as $\omega_c \in [-\omega_c, \omega_c]$. The in-band region is

---

[3] In a real radar, shaping the in-band frequencies of $\Phi_{x_4x_4}(j\omega)$ can be done either before transmitting the waveform or upon reception of the waveform. If the shaping is done before transmission, the peak-to-RMS is degraded, and the waveform could be distorted on transmit. If the shaping is done upon receive, a reduction in the signal-to-noise ratio occurs. The remainder of this section proceeds as if the spectrum is shaped prior to transmit, but the option exists to simply transmit $x_4(t)$ and taper the waveform on receive.

chosen to be consistent with the specifications in Table 5.1. Also, the out-of-band region is multiplied by a constant factor, $\frac{1}{\hat{\Phi}_{x_4x_4}(j\omega_c)}$, to ensure that there are no severe discontinuities in $\Phi_{x_5x_5}(j\omega_c)$. $\hat{\Phi}_{x_4x_4}(j\omega)$ is calculated using an averaged modified periodogram method[4].

Dividing the in-band region of $\Phi_{x_4x_4}(j\omega)$ by $\hat{\Phi}_{x_4x_4}(j\omega)$ (as opposed to $\Phi_{x_4x_4}(j\omega)$) was done to preserve a low peak-to-RMS ratio. If the in-band region was instead normalized to unity, the spectrum would be more greatly altered, which would raise the peak-to-RMS ratio to an unacceptable level[5]. However, when dividing the in-band region by $\hat{\Phi}_{x_4x_4}(j\omega)$, the minor distortion to $x_4(t)$ (which originally had a very low peak-to-RMS ratio) does not significantly raise the peak-to-RMS due to averaging involved in the calculation of $\hat{\Phi}_{x_4x_4}(j\omega)$.

The next step involves shaping the in-band region of $\Phi_{x_5x_5}(j\omega)$ with a kaiser window. The kaiser window depends on two parameters, the length of the window and the parameter, $\beta$, which trades off main-lobe width with side-lobe area. The length was determined by the length of the in-band region of $\Phi_{x_5x_5}(j\omega)$. $\beta$ was determined to ensure the resulting waveform had an autocorrelation function main-lobe width equal to the main-lobe width of $r_{ww}(t)$. Consequently, $\beta$ was chosen to be 4.75. The resulting Kaiser window is shown in Fig. 5-13.

Using $w_k(j\omega)$, the in-band region of $\Phi_{x_5x_5}(j\omega)$ was shaped as described in Eqs. 5.19 and 5.18 where $\Phi_{x_6x_6}(j\omega)$ is the output of this shaping.

$$\Phi_{x_6x_6}(j\omega) = |H_k(j\omega)|^2 \, \Phi_{x_5x_5}(j\omega) \tag{5.18}$$

$$|H_k(j\omega)|^2 = \begin{cases} w_k(j\omega); & \omega \in [-\omega_c, \omega_c] \\ w_k(j\omega_c); & \omega \in (-\infty, -\omega_c) \cup (\omega_c, \infty) \end{cases} \tag{5.19}$$

The in-band region is defined as $\omega_c \in [-\omega_c, \omega_c]$. Also, the out-of-band region is multiplied by a constant factor, $w_k(j\omega_c)$, to ensure that there are no severe discontinuities

---

[4] $\hat{\Phi}_{x_4x_4}(j\omega)$ was evaluated via Welch's averaged modified periodogram method with one exception. Welch's method uses eight segments of equal length with 50% overlap; whereas, the approximation computed herein uses fourteen segments of equal length with 50% overlap.

[5] If the in-band tapering is done upon receive, then one might consider normalizing the in-band spectrum to unity.

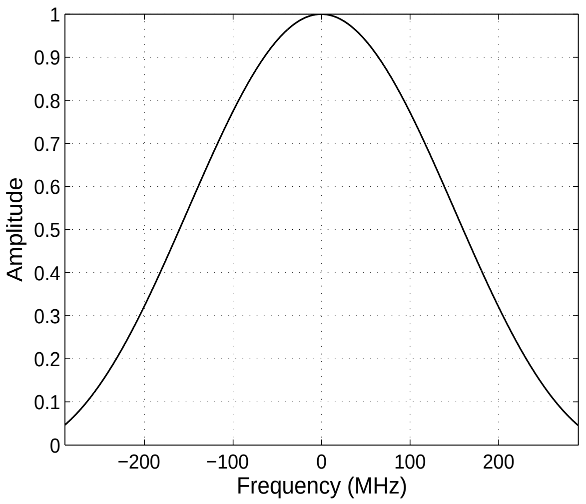

Figure 5-13: The Kaiser Window Used to Shape $\Phi_{x_5 x_5}(j\omega)$.

in $\Phi_{x_6 x_6}(j\omega_c)$. Thus, since the Kaiser filter is designed to trade-off main-lobe width and side-lobe area, the side-lobes of the autocorrelation function of $x_4(t)$ have also been reduced when compared to $x_L(t)$, which is shown in the next section.

For ease of implementation, both $H_{norm}(j\omega)$ and $H_k(j\omega)$ are combined into one shaping filter, $H_{min}(j\omega)$, which is shown in Fig. 5-14. The mathematical description

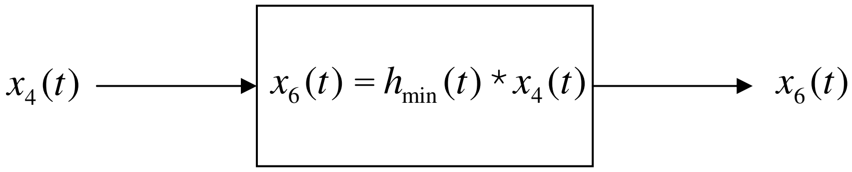

Figure 5-14: System Description of $H_{min}(j\omega)$.

for this filter is given in Eq. 5.20.

$$|H_{min}(j\omega)|^2 = \frac{\Phi_{x_6x_6}(j\omega)}{\Phi_{x_4x_4}(j\omega)} \tag{5.20}$$

By substituting Eq. 5.16 for $\Phi_{x_5x_5}(j\omega)$ in Eq. 5.18, $\Phi_{x_6x_6}(j\omega)$ can be expressed as shown in Eq. 5.21.

$$\Phi_{x_6x_6}(j\omega) = |H_{norm}(j\omega)|^2 \, |H_k(j\omega)|^2 \, \Phi_{x_4x_4}(j\omega) \tag{5.21}$$

Consequently, by substituting Eq. 5.21 into Eq. 5.20, the squared magnitude of $H_{min}(j\omega)$ can be described by Eq. 5.22, which can be evaluated as shown in Eq. 5.23.

$$|H_{min}(j\omega)|^2 = |H_{norm}(j\omega)|^2 \, |H_k(j\omega)|^2 \tag{5.22}$$

$$|H_{min}(j\omega)|^2 = \begin{cases} \frac{w_k(j\omega)}{\hat{\Phi}_{x_4x_4}(j\omega)}; & \omega \in [-\omega_c, \omega_c] \\ \frac{w_k(j\omega_c)}{\hat{\Phi}_{x_4x_4}(j\omega_c)}; & \omega \in (-\infty, -\omega_c) \cup (\omega_c, \infty) \end{cases} \tag{5.23}$$

To also determine the phase information of $H_{min}(j\omega)$, spectral factorization is employed to factor $|H_{norm}(j\omega)|^2 \, |H_k(j\omega)|^2$ into a minimum and a maximum phase component [12], as stated in Eq. 5.24. The magnitude squared of the minimum phase component satisfies Eq. 5.22.

$$|H_{norm}(j\omega)|^2 \, |H_k(j\omega)|^2 = H_{min}(j\omega) H_{max}(j\omega) \tag{5.24}$$

Herein, the Levinson-Durbin recursion algorithm was utilized estimate $H_{min}(j\omega)$ by approximating this factorization with an IIR filter.

Therefore, $h_{min}(t)$ (the inverse Fourier transform of $H_{min}(j\omega)$) can be used to shape the in-band frequencies of $\Phi_{x_4x_4}(j\omega)$ in order to reduce the side-lobes of the autocorrelation function of $x_4(t)$. This operation is illustrated in Fig. 5-14 and described by Eqs. 5.25 and 5.26.

$$
\begin{aligned}
x_6(t) &= h_{min}(t) * x_4(t) && (5.25)\\
|H_{min}(j\omega)|^2 &= \begin{cases} \frac{w_k(j\omega)}{\hat{\Phi}_{x_4x_4}(j\omega)}; & \omega \in [-\omega_c, \omega_c] \\ \frac{w_k(j\omega_c)}{\hat{\Phi}_{x_4x_4}(j\omega_c)}; & \omega \in (-\infty, -\omega_c) \cup (\omega_c, \infty) \end{cases} && (5.26)
\end{aligned}
$$

Since shaping $\Phi_{x_4x_4}(j\omega)$ boosts the PRMS of $x_6(t)$, the amplitude of $x_6(t)$ is clipped to lower the peak-to-RMS to a reasonable level. This was a simple operation accomplished by simply re-normalizing the amplitude of $x_6(t)$ by dividing by 0.7 and then setting all values of $|x_6(t)| > 1$ equal to unity in magnitude as described by Eq. 5.27. The PRMS of the resulting waveform, $\mu_L(t)$, was calculated over 10 different waveforms and the mean PRMS and maximum PRMS were 1.22 and 1.26, respectively.

$$
\mu_L(t) = \begin{cases} \frac{1}{0.7} \cdot x_6(t) & \texttt{if } \frac{\|\texttt{x}_6\texttt{(t)}\|}{0.7} < 1 \\ \frac{1}{0.7 \cdot \|x_6(t)\|} x_6(t) & \texttt{if } \frac{\|\texttt{x}_6\texttt{(t)}\|}{0.7} \geq 1 \end{cases} \qquad (5.27)
$$

Thus, as a result of this section, the original Lorenz waveform, $x_L(t)$, has been modified in a systematic way to both correct for the PRMS and to decrease the main-lobe width of the autocorrelation function and to make the spectrum more compact. The systematic procedure developed in this thesis to generate Lorenz-based radar waveforms is shown in Fig. 5-15. The new, Lorenz-based waveform, $\mu_L(t)$, will be evaluated in the next section.

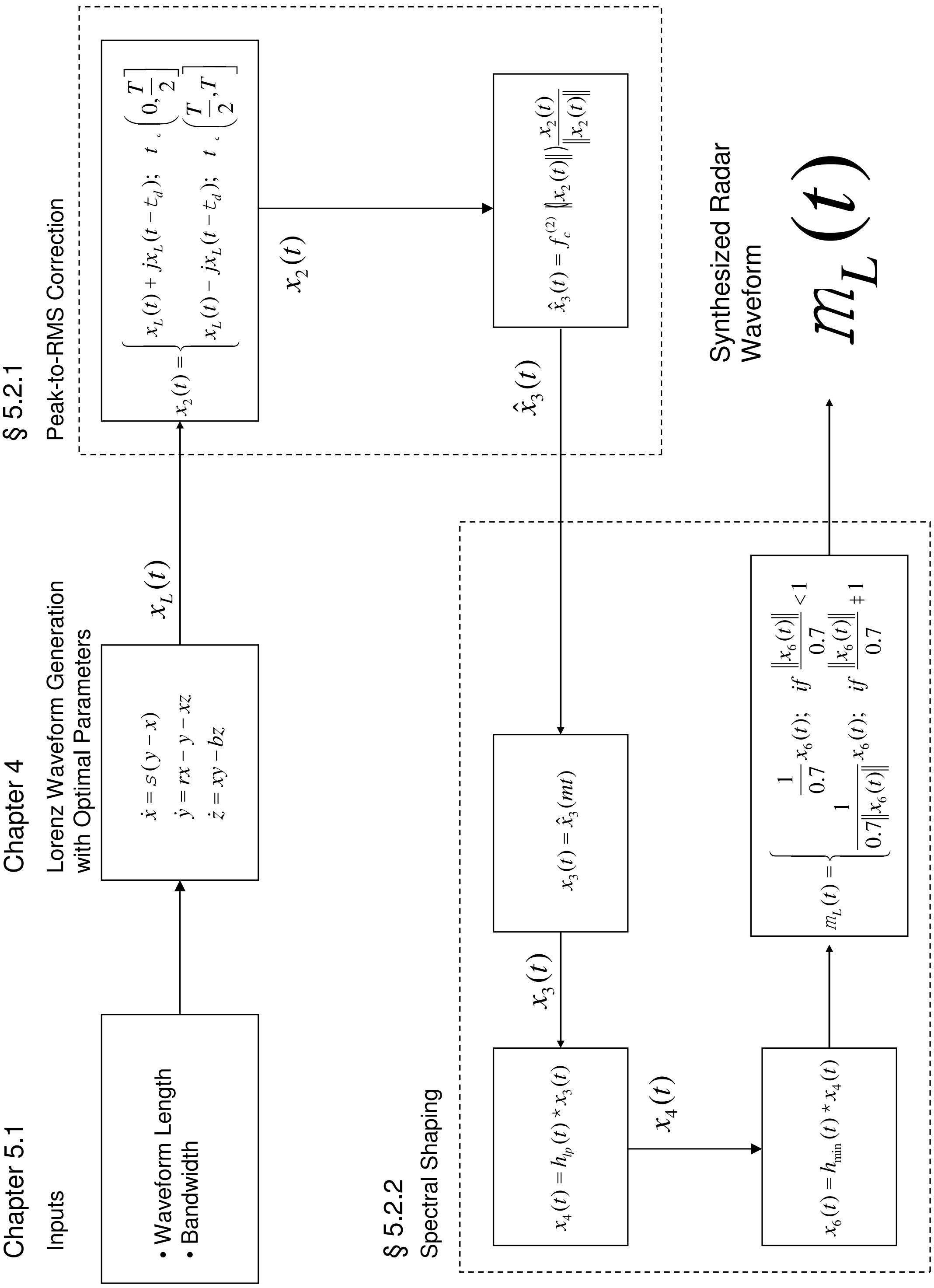

Figure 5-15: Systematic Procedure for Generating Lorenz-Based Waveforms.

## 5.3 Evaluating the Transformed Lorenz Radar Waveforms

The Lorenz-based waveforms, $\mu_L(t)$, perform much better than the original Lorenz waveforms, and in some ways, out perform $w(t)$, the waveform used in practice. Moreover, the waveform $w(t)$ was generated via a long numerical optimization program that lasts several hours to even days when generated on a desktop machine using Matlab. On the other hand, utilizing the Lorenz system, Lorenz-based radar waveforms can be generated very quickly (seconds in Matlab) suggesting the potential of generating these waveforms in real-time on a pulse-to-pulse basis in a radar. The objective of this section is to evaluate the Lorenz-based waveforms based on the radar waveform design goals and compares them with $w(t)$. The output radar waveforms all were compatible with the system specifications given in Table 5.1.

### 5.3.1 Peak-to-RMS Ratio

After taking steps to reduce the PRMS of the Lorenz waveforms (most importantly by adding an imaginary component to the Lorenz waveforms), the PRMS of the resulting Lorenz-based waveforms is significantly reduced. As mentioned earlier the mean PRMS of $\mu_L(t)$ over ten distinct waveforms is 1.22 and the peak value is 1.26. Since the PRMS of $w(t)$ 1.21, it is concluded that the PRMS of the Lorenz-based waveforms is roughly equal in value to that of $w(t)$.

### 5.3.2 Autocorrelation Function

The autocorrelation function of the Lorenz-based waveform demonstrates both a narrower main-lobe and lower side-lobes than the original Lorenz waveform. The narrow main-lobe is due to shaping the in-band frequencies of the energy spectrum of the original Lorenz waveform to create a larger effective bandwidth for the system. Moreover, application of the filter described in Eq. 5.26 effectively lowers the side-lobes centered around the main-lobe of the autocorrelation function. Both of these effects can be seen in Fig. 5-16. The autocorrelation function is plotted alongside the autocorrelation function of $w(t)$ to demonstrate an equal main-lobe width and lower side-lobes. Specifically, without applying $h_{min}(t)$, the side-lobes of $r_{\mu_L \mu_L}(t)$ would be on the order of $20 \log |\sqrt{LB}|$ below the main-lobe, as is the case for the side-lobes of $r_{ww}(t)$. With the application of $h_{min}(t)$, the side-lobes of $r_{\mu_L \mu_L}(t)$ centered around the main-lobe are lowered an additional 10 dB[6].

### 5.3.3 Energy Spectrum

The triangular-like energy spectrum of the original Lorenz waveforms has been modified to make the spectrum more compact. The original energy spectrum (given in Fig. 5-3) has been transformed through spectral shaping into a more compact energy spectrum. The energy spectrum for an example Lorenz-based radar waveform is given in Fig. 5-17, which was computed via Eq. 3.22. As can be seen from the figure, less out-band energy exists in Fig. 5-17 than Fig. 5-3 (where in-band is defined as the 500 MHz region centered around zero as specified by Table 5.1). Moreover, the energy spectrum is of comparable compactness as the energy spectrum of $w(t)$, which is given in Fig. 5-4.

### 5.3.4 Cross-Correlation Function

The cross-correlation level of the Lorenz-based radar waveform is unaffected by the operations that modify $x_L(t)$. The cross-correlation function of two distinct Lorenz-based waveforms, $\mu_{L1}(t)$ and $\mu_{L2}(t)$, is shown in Fig. 5-18 where the autocorrelation function of one of the waveforms is plotted lightly behind the cross-correlation function. The time-bandwidth product remains at -40 dB; thus, the average cross-correlation level is expected to be located around -40 dB. The average side-lobe level and peak side-lobe of the cross-correlation function was calculated to be -44.56 and -28.04, respectively. Therefore, as expected the cross-correlation between two distinct

---

[6] Remembering that the autocorrelation function is the zero-doppler slice of the ambiguity function is important. A full ambiguity function is given in the appendix, which illustrates the low side-lobes in both time and doppler. Also, the appendix demonstrates how these low side-lobes are not degraded by a radar transmitter.

Lorenz-based waveforms remains low and comparable to both the original Lorenz waveforms (as shown in Fig. 5-5) and the cross-correlation level between $w(t)$ and $\tilde{w}(t)$, which are both being used in current applications (as shown in Fig. 5-6).

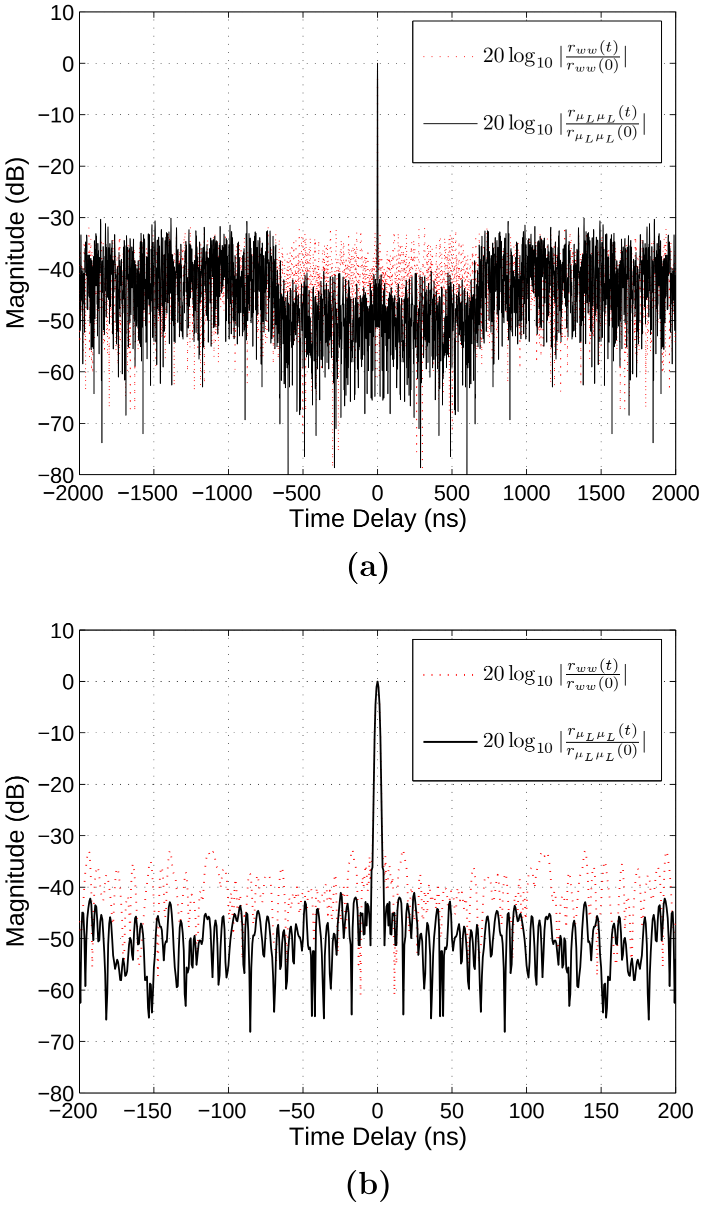

Figure 5-16: The Autocorrelation Function of $\mu_L(t)$. This figure plots the autocorrelation function of $\mu_L(t)$, $r_{\mu_L\mu_L}(t)$. Behind is the autocorrelation function of $w(t)$, $r_{ww}(t)$. The second plot is an enlarged view of the first plot.

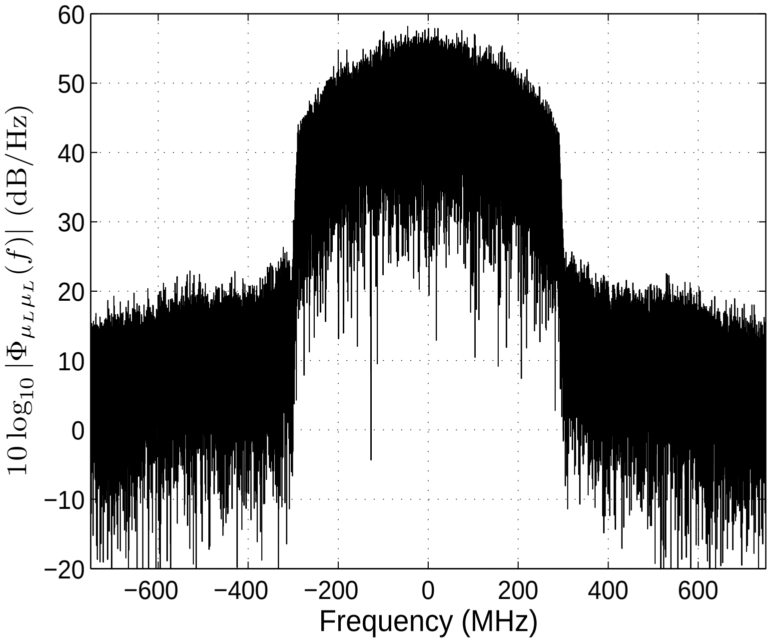

Figure 5-17: The Energy Spectrum of $\mu_L(t)$.

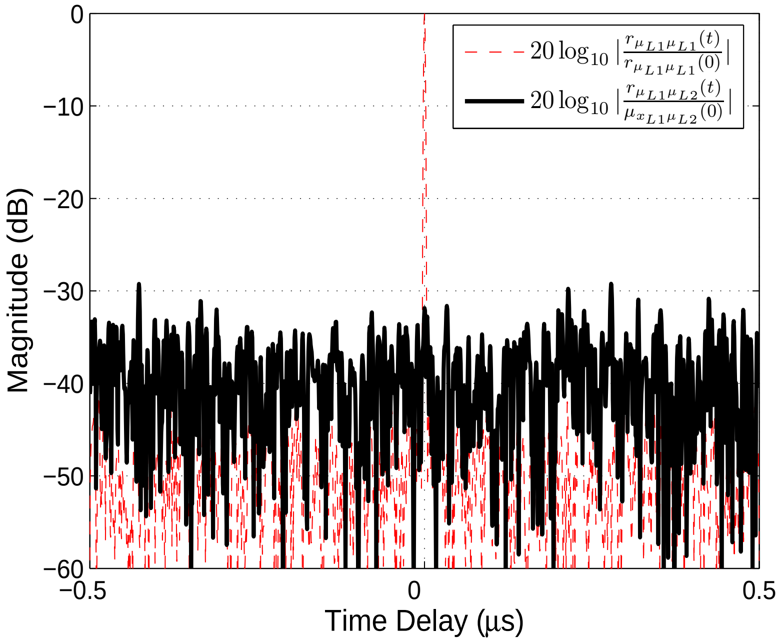

Figure 5-18: Cross-Correlation Between Two Distinct Lorenz-based Waveforms. The autocorrelation function is plotted lightly behind the cross-correlation function. The function $r(t)$ denotes the cross-correlation function of $\mu_L(t)$.

# Chapter 6

# Summary and Suggestions for Future Research

This chapter summarizes the thesis and also suggests various directions for future work.

## 6.1 Summary

As discussed in the introduction, the development of A/D converters possessing sufficiently high sampling rates allows the use of arbitrary, wideband waveforms in radar applications. This thesis studies the utilization of the Lorenz system to generate large sets ($> 50$) of high-quality, wideband, quasi-orthogonal radar waveforms. The systematic waveform generating procedure is closely based on the Lorenz system and requires only a few seconds to generate each waveform in Matlab. Additionally, each waveform can be represented by 6 parameters: three initial conditions and the Lorenz parameters, $\sigma$, $r$, and $b$.

Chapter 3 proposes and explains four radar waveform design considerations. The four design considerations are (i) the peak-to-RMS ratio, (ii) the autocorrelation function, (iii) the power spectrum, and (iv) the cross-correlation function. These design considerations are used to evaluate waveforms in this thesis.

Chapter 4 demonstrates that scaling the Lorenz parameters approximately time and amplitude scale the state variables of the Lorenz system. This scaling is exploited such that one parameter, $b$, sets the bandwidth and the remaining two parameters, $\sigma$ and $r$, set the remaining system properties. Specifically, for a fixed value of $b$, $\sigma$ and $r$ can be chosen to minimize the autocorrelation function side-lobes, as well as reduce the peak-to-RMS ratio of the Lorenz waveform. The trade-off between side-lobes and peak-to-RMS ratio is summarized by the design curves in Fig. 4-13.

As well as providing a method for selecting the Lorenz parameters, Chapter 4 verifies that the Lorenz system can be used to generate quasi-orthogonal waveforms and suggests two distinct methods for time-scaling the Lorenz system. The first method, via scaling the Lorenz equations, is exact. The second method, via scaling the Lorenz parameters, is approximate. This second method provides two additional insights. First, the parameters being used to set the bandwidth can be decoupled from the parameters being used to set other system properties. The second insight reveals the existence of other chaotic systems where scaling the parameters corresponds exactly to time and amplitude scaling of the state variables. Several such systems are suggested, but the dynamics of these systems are yet to be explored.

Chapter 5 discusses how the x state variable from the Lorenz system can be used to generate practical radar waveforms. This discussion begins by illustrating the deficiencies in using the Lorenz waveform as a radar waveform. Based on these weaknesses, a correction procedure is suggested to modify the Lorenz waveform. This procedure is summarized by Fig. 5-15. The resulting Lorenz-based waveform, $\mu_L(t)$, is then compared with a sample radar waveform, $w(t)$, which is taken from a set of quasi-orthogonal radar waveforms used in practice at M.I.T. Lincoln Laboratory and generated from a method independent of deterministic chaos. The comparison illustrates that the peak-to-RMS ratio, the energy spectrum, and the cross-correlation function are, more or less, equivalent for the two waveforms[1]. However, the autocorrelation function of $\mu_L(t)$ has considerably lower side-lobes centered around the main-lobe[2]. Moreover, generating $w(t)$ requires many hours. Generating $\mu_L(t)$ requires

---

[1] The appendix describes how to also reduce the PRMS of the Lorenz-based waveform to a level significantly less than the PRMS of $w(t)$.

[2] The appendix illustrates that these low side-lobes can be realized in practice.

only a few seconds, and unlike $w(t)$, each Lorenz-based waveform can be represented with only 6 finite-precision parameters.

By combining the highlights from each chapter, a concise summary of the entire thesis can be expressed in just two figures. The first, Fig. 4-13, describes how to optimally choose the Lorenz parameters to trade-off side-lobe level of the autocorrelation function with the peak-to-RMS ratio of the Lorenz waveform. The second, Figure 5-15, describes the operations that are performed on the Lorenz waveform to arrive at a Lorenz-based waveform, which outperforms sample waveforms employed in current radar applications.

## 6.2 Future Research Directions

Two significant directions are explored within this thesis. One direction is a study of the parameter space of the Lorenz system as described by Chapter 4. Another direction addresses various practical radar design issues when generating radar waveforms via the Lorenz system. These directions can be used to illustrate the clearest avenues for future research.

From the discussion of scaling the Lorenz parameters to approximately time and amplitude scale the Lorenz system, two major extensions are suggested. The first extension involves the reduction of the three-dimensional parameter space to two dimensions by decoupling $\sigma$ and $r$ from $b$. This new two-dimensional parameter space has only been explored in the context of radar waveforms. However, exploration of arbitrary properties and dynamics in this parameter space has been neglected. For example, the changes in the attractor shape appear easier to visualize when two parameters are varied, as opposed to three parameters. Moreover, when $r$ is fixed, the transition rate of the Lorenz system behaves somewhat symmetrically for increasing values of $\sigma$, i.e. the transition rate first decreases, and then begins increasing until the system is no longer exhibits chaotic dynamics. Thus, perhaps this symmetrical behavior can be quantified and understood.

The second extension of the parameter space involves the exploration of chaotic systems introduced in Chapter 4. Scaling the parameters of these systems results in an exact time and amplitude scaling of the corresponding state variables. Specifically, the Lorenz system for large parameter values appears to exhibit similar dynamics as one of the systems introduced in Section 4.3.3. Consequently comparing the two systems might provide insight into the dynamics of the Lorenz system at all parameter values.

There are numerous directions of research in utilizing chaos theory to generate practical radar waveforms. The systematic procedure used to generate radar waveforms could be improved. Also, the synchronization property of Lorenz system has not been exploited in either the waveform design procedure or when processing the radar waveform after reception.

Also, as mentioned in Section 5.2.2, it is not clear how much spectral shaping (by application of $h_{min}(t)$) should take place before transmit versus after receive. For example, if frequency shaping is not applied until after receiving the radar waveform, this new waveform, which we will call $\hat{\mu}_L(t)$, will have a lower peak-to-RMS ratio but higher side-lobes in the autocorrelation function[3]. Using $\hat{\mu}_L(t)$ for transmission and applying the shaping filter on receive (which trades off side-lobes with the signal-to-noise ratio) might be more advantageous in certain applications than using $\mu_L(t)$ for transmission. Thus a study contrasting the practical trade-offs between $\hat{\mu}_L(t)$ or $\mu_L(t)$ would be very useful.

---

[3] When compared with $w(t)$, the new transmitted waveform will have a lower peak-to-RMS ratio and comparable side-lobes. Since the peak-to-RMS of $\hat{\mu}_L(t)$ is lower than the peak-to-RMS of $w(t)$, the degradation of the signal-to-nose ratio might be less when using $\hat{\mu}_L(t)$ as opposed to $w(t)$ when both waveforms are spectrally shaped on receive to lower the autocorrelation function side-lobes.

# Appendix A

# Chaos-Based Waveforms in Practice

The preceding chapters describe the utilization of chaotic systems to generate sets of quasi-orthogonal radar waveforms. This appendix evaluates the performance of the designed waveforms in an operational radar system. Before evaluating the waveforms in practice, the complex base-band waveforms in Chapter 5 need to be converted into real signals capable of being transmitted, which is explained next.

## A.1 Synthesizing a Transmit Radar Waveform

Transmitting a radar waveform requires the conversion of a base-band waveform to a real signal via Eq. 3.7. Consequently, the procedure for generating Lorenz-based waveforms (as given in Fig. 5-15) is modified to account for the construction of this real radar signal. The new generating procedure for the synthesized radar signal is given in Fig. A-2. As can be seen from the figure, the amplitude clipping function in Eq. 5.27 has been placed after the construction of the real signal, since this location more effectively reduces the peak-to-RMS ratio. A summary of the changes made to the original procedure can be found in Fig. A-1 where $\omega_c = 2\pi 800$ rad/s and $x_6(t)$ is as defined in Section 5.2. The synthesized radar waveforms will still be referred to as Lorenz-based waveforms.

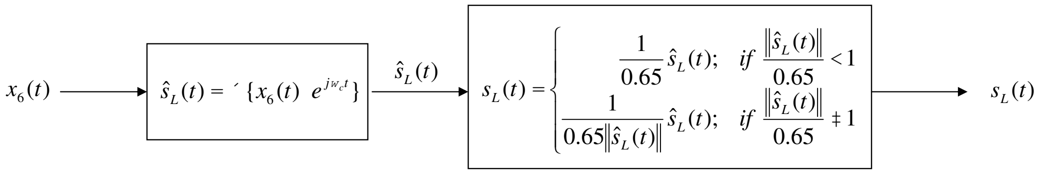

Figure A-1: Summary of Changes made to Waveform Generation Procedure.

To generate one particular Lorenz-based waveform, a Lorenz waveform, $x_L(t)$, is generated as described in Section 5.1 with one exception. The bandwidth for the waveforms generated in this appendix is specified to be 440 MHz (as opposed to 500 MHz) in order to minimize the effect of the hardware filters on the transmitted waveform[1]. This Lorenz waveform is then passed through the improvement procedure given in Fig. A-2, which results in the generation of a Lorenz-based waveform. Although practically infinite numbers of these waveforms are realizable, the results of just one waveform are shown to illustrate the typical results. This waveform will be referred to as $s_L(t)$. Since the systematic generating procedure has been modified and for reference, $s_L(t)$ is compared with $\mu_L(t)$ and $w(t)$, which were introduced and evaluated in Chapter 5.

When comparing the PRMS, it is important to clarify that the PRMS of a transmitted waveform is different from the PRMS of a base-band waveform. The PRMS of a transmit signal should be close to 1.414; whereas, the PRMS of a base-band signal should be close to unity as explained in Section 3.1. To compare the PRMS of $s_L(t)$ and $w(t)$, the transmit signal, $s_w(t)$, corresponding to $w(t)$ is calculated from Eq. 3.7. The PRMS of $s_L(t)$ and $s_w(t)$ is 1.51 and 1.72, respectively. A value of 1.51 for $s_L(t)$ is significantly less than the value 1.72 for $s_w(t)$. Moreover, 1.51 is close the the desired value of 1.414. A 2 $\mu s$ time segment of $s_L(t)$ is included in Fig. A-3 to illustrate this low PRMS.

The PRMS of $s_L(t)$ compares more favorably against the PRMS of $s_w(t)$ than did the PRMS of $\mu_L(t)$. Specifically, if the transmit signal corresponding to $\mu_L(t)$ is calculated from Eq. 3.7, the PRMS is 1.73, which is about the same as the PRMS of

---

[1] Consequently, the main-lobe increased by a factor of 1.15.

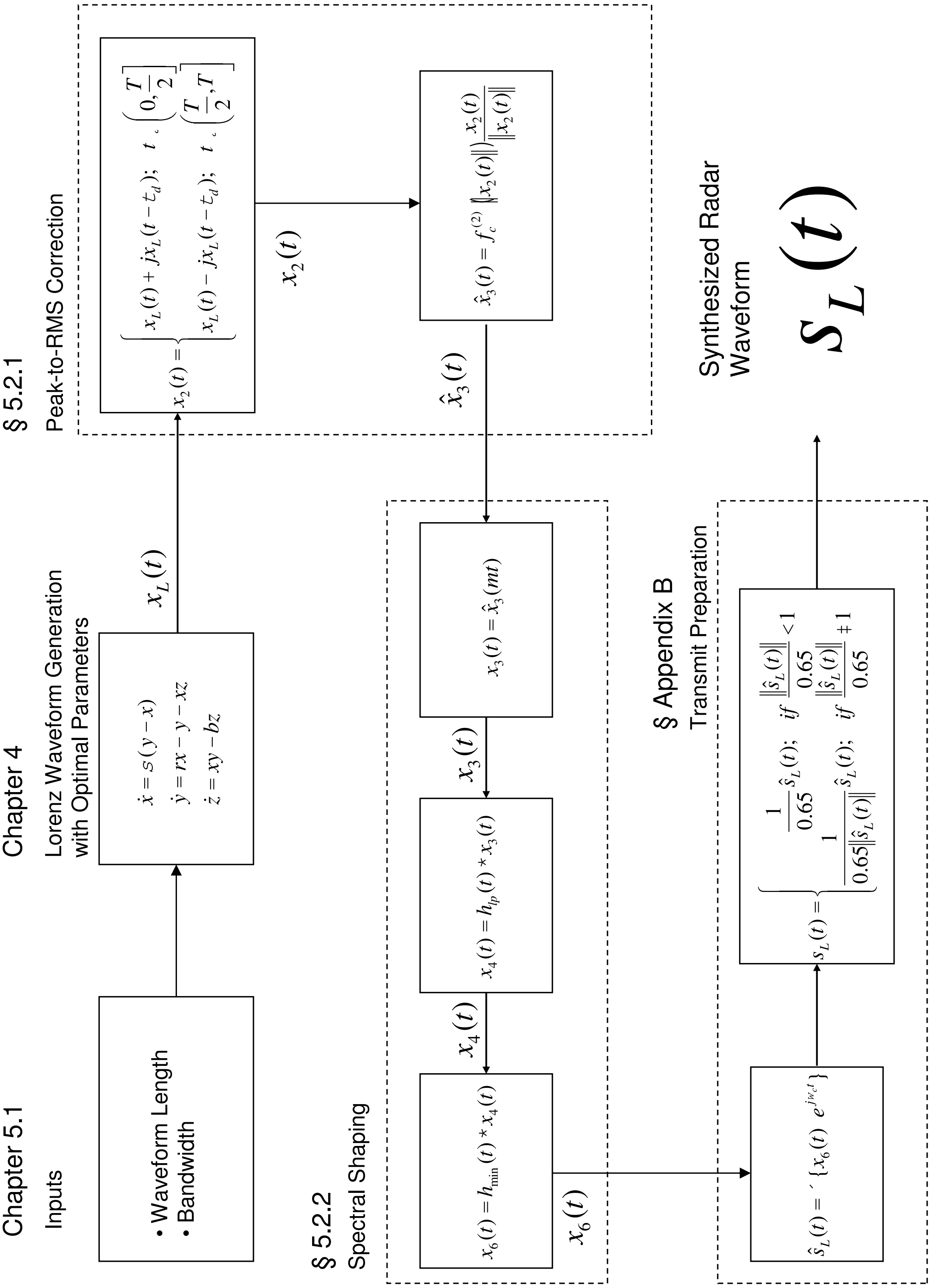

Figure A-2: Systematic Procedure for Generating Lorenz-Based Waveforms.

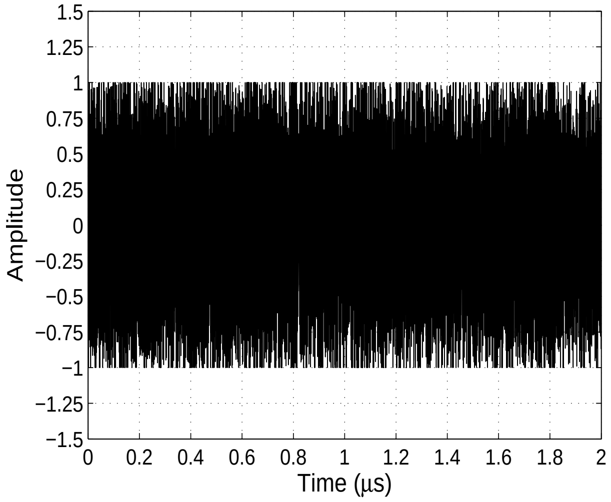

Figure A-3: A 2 $\mu s$ Time Segment of $s_L(t)$.

$w(t)$. As claimed earlier, the amplitude clipping function (which lowers the PRMS) described in Eq. 5.27 is justified in being implemented on the real signal as opposed to the base-band signal, and the low PRMS is now another advantage of the Lorenz-based waveform over $w(t)$.

The base-band signal, $\tilde{\mu}_L(t)$ (not to be confused with $\mu_L(t)$ as defined in Chapter 5), corresponding to $s_L(t)$ can be recovered with Eqs. 3.3 and 3.6. The autocorrelation of $\tilde{\mu}_L(t)$ is given Fig. A-4 and demonstrates a narrow main-lobe and low side-lobes. Specifically, the side-lobes centered around the main-lobe are especially low as a result of the application of the filter described in Eq. 5.26. The side-lobes far away from the main-lobe are at the same level as $w(t)$, as discussed in Section 5.3.1. The autocorrelation function for $\tilde{\mu}_L(t)$ is qualitatively equivalent to the autocorrelation function of $\mu_L(t)$ (given in Fig. 5-16), and both functions outperform the autocorrelation function of $w(t)$ (given in Fig. 5-2). Also for completeness, the ambiguity function of $s_L(t)$ is included. Details on the ambiguity function are given in [14] and not explained herein.

The energy spectrum for $s_L(t)$ is given in Fig. A-6, which was computed via Eq. 3.22. As explained in Chapter 3, the energy of the transmit signal is concentrated around the carrier frequency of 800 MHz. Only the positive frequencies are given in this figure; however, the energy spectrum is symmetric, since $s_L(t)$ is real. The spectrum of $s_L(t)$ is appropriately compact when compared energy spectra of both $w(t)$ and $\mu(t)$, which are given in Section 5.3.3. Although the spectra in Section 5.3.3 are centered around base-band, computing the real signals of these two base-band functions via Eq. 3.7 would center the spectra around 800 MHz, and all these real signals would be qualitatively equivalent.

As discussed in Section 5.3.4, the cross-correlation level of $\mu_L(t)$ is unaffected by the operations that modify $x_L(t)$. The same results hold true in this section although the plots and discussion are omitted to avoid repetitiveness

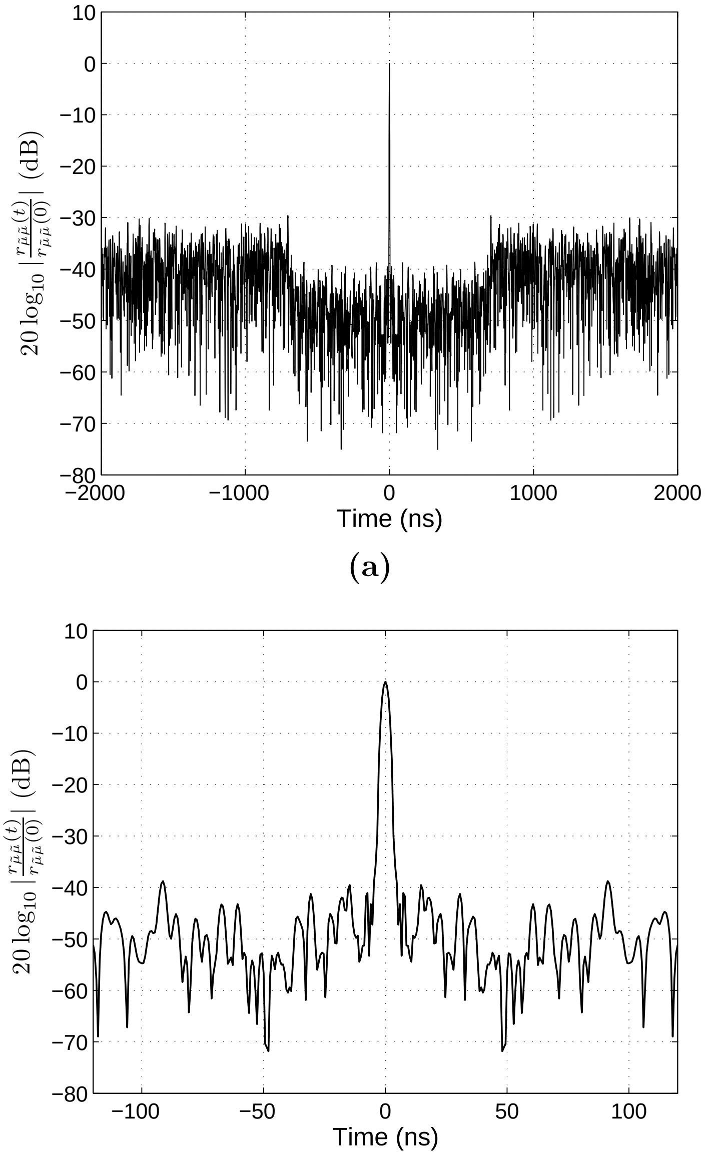

**(a)**

**(b)**

Figure A-4: The Autocorrelation Function of the Lorenz-based Waveform. The second plot is an enlarged view of the first plot.

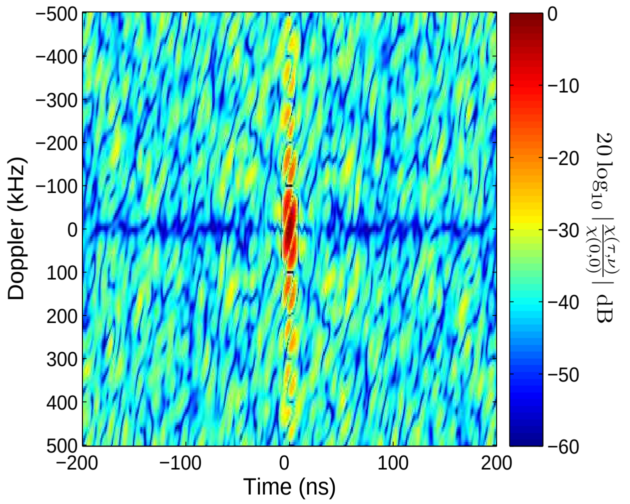

Figure A-5: Ambiguity Function for $s_L(t)$. The ambiguity function, $\chi(\tau, \nu)$, was calculated from Eq. 5.1 in [14] where $\tau$ is corresponds to the time delay and $\nu$ corresponds to the doppler effect.

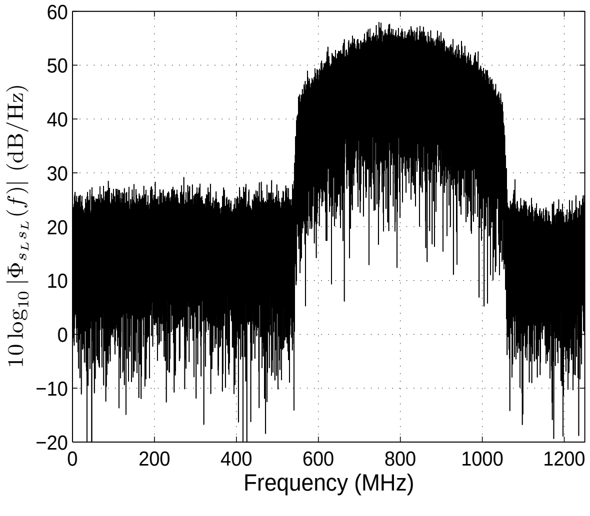

Figure A-6: Energy Spectrum of $s_L(t)$.

## A.2 Experimental Setup and Results

The synthesized radar waveform $s_L(t)$ was placed in an operational radar at M.I.T. Lincoln Laboratory. Figure A-7 shows this radar operating with a Lorenz-based waveform. The antennas transmitting the waveforms are seen in the background of the picture, and three instruments taking measurements of the Lorenz-based waveform can be seen in the foreground. The radar waveform $s_L(t)$ was radiated from the antennas at a moving target simulator (not seen in the photo) about ten feet from the antennas. The scattering response from the target simulator was then received by the same antennas from which the waveform was transmitted. The received waveform will be referred to as $s_r(t)$. Via Eqs. 3.3 and 3.6, the base-band signal, $\mu_r(t)$, can be recovered from $s_r(t)$.

As the case in many radar systems, the target response is determined by converting the returned signal to a base-band signal and cross-correlating it with a time-reversed, base-band replica of the transmitted waveform[2], $\tilde{\mu}_L(t)$. This operation can be expressed as shown in Eq. A.1.

$$r_{\mu_r \tilde{\mu}_L}(t) = \int_{-\infty}^{\infty} \mu_r(\tau)\tilde{\mu}_L^*(\tau - t)d\tau \tag{A.1}$$

If a target is approximated by a group of point scatterers in a zero-noise environment, $r_{\mu_r \tilde{\mu}_L}(t)$ would be a linear superposition of the function $r_{\tilde{\mu}_L \tilde{\mu}_L}(t)$ as long as $s_L(t)$ is not significantly distorted by the transmit or receive process. The time, $t$, of $r_{\mu_r \tilde{\mu}_L}(t)$ is proportional to the distance, in range, between the target and the radar. The amplitude of $r_{\mu_r \tilde{\mu}_L}(t)$ is related to the size of the target (among other factors)[3]. Thus, for illustration purposes, the signal-to-noise ratio for this experiment was set to be sufficiently high to test if $s_L(t)$ is significantly distorted.

After receiving $s_r(t)$, $r_{\mu_r \tilde{\mu}_L}(t)$ is calculated and plotted in Fig. A-8. In the figure, the function has been normalized, and the time axis has been shifted so that the

---

[2] More information on radar processing and radar systems can be found in [14] and [17].

[3] In general, the doppler effect on the waveform due to the motion of the target must be properly removed. For simplicity, the doppler effect is made negligible in this experiment, although in practice, compensation for doppler needs included in target detection.

Figure A-7: Operational Radar Utilizing Lorenz-based Waveforms. The first instrument on the left is an oscilloscope, which measures the amplitude of the transmitted waveform in time. Moving to the right, the next instrument is spectrum analyzer, which displays the frequency content of the transmitted waveform. Finally to the right of the spectrum analyzer is a computer monitor, which displays the cross-correlation function (compressed pulse) of the received waveform with the time-reversed replica of the transmitted waveform.

peak value of 0 dB occurs at $t = 0$. The function $r_{\mu_r \tilde{\mu}_L}(t)$ is then compared with the function $r_{\tilde{\mu}_L \tilde{\mu}_L}(t)$ by plotting $r_{\tilde{\mu}_L \tilde{\mu}_L}(t)$ behind the plot of $r_{\mu_r \tilde{\mu}_L}(t)$. Figure A-8 demonstrates that the target response is more complicated than the response of a single point scatterer[4]. However, since the magnitude of the leading scatterer at $t = 0$ is significantly greater than the magnitude of the other scatterers, the leading scatterer dominates $r_{\mu_r \tilde{\mu}_L}(t)$ outside the range of times corresponding to the response of the target, i.e. outside $t \in [0, 200]$. Outside this region, $r_{\mu_r \tilde{\mu}_L}(t)$ closely approximates $r_{\tilde{\mu}_L \tilde{\mu}_L}(t)$ as can be verified by the figure. Specifically, the low side-lobe basin centered about the main-lobe is not degraded by the transmit or receive process. In fact, the visibility of the target response is the result of especially low side-lobes centered about the main-lobe. Additionally, the main-lobe of the autocorrelation function is not significantly widened. Consequently, comparing $r_{\mu_r \tilde{\mu}_L}(t)$ and $r_{\tilde{\mu}_L \tilde{\mu}_L}(t)$ verifies that $s_L(t)$ is not significantly distorted by the transmit and receive process.

---

[4] This target response is also verfied using other waveforms independent of chaotic systems.

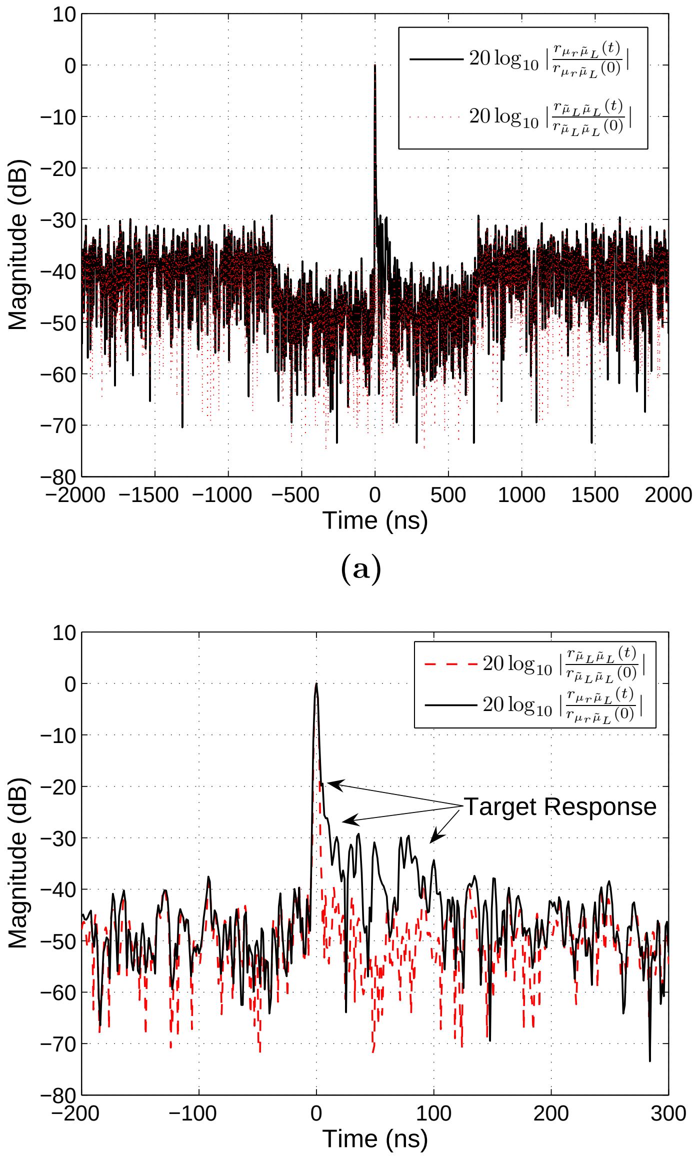

**(a)**

**(b)**

Figure A-8: The Function $r_{\mu_r\tilde{\mu}_L}(t)$. This figure demonstrates that several properties of the waveforms designed in Chapter 5 are realizable in practice by comparing the expected results with the realized results. The second plot is an enlarged view of the first plot and illustrates the detailed response of the target.

## A.3 Chaotic Synchronization through Free Space Transmission

Chapter 6 suggests studying the exploitation of chaotic synchronization. The purpose of this section is to demonstrate preliminary results of what appears to be the approximate self-synchronization of a received radar waveform through free-space transmission. As explained in [4], the Lorenz system is a self-synchronizing chaotic system that satisfies Eqs. A.2 - A.5.

$$\begin{pmatrix} \dot{x}_d \\ \dot{y}_d \\ \dot{z}_d \end{pmatrix} = \begin{pmatrix} \sigma(y_d - x_d) \\ rx_d - \sigma y_d - x_d z_d \\ x_d y_d - b z_d \end{pmatrix} \tag{A.2}$$

$$\begin{pmatrix} \dot{y}_r \\ \dot{z}_r \end{pmatrix} = \begin{pmatrix} rx_d - y_r - x_d z_r \\ x_d y_r - b z_r \end{pmatrix} \tag{A.3}$$

$$\dot{x}_r = \sigma(y_r - x_r) \tag{A.4}$$

$$\begin{pmatrix} x_d(t) - x_r(t) \\ y_d(t) - y_r(t) \\ z_d(t) - z_r(t) \end{pmatrix} \approx \begin{pmatrix} 0 \\ 0 \\ 0 \end{pmatrix} \tag{A.5}$$

The system given in Eq. A.2 is considered the drive system that outputs a drive waveform, $x_d(t)$. The system in Eqs. A.3 and A.4 is considered the receiver, which receives $x_d(t)$ and generates three receive state variables: $x_r(t)$, $y_r(t)$, and $z_r(t)$. In a zero-noise environment, the state variables of the receiver equations will exponentially approach the state variables of the drive system. Thus, assuming a sufficient amount of time has passed, the receive state variables approximately equal the drive state variables as expressed in Eq. A.5.

To demonstrate approximate self-synchronization, a radar waveform is generated as shown Fig. 5-15. However, instead of using $\mu_L(t)$ as the base-band radar waveform, $x_4(t)$ is used as the radar waveform to avoid too severely modifying the original Lorenz waveform[5]. The real component of $x_4(t)$ approximates a time segment of the $x$ state variable of the Lorenz system as illustrated in Fig. A-9. The waveform $x_4(t)$ is then related to a transmit signal, transmitted through free-space, received, and converted again to a base-band waveform, $\hat{x}_4(t)$. A plot of the matched filter response of $\hat{x}_4(t)$ is provided in Fig. A-10 for reference. Using the real component of $\hat{x}_4(t)$ as the drive waveform $x_d(t)$, $x_r(t)$ is computed from Eqs. A.3 and A.4. The close correspondence between $\hat{x}_4(t)$ and $x_r(t)$, in Fig. A-11, demonstrates the preliminary results of what appears to be approximate self-synchronization of chaotic systems via free-space transmission.

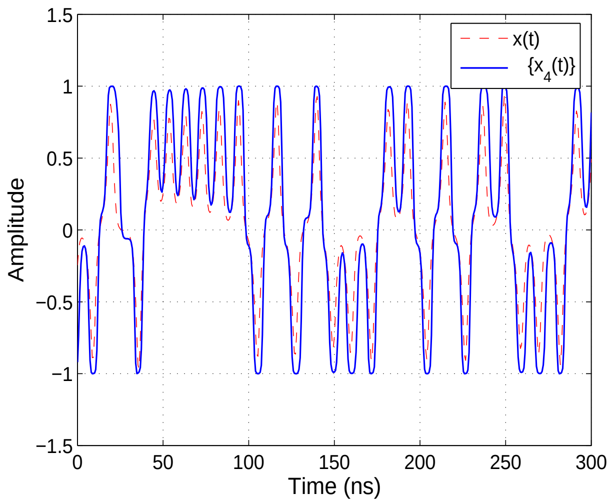

Figure A-9: Comparison of the Real Component of $x_4(t)$ with the $x$ State Variable.

---

[5] Although an evaluation on the design considerations of Chapter 3 is not shown, $x_4(t)$ is comparable to the practical waveform $w(t)$ introduced in Chapter 5.

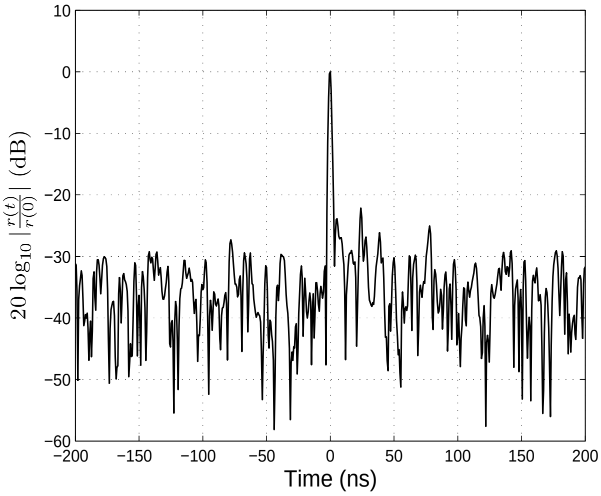

Figure A-10: Matched-Filtered Response for $\hat{x}_4(t)$. The function $r(t)$ denotes this response.

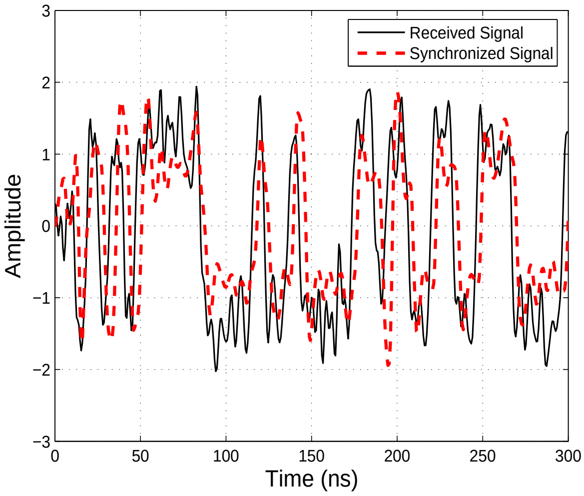

Figure A-11: Chaotic Synchronization through Free Space Transmission. The real part of $\hat{x}_4(t)$ is considered the received waveform, and $x_r(t)$ is considered the synchronized waveform.

# Bibliography

[1] John Paul Braud. Private Communication.

[2] Kevin M. Cuomo. Private Communication.

[3] Apostolos Argyris, Dimitris Syvridis, Laurent Larger, Valerio Annovazzi-Lodi, Pere Colet, Ingo Fischer, Jordi Garcia-Ojalvo, Claudio R. Mirasso, Luis Pesquera, and K. Alan Shore. Chaos-based communications at high bit rates using commercial fibre-optic links. *Nature*, 437:343–346, November 2005.

[4] Kevin M. Cuomo. Analysis and synthesis of self-synchronizing chaotic systems. Doctoral thesis, Massachusetts Institute of Technology, 77 Massachusetts Avenue Cambridge, MA 02139, February 1994.

[5] Kevin M. Cuomo, Alan V. Oppenheim, and Richard J. Barron. Channel equalization for self-synchronizing chaotic systems. In Proceedings of the IEEE ICASSP, (Atlanta, Georgia), 1996.

[6] John Guckenheimer. A strange, strange attractor. *The Hopf Bifurcation and Its Applications*. Marsden and McCracken, eds., Applied Mathematical Sciences, Springer-Verlag, 1976.

[7] John Guckenheimer. On the bifurcation of maps of the interval. *Inventiones Mathematicae*, 39(2):165–178, June 1977.

[8] John Guckenheimer and Philip Holmes. *Nonlinear Oscillations, Dynamical Systems, and Bifurcations of Vector Fields*, volume 42 of *Applied Mathematical Sciences*. Springer-Verlag, New York, New York, 1983.

[9] John Guckenheimer and Robert F. Williams. Structural stability of Lorenz attractors. *Publications Mathématiques de L'I.H.É.S.*, 50:59–72, 1979.

[10] Edward N. Lorenz. Deterministic nonperiodic flow. *Journal of the Atmospheric Sciences*, 20:130–141, March 1963.

[11] Alan V. Oppenheim and Ronald W. Schafer. *Discrete-Time Signal Processing.* Signal Processing Series. Prentice Hall, Upper Saddle River, New Jersey, 1999.

[12] Alan V. Oppenheim, Ronald W. Schafer, and John R. Buck. Parametric signal modeling for discrete-time signal processing, third edition. 2004.

[13] L. M. Pecora and T. L. Carroll. Synchronization in chaotic systems. *Physical Review Letters*, 64(8):821–824, April 1991.

[14] August W. Rihaczek. *Principles of High-Resolution Radar*, volume 42 of *Applied Mathematical Sciences.* Artech House, Norwood, Massachusetts, 1996.

[15] Frank C. Robey, Scott Coutts, Dennis Weikle, Jeffrey C. McHarg, and Kevin Cuomo. MIMO radar theory and experimental results. in Signals, Systems and Computers, 2004. Conference Record of the Thirty-Eighth Asilomar Conference, (Pacific Grove, CA), 2004.

[16] William McC. Siebert. *Circuits, Signals, and Systems.* The MIT Electrical Engineering and Computer Science Series. The MIT Press, 1986.

[17] M. I. Skolnik. *Radar Handbook.* McGraw-Hill, second edition, January 1990.

[18] S. H. Strogatz. *Nonlinear Dynamics and Chaos.* Addison-Wesley, 1994.

[19] R.F. Williams. The structure of Lorenz attractors. *Publications Mathématiques de L'I.H.É.S.*, 50:73–99, 1979.